INFORMATION TO USERS

This manuscript has been reproduced from the microfilm master. UMI films the text directly from the original or copy submitted. Thus, some thesis and dissertation copies are in typewriter face, while others may be from any type of computer printer.

The quality of this reproduction is dependent upon the quality of the copy submitted. Broken or indistinct print, colored or poor quality illustrations and photographs, print bleedthrough, substandard margins, and improper alignment can adversely affect reproduction.

In the unlikely event that the author did not send UMI a complete manuscript and there are missing pages, these will be noted. Also, if unauthorized copyright material had to be removed, a note will indicate the deletion.

Oversize materials (e.g., maps, drawings, charts) are reproduced by sectioning the original, beginning at the upper left-hand corner and continuing from left to right in equal sections with small overlaps.

Photographs included in the original manuscript have been reproduced xerographically in this copy. Higher quality 6" x 9" black and white photographic prints are available for any photographs or illustrations appearing in this copy for an additional charge. Contact UMI directly to order.

ProQuest Information and Learning
300 North Zeeb Road, Ann Arbor, MI 48106-1346 USA
800-521-0600

Investigation of Auroral Hiss Observations on the Ground: Application to Remote Sensing of Auroral Magnetosphere

A

THESIS

Presented to the Faculty

of the University of Alaska Fairbanks

in Partial Fulfillment of the Requirements

for the Degree of

DOCTOR OF PHILOSOPHY

By

Jayashree Harikumar, M.S.(EE).. M.S.C.S.

Fairbanks, Alaska

December 2001

UMI Number: 3029823

Bell & Howell Information and Learning Company
300 North Zeeb Road
P.O. Box 1346
Ann Arbor, MI 48106-1346

Investigation of Auroral Hiss Observations on the Ground: Application to Remote Sensing of Auroral Magnetosphere

By

Jayashree Harikumar

RECOMMENDED:

Dr. Vikas Sonwalkar (Chair)

Dr. Charles Mayer (Department Chair)

Dr. Joseph Hawkins

Dr. Davis Sentman

Dr. John Olson

APPROVED:

Dean, College of Science, Engineering and Mathematics

Dean of the Graduate School

11-4-01

Date

Abstract

Observed both on the ground at high latitudes and on spacecraft in the auroral zone, auroral hiss (AH) emissions ($\sim$ 1 kHz to $\sim$ 1 MHz) are intense electromagnetic emissions emitted from the auroral region. Standard whistler mode propagation theory in a smooth magnetosphere predicts that AH generated at large wave-normal angles along the auroral field lines by Cerenkov resonance cannot penetrate to the ground. This thesis presents a new mechanism of AH propagation to the ground in which presence of density depletions along the field lines in the auroral zone and meter-scale density irregularities at altitudes <5000 km at high latitude permits the AH propagation to the ground. In the proposed mechanism AH generated at high altitudes ($> 5000 - 20,000$ km) propagates to lower altitudes ($< 3000 - 5000$ km) in two modes, the ducted mode and the non-ducted mode, with large wave-normal angles. At altitudes <5000 km meter-scale irregularities scatter the hiss into electrostatic waves with large wave-normal angles that are reflected into the magnetosphere and electromagnetic waves with small wave-normal angles that can penetrate to the ground. The AH propagation model proposed in this thesis also explains the spectral characteristics of AH including the upper and lower frequency cutoffs, the dispersion of AH, the location of ionospheric exit points of AH with respect to visible aurora, and the 2-5 orders of magnitude difference in the power spectral density ratio measured on satellites versus ground. The new understanding of AH permits the determination of AH source region, energetic electron parallel resonance energy, and cold plasma electron concentrations along field lines. Analysis of AH spectra, recorded at South Pole (July 09, 1996 0005 UT), using the model developed in this thesis shows that: (a) AH source region altitude for frequencies 7-9 kHz should be $>$ 16,000 km while for frequencies 12-20 kHz it should be $<$ 8000 km. (b) parallel resonance energy of the energetic electrons generating the frequencies should be $<$ 1 keV, and (c) cold plasma electron concentration along the field line $\Lambda = 79°$ should be $\sim$ 100 el cm^{-3} at 12,740 km altitude.

Table of Contents

LIST OF FIGURES

LIST OF TABLES

Acknowledgements

My advisor, Dr. Vikas Sonwalkar has been pivotal to my understanding of the field. He has taught me how to view problems in simple geometric terms. His style of breaking complex problems into several simple ones helped me to keep the results tractable. There are other professors on my thesis committee who inspired me during my doctoral studies. Dr. Hawkins's and Dr. Mayer's enthusiasm when teaching space related engineering topics helped me develop the right attitude to face the challenges during my thesis work. Dr. Olson's discipline in pursuing a problem helped me develop complete dedication and tenacity towards my quest in this thesis. Dr. Sentman with his seemingly boundless energy showed me how to evaluate all possible solutions to a problem.

I would like to thank Mr. Earl Tech, Mr. Steve Blair, Mr. Robert Dingler and Mr. John Sutton for having given me the opportunity to work for Los Alamos National Laboratory as a student assistant in Fairbanks. This uninterrupted assistantship helped me concentrate on my doctoral studies during the final three years. My gratitude to Ms. Barbara Adams, my good friend, for all her help and for the timely help she and Mr. Lai rendered just prior to my thesis defense.

During the final stages of my thesis, I was blessed with a handsome son, Sanjiv. My parents, husband, parents-in-law, and sister-in-law stepped up to the plate and made it possible for me to devote time towards my thesis. I am eternally grateful for their words of encouragement and advise as they stood by me during the trying times in my research. I have been truly fortunate to have their support and their willingness to give me the space to develop and finish this thesis. They have shown me that being anchored in life as a human and learning to sacrifice for one another is as important as being a scientist. Learning is fun. My 18 month son taught me patience and showed me how to look at problems as fun games to be solved. I thank God for having blessed me with wonderful professors, a loving family and friends.

This research was sponsored by the Los Alamos National Laboratory under contract 389AZ0017-97 to the University of Alaska Fairbanks.

1. Introduction

The scientific objective of this thesis is to help understand the generation and propagation mechanism of auroral hiss observed at high latitudes. These electromagnetic whistler mode waves propagate through the Earth's magnetosphere and ionosphere. In sections 1.1 and 1.2 of this chapter a brief description of the Earth's magnetosphere and whistler mode waves in the magnetosphere are provided. Section 1.3 is an introduction to the work done in this thesis. The organization of this thesis report is detailed in section 1.4. Section 1.5 lists the specific contributions made by the present work.

1.1 The Earth's Magnetosphere

The air near the ground is unionized and its electrical conductivity is very small. This region of the Earth's atmosphere is $\sim 50 - 80$ km thick. This region is controlled by the Earth's gravitational field and so it is a horizontally stratified system. The next layer between 80 and 1000 km is the *ionosphere*. There are several different ionospheric layers. The main ones are the E-layer at $\sim$ 100 km and the F-layer at $\sim$ 300 km with an ion and electron concentration of about 10^{-11} and 10^{-5} of the neutral particles, respectively. Above 1000 km is the Earth's *magnetosphere* (Figure 1.1.1) which is a fully ionized ion plasma and the dynamics of the charged particles in this region are controlled by the geomagnetic field. The magnetosphere extends to about 14 R_E on the sunlit side of the Earth. R_E is one Earth radius (6370 km) usually measured from the center of the Earth. The magnetosphere is like a conducting fluid surrounding Earth and its shape is greatly influenced by the solar wind, which is a fully ionized plasma flowing outwards from the sun. The solar wind is a good conductor and the Earth's magnetic field cannot quickly penetrate into it. As a result, a sharp boundary is formed when the solar wind encounters the Earth's magnetic field which forms

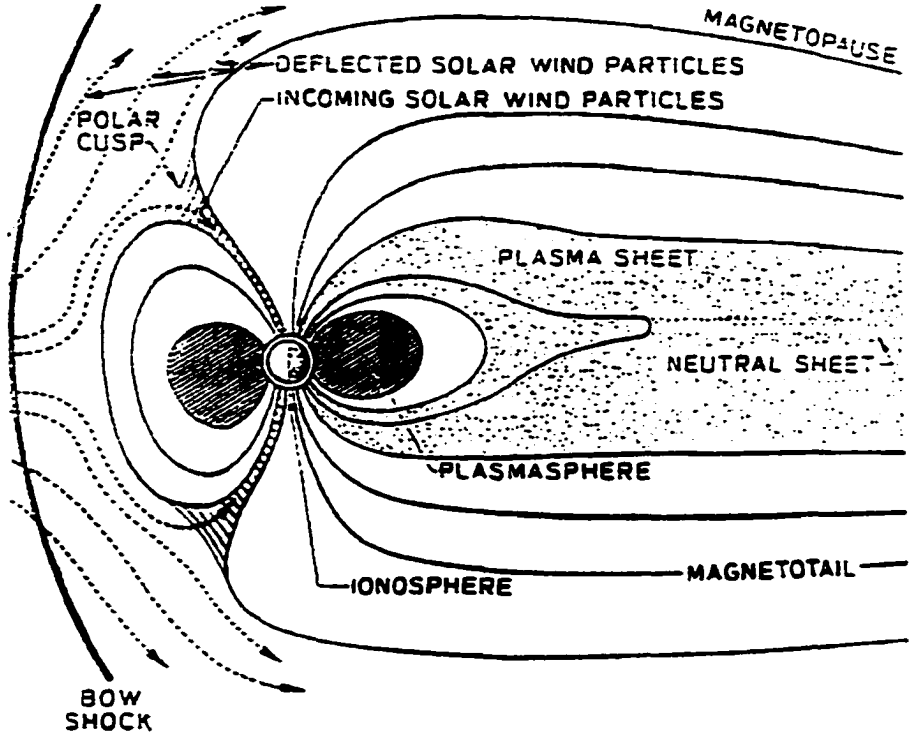

Figure 1.1.1. Schematic of the Earth's Magnetosphere.

forms an outer region where the solar wind distorts the magnetosphere and draws it out onto a long tail. the *magnetotail* on the remote side of the sun. and an inner region that contains the compressed geomagnetic field. and from which the wind is excluded. The magnetotail extends to distances beyond the radius of the moon's orbit and consists of roughly oppositely directed field lines separated by a neutral sheet of ~ 0 magnetic field. The inner region is called the magnetosphere. and the boundary is called *magnetopause*. At the magnetopause which is located ~ 10 Earth radii towards the sun. the pressure of the geomagnetic field is balanced by the kinetic pressure of the solar wind particles. The impact of the solar wind on the magnetospheric boundary results in a standoff shock wave near which the flow lines change their direction abruptly. This region of plasma turbulence beyond the magnetopause is called the *magnetosheath* and it is about $2\ R_E$ along the Earth-Sun axis. The day side of the shock front is called the bow shock.

The geomagnetic field up to about $6\ R_E$ in the magnetic equatorial plane and between $\pm 66^o$ geomagnetic latitudes of the earth. can be approximated by a magnetic dipole at the center of the Earth. At greater distances the solar wind distorts the dipole symmetry and each field line is now compressed and defined by a parameter L. where $L = R/(R_E cos^2 \lambda)$ [*McIlwain.* 1961]. R is the geocentric distance and λ is the magnetic latitude.

Ionization by solar ultra violet ray radiation in the daytime F region of the ionosphere is believed to generate thermal or cold plasma. which then flows along field lines to fill an inner region of the magnetosphere called the *plasmasphere*. The plasmasphere consists of thermal electrons. protons and some He^+ and O^+ ions in the ≤ 1 eV range. The electrons and ions in the plasmasphere are in diffusive equilibrium and approximately corotate with the Earth. The region beyond the plasmasphere has charged particles of higher energy. $10^2 - 10^4$ eV. but of smaller concentrations typically in the order of 1 el cm^{-3} and is called the *plasmatrough*. The boundary between the plasmasphere and the plasmatrough is called the *plasmapause*. The cold plasma density measured at the geomagnetic

equator gradually decreases with increasing distance from the earth up to the plasmapause, at which point the electron concentration drops by two orders of magnitude over a distance of < 1000 km. The plasmapause is typically near $L \approx 4 - 5$ for quiet geomagnetic conditions.

The magnetosphere in general is a dynamic system and the location of the plasmasphere depends on the global geomagnetic activity. The plasmasphere also contains protons and electrons with energies extending from approximately 100 eV up to hundreds of MeV. These energetic particles form the earth's radiation belts and those that are magnetically trapped in the geomagnetic field execute three distinct motions: a helical gyration around the field lines, a bounce motion along the field lines between the two mirror points in the conjugate hemispheres, and a slow drift in longitude across the field lines. Longitudinal drift is negligible at altitudes less than a few hundred kilometers because of atmospheric losses. Also, at altitudes greater than 10 R_E, magnetic field distortions make longitudinal drift impossible.

The ionosphere has traditionally been treated as horizontally stratified because the Earth's gravity is a controlling factor at these altitudes. However, there are horizontal gradients of enhanced and/or depressed ionization present throughout the ionosphere at all times. The majority of these density gradients or irregularities are aligned along the Earth's magnetic field lines so that the gradient of density is perpendicular to the field line. Radar and in-situ measurements place the spatial scale of these irregularities from 10 centimeters to hundreds of kilometers and the density changes from a few percent to 500 percent [*Fejer and Kelley*, 1980].

There is no sharp physical boundary between the ionosphere and the magnetosphere. *Storey* [1953] used electromagnetic waves called *whistlers* to show that the Earth's plasma extended far beyond the F-layer. Prior to his work, ground-based measurements were used to infer the Earth's atmosphere above 200-300 km. Extrapolation from these measurements led to the belief that the atmosphere becomes less dense with increasing altitude and eventually merges

into empty space, or rather into interplanetary space with an electron density of $\sim$ 1 el cm^{-3} at about 1000 km above the ground. It is for this historical reason that the boundary between the ionosphere and the magnetosphere is often set between 500 and 1000 km.

1.2 Whistler Waves in the Magnetosphere

The Earth's magnetic field along with the electrons and ions of finite temperatures in the Earth's magnetosphere makes the magnetospheric plasma anisotropic, which supports a number of wave modes. Electromagnetic, electrostatic, and magnetosonic waves exist in the magnetosphere. In this thesis, a cold plasma model and whistler mode wave propagation is assumed. Whistlers are very-low-frequency (VLF) electromagnetic waves produced by lightning discharges. A lightening discharge radiates electromagnetic energy over a wide range of frequencies and the source of whistlers is radiation from the 300 Hz to 30 kHz range. Whistlers are produced when different frequency components of the impulsive lightening pulse travel through the Earth's ionosphere and magnetosphere at different speeds. These radio waves are so named because in the audio-frequency range the high frequency components are heard before the low frequency components and the drop in frequency is $\sim$ 1000 Hz in one second and thus the wave sounds like a "whistle" [*Helliwell*, 1965]. Since whistlers exist in the audio-frequency range, they can be heard with an earphone. The whistler mode exists at frequencies below both the local plasma frequency f_{pe} and local electron gyrofrequency f_H. The wave-normal vectors for whistlers are confined within the resonance cone centered about the geomagnetic field line. A whistler wave undergoes reflection when its wave frequency is equal to the local lower hybrid frequency f_{LHR} and propagation is perpendicular to the ambient magnetic field. Thus the local f_{LHR} provides the lower cutoff frequency for whistler waves. The whistler mode wave polarization is generally right-hand elliptic and it has a right-hand circular polarization when propagating parallel to the mag-

netic field line with its wave vectors rotating in the same sense as an electron gyrating about the field line. Whistler mode waves propagate at velocities well below the wave velocity in vacuum and the slow phase velocities allow the waves to interact strongly with energetic electrons.

Wave propagation in a magnetoplasma is both anisotropic (refractive index μ depends on the wave-normal angle θ) and dispersive (μ depends on frequency f) and the direction of propagation or ray direction of a wavepacket of finite temporal duration and spatial extent is different from the wave-normal direction. For whistler mode signals the ray direction is normal to the refractive index surface and the ray angle α between the ray direction and the wave-normal direction is given by

$$\tan\alpha = \frac{-1}{\mu}\frac{\delta\mu}{\delta\theta}$$

At low frequencies the ray direction is close to the static magnetic field and in the zero frequency limit the maximum possible angle is $\sim 19.3°$. The geomagnetic field thus affects the wave-normal direction and ray path and tries to guide rays along the field lines. Additionally, the magnetosphere is inhomogeneous and the field-aligned enhancements of ionization act as a waveguide to trap the wave energy. However, the medium properties change slowly over many wavelengths of a plasma wave mode, and one can still consider propagation of plasma waves in terms of an infinite homogeneous plasma. This approximation is called the ray approximation.

Most of the waves in the magnetosphere cannot reach a ground receiver because they are either totally internally reflected at the Earth-ionospheric boundary, where the refractive index changes from a large value ($\sim 10 - 100$) in the ionosphere to one on Earth, or the waves undergo LHR (local hybrid resonance) reflections in the magnetosphere. However, field-aligned columns of enhanced or depressed ionization called *ducts* can guide the waves to the low altitude ionosphere. The *wave – normal* angle (angle between the wave normal and the

ambient magnetic field) is small for ducted waves and large for nonducted waves. Typical free-space wavelengths for 1-30 kHz whistlers range from 300 to 10 km. These wavelengths are greater than the $\sim 60 - 300$ km altitude low ionosphere. As a result the refractive index changes rapidly in the lower ionosphere and the ray approximation cannot be applied in this region. Additionally, by Snell's law if waves are generated at all angles at low altitudes, those waves with sufficiently small angles with respect to vertical can reach the ground. Nonducted waves can also be guided along the plasmapause to the ground [*Inan and Bell*, 1977] or along ionospheric irregularities [Kelly, 1980]. In general a signal observed at the ground is a sum of the signals that have exited from various ducts located at different altitudes, latitudes and longitudes. A detailed study of whistlers can be found in a monograph by *Helliwell* [1965].

1.3 Auroral Hiss

Energetic electrons in the magnetosphere give rise to a variety of VLF emissions. Depending on their characteristic features or spectral forms these emissions are classified as "hiss", "discrete emissions", "periodic emissions", "chorus", "quasi-periodic emissions", and "triggered emissions". *Helliwell* [1965] has given us an excellent collection of spectrograms to classify these emissions. VLF emissions are localized geographically and most commonly observed at middle and high latitudes. At geomagnetically conjugate locations emissions are often related in time of occurrence and form.

Auroral Hiss (AH) is a broadband, whistler mode plasma wave emission. It is emitted from the auroral region and is identified aurally by a hissing sound. It has a wide frequency range from a few hundred Hertz to several hundred kiloHertz. The spectrum for hiss resembles that of a band-limited noise. AH frequency is always below the local electron gyrofrequency and plasma frequency. Examples of AH spectra are as shown in Figure 1.3.1. AH is observed both on the ground

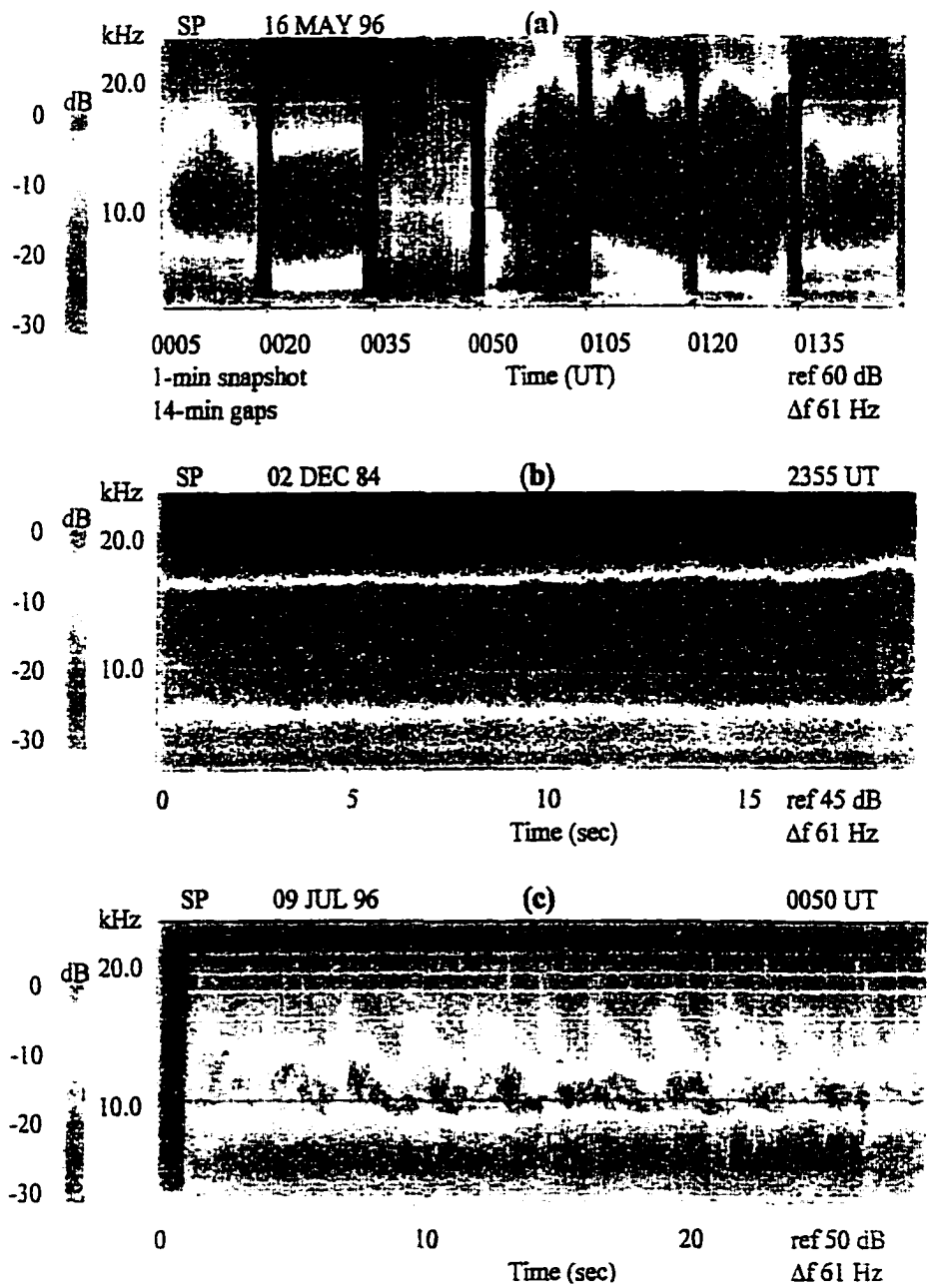

Figure 1.3.1. Examples of auroral hiss observed at South Pole, Antarctica. (a) AH spectra showing variation in time of upper and lower cutoffs. (b) Example of continuous auroral hiss (CAH). (c) Example of impulsive auroral hiss (IAH) showing dispersion.

at high latitudes in the evening and nighttime and on spacecraft in the auroral zone. Satellite and ground-based observations have provided lots of information on AH characteristics, morphology, association with visible aurora, substorm activity, and fluxes of energetic electrons [*Sazhin et al.*, 1993; *Sonwalkar*, 1995, and references therein] but the propagation of AH from the source region to the ground is poorly understood. However, the generation and propagation of AH from the source region to a high-altitude spacecraft is reasonably well understood. Standard whistler mode propagation theory in a smooth magnetosphere predicts that AH generated with large wave-normal angles along the auroral field lines by Cerenkov resonance cannot penetrate to the ground. This thesis presents a new mechanism of AH propagation to the ground. The model proposed in this thesis also explains the following salient features of AH that were poorly understood before:

1. AH has distinct spectral features. It is called continuous auroral hiss (CAH) when its spectrum is structureless and it remains steady over minutes and hours (Figure 1.3.1b). It is called impulsive auroral hiss (IAH) when its frequency-time spectrum is highly structured and it only fluctuates over seconds and also shows dispersion (Figure 1.3.1c). Both CAH and IAH have a low-frequency cutoff at a few kiloHertz, and a peak intensity at ~10 kHz. The upper cutoff frequency of CAH is ~30 kHz and that of IAH is several tens of kiloHertz, and at times can be up to several hundred kiloHertz.

2. The ground AH power spectral density is $\sim 10^{-16} - 10^{-14}$ Wm^{-2} Hz^{-1} [*Jorgensen*, 1968; *Tanaka et al.*, 1976] and is about 2-5 orders of magnitude smaller than the average AH power spectral density of $\sim 10^{-12} - 10^{-11}$ Wm^{-2} Hz^{-1} measured on satellites [*Barrington et al.*, 1971; *Gurnett and Frank*, 1972].

3. The ionospheric exit point of IAH is near the zenith where localized regions of bright aurora are observed [*Martin et al.*, 1960; *Helliwell and Morgan*, 1960]. The ionospheric exit point of CAH is located equatorward and is within ~600 km of a steady auroral arc [*Swift and Kan*, 1975; *Srivastava*, 1976].

4. IAH is associated with structured fluxes of precipitating electrons with energies ≥ 1 keV, and CAH is associated with rather structureless precipitating electrons with energies < 1 keV [*Hoffman and Laaspere*, 1972; *Mosier and Gur-*

nett. 1972; *Laaspere and Johnson*. 1973; *James*. 1973; *Beghin*. 1989; *Winningham and Heikkila*. 1974; *Ondoh et al*., 1981; *Ondoh* 1991].

5. AH is associated with visible aurora and substorms, but AH intensity and auroral luminosity or AE index often show no correlation [*Jorgensen*. 1969, 1979; *Makita*. 1979]. *Srivastava* [1976] has noted that at times AH is not observed at the time of auroral or magnetic activity, but auroral and magnetic activity always accompany AH.

6. On occasion, AH and radar events show very close time correlation. *Hower and Gluth*. [1965] have shown that AH in the 1 - 10 kHz band shows a strong correlation to 18 MHz radar echoes from the F region field-aligned irregularities. They found that all but one of the 33 hiss events that they observed were associated with 18 MHz radar events.

1.4 Importance of Present Work

In this thesis a new mechanism is proposed to explain the generation and propagation of VLF or auroral hiss (AH) from their source region to the ground. Standard whistler mode propagation theory in a smooth magnetosphere suggests that auroral Hiss generated with large wave-normal angles by Cerenkov resonance along auroral field lines cannot penetrate to the ground. In this thesis it is shown that AH can penetrate to the ground when they scatter from meter-scale irregularities. The study of auroral hiss (AH) is important because the generation and propagation of AH is closely related to the physics of auroral acceleration processes, auroral precipitation, visible aurora, and substorm activity. Auroral acceleration processes is important because the parallel electric field that drives the auroral ion beams transports ionospheric plasma. If there is a physical mechanism to relate optical and radar measurements of aurora, then plasma density enhancements and depletions can be remotely determined from the ground. AH is observed on the ground and on spacecraft and an understanding of its generation and propagation mechanism could be the physical mechanism to relate optical and radar data on aurora. The density depletions in the auroral zone are important because they are directly associated with the auroral acceleration

processes [*Persoon et al.*, 1988] and the generation of auroral kilometric radiation (AKR). The intensity of AKR and their generation mechanism affects the generation of other astrophysical radio sources that are important [*Benson and Calvert*, 1979; *Calvert*, 1981].

Meter-scale irregularities simulate lower hybrid (LH) waves when auroral hiss with large initial wave-normal angles impinge on them. LH waves are important because they couple both to electrons and ions. It is believed that LH waves are most efficient in heating suprathermal ions in the auroral region [*Lysak et al.*, 1980; Chang and Coppi, 1981]. If AH propagation to the ground is understood, the vertical extent of the meter-scale irregularities measured by radar at low altitudes can be interpreted and the LH wave intensity (simulated by AH) and region of occurrence can be determined.

Density measurements and LH wave intensity measurements to date have only been made on spacecraft. Study of AH and its propagation mechanism provides a mechanism to (1) make ground based measurements of density depletions along auroral field lines, (2) determine the vertical extent of meter-scale irregularities measured by radar at low altitudes, and (3) compute the intensity of LH waves simulated by AH. The advantage of a ground based system over the conventional use of satellites is that with receiving stations on the ground or with a singe receiving station on the ground receiving signals from multiple transmitters spaced in longitude, large scale measurements can be made over time-scales of hours. A ground-based system is also cost effective.

1.5 Contributions Made by the Present Thesis

This thesis presents a new mechanism of AH propagation from source region to the ground. AH propagation from source region to high latitude spacecrafts are well understood but AH propagation from source region to ground was not explained. By standard mode whistler propagation theory AH generated with large wave-normal angles along auroral field lines cannot penetrate the ground. However, AH is observed on the ground and this thesis provides a mechanism by which AH can penetrate the ground. The model and the new mechanism

is reported in the Journal of Geophysical Research [*Sonwalkar and Harikumar*. 2000].

The theory developed in this thesis provides a mechanism to remotely sense from the ground the plasma density and density depletions or cavities along the auroral field lines and the vertical extent of the meter-scale irregularities measured by radar at low altitudes. These measurements to date have only been made on spacecraft. The importance of these measurements is discussed in section 1.4. Ground-based remote sensing suggested in this thesis provides a method to study temporal changes in the auroral ionosphere and magnetosphere from a ground station over timescales of hours.

This thesis also provides a physical mechanism to relate auroral hiss observed on the ground to optical measurements of flux and characteristic energies of electrons and to radar measurements of aurora and meter-scale density irregularities. This AH propagation mechanism suggested in this thesis provides a method to estimate the intensity of lower hybrid waves simulated by auroral hiss. The measurement of LH waves simulated by AH is important and is discussed in section 1.4.

Another result shown in this thesis is that there is no conflict of AH source altitude region between satellite and ground observations of AH. Spacecraft data suggested that the source altitude for AH was somewhere between $\sim$ 5000 and 10,000 km altitude. [*Gurnett et al.*, 1983]. Ground Measurements [*Makita*, 1979] placed the AH source region at altitudes of $\sim$ 20,000 km. This thesis reinterprets the satellite data to show that AH source altitude can be anywhere between 5000 and 20,000 km altitude.

The present thesis has been partially reported in two referred journal articles *Sonwalkar et al.*, [2001], and *Sonwalkar and Harikumar* [2000], and the following conference proceedings *Sonwalkar et al.*, [2000], *Sonwalkar et al.*, [1999], *Harikumar and Sonwalkar* [1999], *Sonwalkar and Harikumar* [1999], *Sonwalkar and Harikumar* [1998], *Sonwalkar and Harikumar* [1997].

1.6 Organization of This Thesis Report

This thesis consists of four chapters. In Chapter 1. a background to the work done in this thesis is provided. In the first three sections of Chapter 1 a brief description of the Earth's magnetosphere. the whistler mode waves in the magnetosphere and auroral hiss is given. In the later part of the chapter an introduction is provided to the work done in this thesis and the contributions made by the present work.

Chapter 2 describes the new model to explain the generation and propagation of AH from its source in the magnetosphere to the ground station. Additionally. in this chapter the proposed model is compared to past work and also used to explain the ground-based observed features of AH.

Chapter 3 is a discussion of the geomagnetic field model. cold plasma density model and the linear model conversion model used in this thesis to describe the Earth's magnetosphere and the electrostatic-to-electromagnetic wave conversion in it. Chapter 3 also provides a description of the software programs used in this thesis.

Chapter 4 shows how the model described in chapter 2 can be applied to make inferences about the magnetosphere from ground-based auroral hiss dispersion data. One case of auroral hiss observed on July 09. 1996 at 0005 UT is analyzed in detail in section 4.3 of this chapter to show how the model proposed in this thesis can be used to invert the auroral hiss spectra to determine the field line(s) and the cold plasma density along that field line(s).

Chapter 5 concludes this thesis report with a summary of the work done in this thesis. In this chapter the model proposed in this thesis is compared with whistlers that are used to determine the cold plasma electron concentrations at low and mid latitudes. In section 5.2 a summary of the contributions made in this research is given and section 5.3 discusses avenues for future work.

2. Auroral Hiss Generation and Propagation From Source Region to the Ground

In this chapter, a new mechanism is proposed to explain auroral hiss propagation to the ground from its source region at high latitudes. By whistler mode propagation theory, auroral hiss generated with large wave-normal angles along the auroral field lines should reflect within the magnetosphere and not penetrate to the ground. In this chapter a model is developed to show how auroral hiss can penetrate to the ground.

2.1 Review of Previous Work

The currently accepted AH generation mechanism [*Swift and Kan*, 1975; *Maggs*, 1976, 1978; *Maggs and Lotko*, 1981; *Sazhin et al.*, 1993, and references therein; *Farrell et al.*, 1988, 1989] involves two steps. Auroral electrons with energies 0.1 - 10 keV during their motion down (or up) stimulate incoherent Cerenkov radiation. This radiation during its propagation is further amplified by a coherent amplification process. One theory suggested by the above authors with the exception of *Farrell et al.* [1988, 1989], is that a (beam-type) Cerenkov instability is responsible for the amplification process. *Farrell et al.* [1988, 1989] have suggested, based on the Spacelab 2 mission, that a plasma bunching instability may be responsible for the amplification of AH. A key feature of either theory is that the Cerenkov condition for wave generation by 0.1 - 10 keV electrons is satisfied for whistler mode waves at wave-normal angle θ (wave-normal angle with respect to the geomagnetic field) close to the whistler mode resonance cone angle θ_R. The theory predicts (1) a peak spectral density for AH at ~10 kHz, consistent with observations, and (2) an AH cutoff when AH electron fluxes fall below $10^4 - 10^5$ el $cm^{-2}s^{-1}ster^{-1}eV^{-1}$ [*Mosier and Gurnett*, 1972]. The theory is well supported by satellite observations of electron fluxes (energy range and limiting value) and the AH propagation from the source region to a spacecraft at $\theta \sim \theta_r$ [*Mosier and Gurnett*, 1969; *Gurnett et al.*, 1983; *Sazhin et al.*, 1993]. In this thesis, it is assumed that AH has been generated by Cerenkov resonance

at $\theta \sim \theta_R$ and that it has been amplified by a coherent amplification process.

VLF wave propagation theory in a smooth magnetosphere predicts that a whistler mode wave propagating at large θ will undergo reflection within the magnetosphere at an altitude where the wave frequency $f = f_{LHR}$, where f_{LHR} $(= ((\text{mass}_{ion}/\text{mass}_{electron})(f_{pe}^{-2} + f_H^{-2}))^{-0.5})$ is the lower hybrid resonance frequency [*Kimura*, 1966]. For a typical auroral magnetosphere the maximum value of f_{LHR} ranges from 2-15 kHz depending on the density model. Thus one would expect waves < 2 to 15 kHz to be reflected due to LHR reflection. Higher-frequency waves ($f > f_{LHR}$) will undergo total internal reflection (by Snell's law) at the Earth-ionosphere boundary where the refractive index (μ) of whistler mode waves in the ionosphere is $\gg 1$. *Siren* [1972, 1975] and *Makita* [1979] have tried to explain AH propagation to ground in terms of ducted propagation. *Siren* [1975] performed a dispersion analysis on impulsive hiss assuming that auroral hiss was propagating with its wave normal parallel to the geomagnetic field, an assumption that is not valid for auroral hiss which is generated at large wave-normal angles. *Makita* [1979] assumed that a magnetospheric duct terminates abruptly at 3000 km where hiss exits at all possible wave-normal angles. A part of the AH that has the appropriate wave-normal angles then falls into the transmission cone and reaches the ground. The abrupt duct termination condition is physically unrealistic and does not agree with conclusions of *Bernhardt and Park* [1977], who estimated that the magnetospheric duct terminates at 3000 km and then merges with the background ionosphere with scale heights of 800 – 1800 km. There is also a discrepancy in the source altitude location of AH as determined from the spacecraft and ground observations. Ground observation estimates by *Siren* [1972, 1975] and *Makita* [1979] place the AH source altitudes at values ~20,000 km for 10 kHz AH. Satellite observations and analysis of one case of AH data from the DE 1 satellite by *Gurnett et al.* [1983] estimate source altitudes for 10 kHz AH in the range of 4459-5733 km. Recently, *Matsuo et al.* [1998] have proposed that large-scale (~10-100 km) irregularities can bend the AH wave-normal angles sufficiently to fall in the transmission cone. They assume an initial wave-normal angle of $\sim 10°$ away from the resonance cone angle for a frequency of 5 kHz (at source heights of ~5000 km). At this wave-normal angle the resonant energies of electrons required to generate AH are about ~150 keV.

which is too high compared to <10 keV electrons associated with the generation of AH. In this thesis it is shown that both ducted and nonducted whistler mode waves with large initial wave-normal angle cannot reach the ground even if large-scale density gradients present in the ionosphere are taken into account. An additional mechanism, scattering of AH by meter-scale irregularities, presented in this thesis, is required for AH to penetrate the Earth-ionosphere boundary.

2.2 New Model of Auroral Hiss Propagation to the Ground

The schematic of Figure 2.2.1 explains the main ideas of the model and shows an experimental arrangement that can be used to test the ideas presented in this thesis. AH is assumed to be generated at large wave-normal angles on auroral field lines at ~5000 - 20,000 km via Cerenkov resonance. It then propagates to lower altitudes (3000 - 5000 km) by two different modes of propagation: IAH propagates in field-aligned density depletions and enhancements (ducts) and CAH propagates in the nonducted mode. Both types of AH reach the lower altitude with large wave-normal angles, and would in general be reflected at these altitudes either by LHR reflections or by total internal reflection at the Earth-ionosphere boundary. The model proposes that the meter-scale (1-100 m) irregularities present at altitudes < 5000 km scatter a small fraction (0.1-10%) of the incident large wave-normal whistler mode waves into small wave-normal waves, which can then propagate to the ground without being totally internally reflected. In this chapter AH propagation to the ground is discussed in four stages: (1) source or generation region, (2) propagation from the source region to altitudes of ~ 5000 km (topside ionosphere), (3) scattering by meter-scale irregularities in the ionosphere, and (4) penetration to the ground at the Earth-ionosphere boundary.

Two software programs were used to derive the results shown in this thesis. They are (1) the Stanford two-dimensional (2-D) ray-tracing program [*Burtis*, 1974], and (2) the full wave linear scattering program developed by *Ngo* [1989] and modified in this thesis to perform numerical calculations. These two programs are discussed in chapter 3 of this thesis. In all the calculations for this chapter,

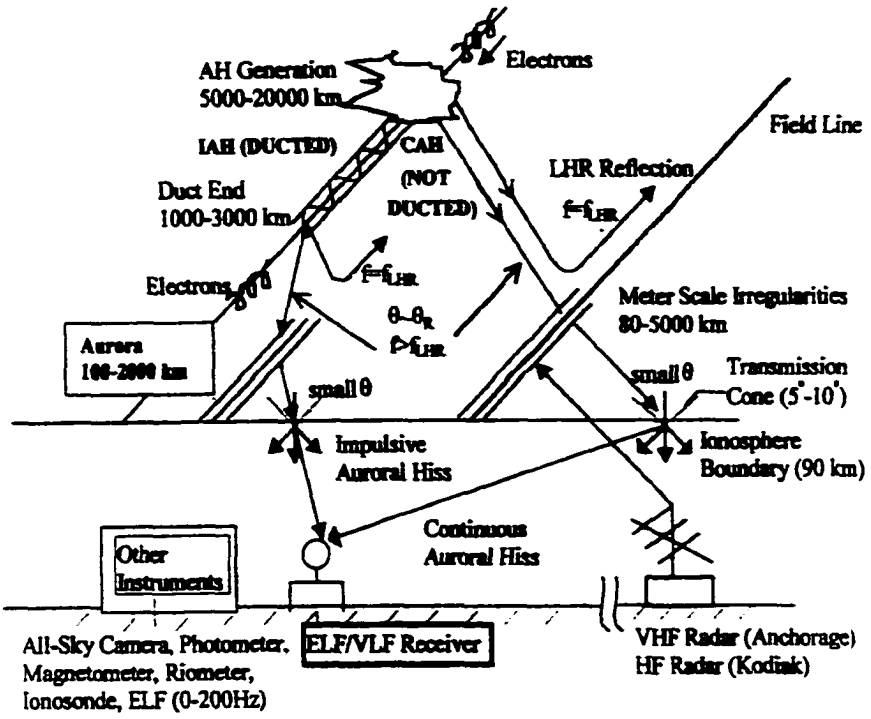

Figure 2.2.1. Schematic illustrating the proposed propagation of hiss from source region to a ground based experimental setup including a VLF receiver, photometer, all sky camera, and radar. AH generated at high altitudes ($\sim 5000 - 20,000$ km) propagates to lower altitudes (<5000 km) in a ducted (IAH) or nonducted (CAH) mode. The hiss with large θ arriving at <5000 km altitude is scattered by meter-scale irregularities, and about 1 - 10% of the scattered hiss has small θ that can penetrate to the ground. The schematic also shows various instruments that can be used to observe the hiss that is scattered by the meter-scale irregularities. LHR denotes lower hybrid resonance.

the plasmapause was defined at $L = 4$. and a density variation of $R^{-4.5}$ was assumed outside the plasmapause. References to reference density $N_{e,ref}$ refers to electron density at 2 R_E altitude and 70° invariant latitude. The reference density ($N_{e,ref}$) is varied between 1 and 100 el cm^{-3}. The reference densities < 25 generally represent the low-density auroral cavity [*Persoon et al.*, 1988] and those between ~ 25 and 100 represent the high-density auroral region equatorward and poleward of the low density auroral cavity [*Gurnett*, 1978; *Persoon et al.* 1983]. Figure 2.2.2 shows the important parameters for the density model, including gyrofrequency f_H, electron plasma frequency f_{pe}, and lower hybrid frequency f_{LHR} as a function of altitude along the $\Lambda = 70°$ ($L = 8.55$) field line for $N_{e,ref} = 1$, 10, and 100 el cm^{-3}. All ray-tracing calculations based on this model were performed for frequencies between 3 and 30 kHz that are commonly observed on the ground, but the results will be illustrated for 10 kHz, the frequency at which both IAH and CAH show a spectral peak. IAH can occasionally have frequencies >100 kHz, and the results discussed in this thesis are applicable for those frequencies also.

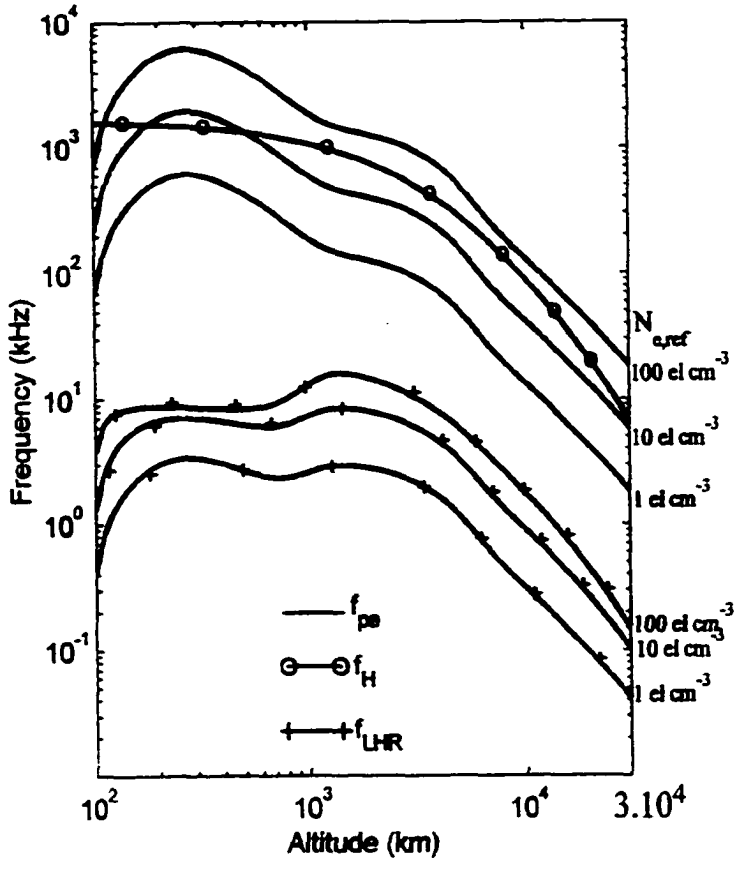

Figure 2.2.2. Values of frequencies f_H, f_{pe}, and f_{LHR}, as a function of altitude along the L = 8.55 field line for three density models: $N_{e,ref}$=1, 10, and 100 el cm^{-3}. The electron density refers to cold plasma density at a reference altitude of 2 R_E and invariant $\Lambda = 70°$.

2.3 The Source Region and Generation of Auroral Hiss

Spacecraft and ground-based observations of auroral hiss place the source region of AH at completely different altitudes. Ground observations by *Siren* [1972, 1975] and *Makita* [1979] place AH source altitudes at $\sim$ 20,000 km altitude for 10 kHz AH. *Gurnett and Frank* [1972] place the source of auroral hiss at altitudes between 5000 and 10,000 km in the polar ionosphere. They based these numbers on the V-shaped low frequency cutoff of whistler radiation that they observed at low altitudes. *Gurnett et al.*, [1983] estimate source altitudes for 10 kHz AH in the range of 4459-5733 km from satellite observations and analysis of one case of AH data from the DE 1 satellite. The above authors suggest that the "funnel" shaped frequency-time spectrum of AH that they observed from the DE-1 satellite is characteristic of radiation emitted from a spatially localized source below the spacecraft and hence the source altitude of 10 kHz AH is $\sim 4459 - 5733$ km. In this thesis the satellite data is reinterpreted to show that the AH source altitude need not be limited to $\sim$ 6000 km altitude because of a "funnel" shaped frequency-time spectrum of AH. This thesis shows that a "funnel" shaped frequency-time spectrum of AH is possible when the emitting source is both above or below the satellite.

For wave-normal angles (θ) close to the resonance cone angle (θ_{res}) the ray direction is perpendicular to the resonance cone. At $\theta \sim \theta_{res}$, auroral hiss from a point source produces a "funnel" shaped spectrum [*Gurnett et al.*, 1983]. The "funnel" shaped spectrum is caused by the frequency dependence of the whistler wave propagating along the magnetic field line. If the ray makes an angle w_{res} with the resonance for a wave-normal angle θ_{res} then from *Gurnett et al.*, 1983, neglecting ion effects for a high density approximation model

$$\tan^2 w_{res} = \frac{f^2 f_{pe}^2}{(f_{pe}^2 - f^2)(f_H^2 - f^2)} \qquad (2.3.1)$$

From the above equation it is seen that the characteristic funnel shape of AH is due to low frequencies propagating along the magnetic field line and the high

frequencies propagating at large angles to the magnetic field line. *Gurnett et al.*, 1983 state that the funnel shape of the spectrum is a result of particle interaction with the wave traveling in the same direction as the upgoing particle and hence the source region of the hiss has to be below the spacecraft. Likewise, particle interaction with the wave traveling in the same direction as the downcoming particle can produce an inverted funnel shape spectrum. Figures 2.3.1(a-b) show a "funnel" shaped frequency-time spectrum for source regions for AH sources located below (Figure 2.3.1a) and above (2.3.1b) the spacecraft. In Figure 2.3.1a, the source region is at an altitude of 5000 km and is below the spacecraft and in Figure 2.3.1b the source region is 5000 km above the spacecraft.

Based on the above discussion and Figures 2.3.1(a,b), the source region for AH is assumed to be somewhere between $\sim$ 5000 and 20,000 km, depending on frequency. For this thesis, the choice of the source region for auroral hiss includes the source region altitudes suggested by both ground and satellite measurements [*Siren* 1972, 1975; *Makita*, 1979; *Mosier and Gurnett*, 1969; *Gurnett et al.*, 1983]. The altitude-dependent AH generation model of *Maggs and Lotko* [1981] suggests that the strongest power fluxes of AH are likely to occur in the altitude range of a few thousand kilometers. In this thesis, it is assumed that AH is generated by Cerenkov resonance given by the following expression:

$$V_{\|} \cos\theta = V_{ph} = \omega/k,$$

or equivalently,

$$\mu \cos\theta \approx 510/\sqrt{E_{\|}(eV)}. \qquad (2.3.2)$$

where $V_{\|}$, V_{ph} are the parallel velocity of the electron and phase velocity of the wave, respectively, θ is the wave-normal angle, $\omega = 2\pi f$ is the angular frequency, k is the whistler mode wave number, μ is the whistler mode refractive index, and $E_{\|}$ is the parallel energy of the resonant electron. Past work has shown that AH is generated by 0.1-10 keV electrons [*Hoffman and Laaspere*, 1972; *Mosier and Gurnett*, 1972; *Laaspere and Johnson*, 1973; *James*, 1973; *Beghin et al.*, 1989; *Winningham and Heikkila*, 1974; *Ondoh et al.*, 1981; *Ondoh*, 1991].

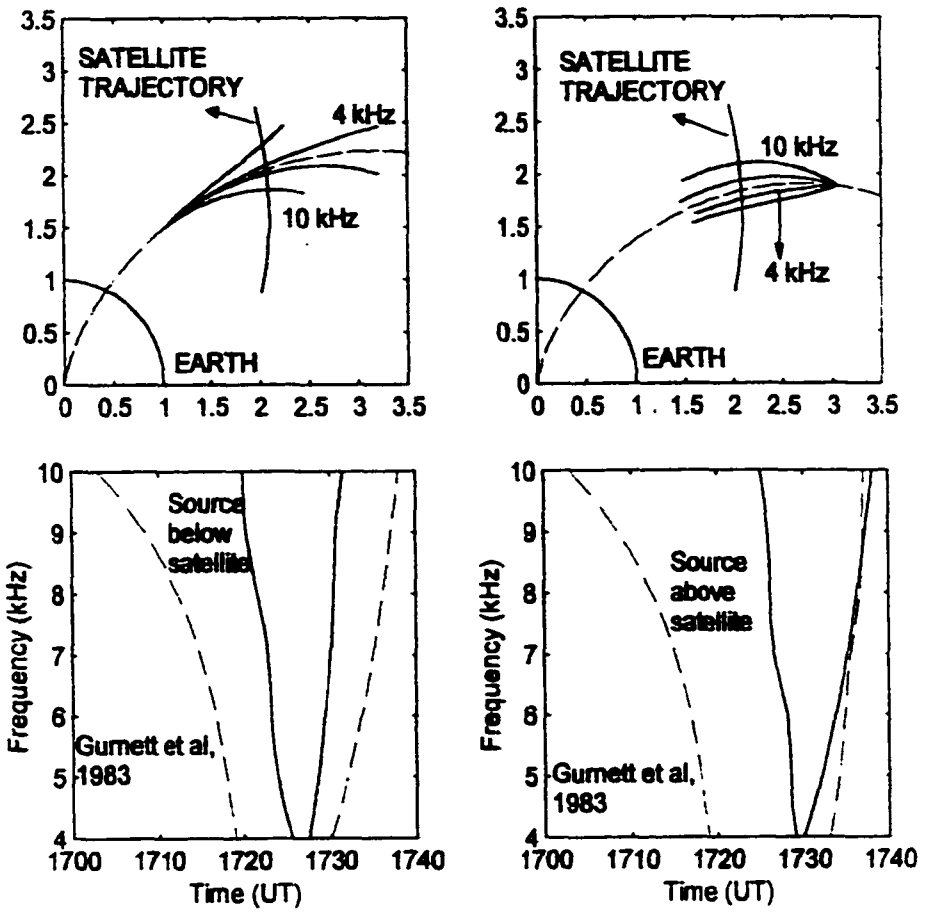

Figure 2.3.1 Raytracing examples to show that source altitudes above and below the satellite produce a funnel shaped spectrum.

Thus at any given altitude, and for a given plasma density, using equation (2.3.2), the range of initial wave-normal angles of AH as a function of frequency that can be generated by 0.1 - 10 keV electrons can be determined. Figures 2.3.2(a-h) show the initial wave-normal angles as a function of energy for 3, 10, and 30 kHz frequency waves at four different altitudes, for reference density $N_{e,ref}$=10 el cm^{-3} and 50 el cm^{-3}, respectively. For 0.1-10 keV resonant electrons the initial wave-normal angles θ at the source are close (within a degree or so) to the resonance cone angle θ_R.

The upper altitude limit on the generation region for a given frequency (f) is given by the whistler mode upper frequency cutoff $f = \min(f_H, f_{pe})$ (Figure 2.2.2) because when $f > f_{pe}$ or $f > f_H$, the wave is no longer a whistler mode wave. At low altitudes, when $f < f_{LHR}$, the resonance condition is not satisfied for $E_{||}$ in the 0.1-10 keV energy range. For example, a 10 kHz wave injected at 10,000 km altitude is LHR reflected at $\sim$ 2730 km altitude, and the $E_{||}$ of the wave at this altitude is $\sim 6.8 \times 10^5$ keV. The reference density used in the above example is 45 el cm^{-3} defined at an altitude of 2 R_E and $\Lambda = 70°$. Thus the altitude at which $f \leq f_{LHR}$ may determine the low-altitude limit on the generation region for the given frequency. Figure 2.2.2 shows the f_{LHR} values for a range of density models from which the low-altitude limit for the generation region of AH for a given frequency can be estimated. At 5000 km altitude, $f_{LHR} > 3$ kHz, and therefore a 3 kHz wave cannot be seen at this altitude, as discussed above. It is also the reason why 3 kHz waves are not shown in Figures 2.3.2a and 2.3.2b. High-frequency waves $\geq$ 30 kHz are not generated at altitudes $\geq$ 15,000 km since 30 kHz is greater than $\min(f_{pe}, f_H)$ at that altitude. Figure 2.3.2 also illustrates the frequency and altitude dependence of waves as a function of energy ($E_{||}$) and initial wave-normal angle (θ). For a given altitude, frequency, and $E_{||}$, θ can be further away from θ_R for high densities. For example, a 10 kHz wave generated by 1 keV electrons at 10,000 km altitude is $\sim 0.05°$ away from θ_R for $N_{e,ref} = 10$ el cm^{-3} but the same wave is $\sim 0.1°$ away from θ_R for $N_{e,ref} = 50$ el cm^{-3} (Figures 2.3.2c and 2.3.2d). For a given density model, frequency, and parallel resonant energy, as the injection altitude increases the same wave can be injected further away from θ_R. Finally, for a given altitude, density, and parallel resonant energy, $(\theta - \theta_R)$ is smaller for smaller frequencies.

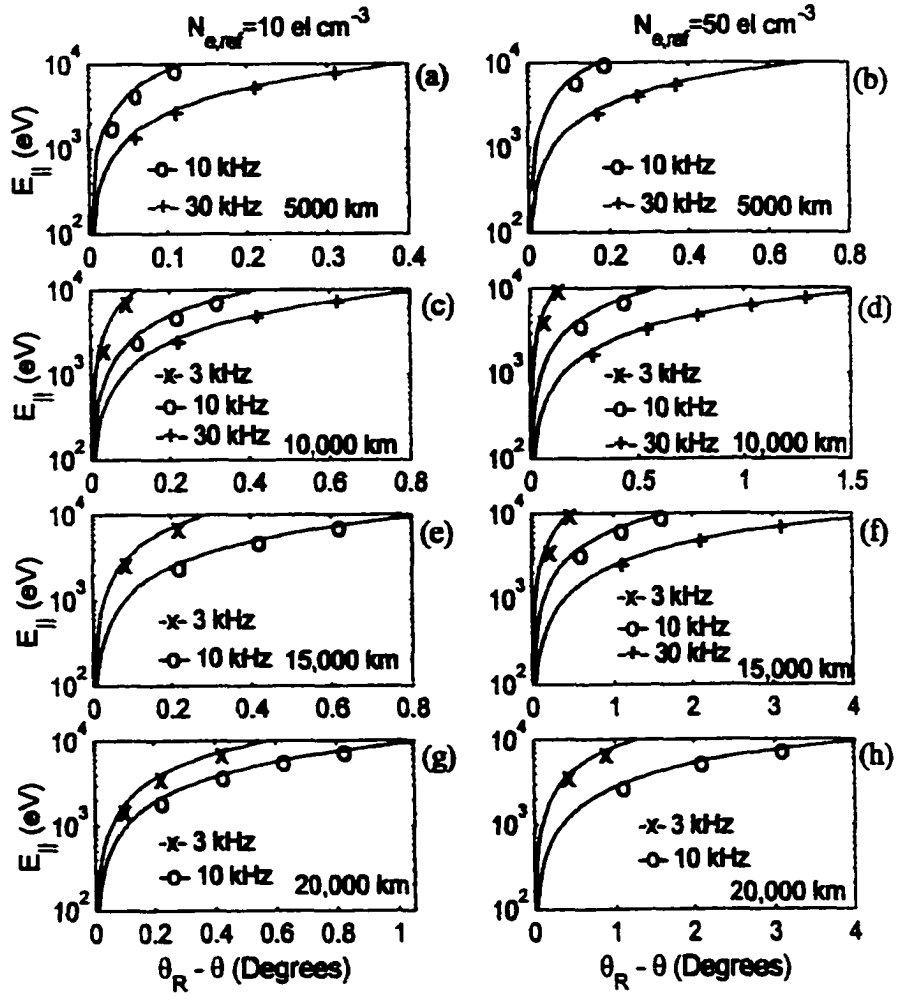

Figure 2.3.2. Parallel resonant energy ($E_{||}$) as a function of $(\theta - \theta_R)$, where θ is the injected wave-normal angle and θ_R is the resonance cone angle, for different wave frequencies and different injection altitudes on the $L = 8.55$ field line. (a) $N_{e,ref} = 10$ el cm^{-3} and altitude is 5000 km. (b) $N_{e,ref} = 50$ el cm^{-3} and altitude is 5,000 km. (c) $N_{e,ref} = 10$ el cm^{-3} and altitude is 10,000 km. (d) $N_{e,ref} = 50$ el cm^{-3} and altitude is 10,000 km. (e) $N_{e,ref} = 10$ el cm^{-3} and altitude is 15,000 km. (f) $N_{e,ref} = 50$ el cm^{-3} and altitude is 15,000 km. (g) $N_{e,ref} = 10$ el cm^{-3} and altitude is 20,000 km. (h) $N_{e,ref} = 50$ el cm^{-3} and altitude is 20,000 km. (Please see text for details).

This dependence of $(\theta - \theta_R)$ on frequencies can be explained qualitatively as follows. For $(f_{pe} \gg f_H)$, $\cos\theta \approx \cos\theta_R \approx f/f_H$. For low frequencies the ratio f/f_H is small and thus cos θ is small. For high frequencies the ratio f/f_H is relatively large and thus cos θ is large. Similarly, for $(f_{pe} \ll f_H)$, $\tan^2(\theta_R) \approx (f_{pe}^2/f^2 - 1)$, and similar results are observed. Thus, at a given altitude for a given energy of electrons, cos θ is much smaller for lower frequencies and therefore the μ required to satisfy equation (2.3.2) is large, and this requires θ to be much closer to θ_R compared to the θ at higher frequencies. The above inferences are used in section 2.4 to show that IAH observed on the ground is generated at higher altitudes for lower frequencies, giving the observed frequency dispersion on the ground. The relationships shown in Figure 2.3.2 hold for $f_{pe} \gg f_H$ and $f_{pe} \ll f_H$. At the limit, when $f \approx f_H$ or $f \approx f_{pe}$, the relationships shown in Figure 2.3.2 fail for that altitude or density model, respectively. Chapter 4 analyzes the above cases in terms of auroral hiss dispersion observed on the ground.

2.4 Propagation of Auroral Hiss From the Source Region to the Topside Ionosphere

Once the wave is launched in the source region with its initial wave-normal angle $\theta \sim \theta_R$ pointing downward, it can propagate in two distinct propagation modes: (1) ducted mode (Figure 2.4.1a), in which a wave (ray) is trapped in field-aligned density enhancements or depletions called ducts, and (2) nonducted mode (Figure 2.4.1b), in which a ray departs from the initial field line. The ducted propagation, when $\theta \sim \theta_R$, is very different from conventional ducted propagation of lightning-generated whistlers which start with initial $\theta \sim 0°$. In the case of lightning-generated whistlers, θ remains close to 0° throughout the wave's course of propagation. For both ducted and nonducted propagation with initial $\theta \sim \theta_R$, the wave-normal angle θ continues to increase as the wave propagates downward. In both ducted and nonducted cases, the wave is reflected at an altitude where the wave frequency f is equal to the local f_{LHR}. For waves with $f > f_{LHR}$, the waves are total internally reflected at the Earth-ionosphere boundary.

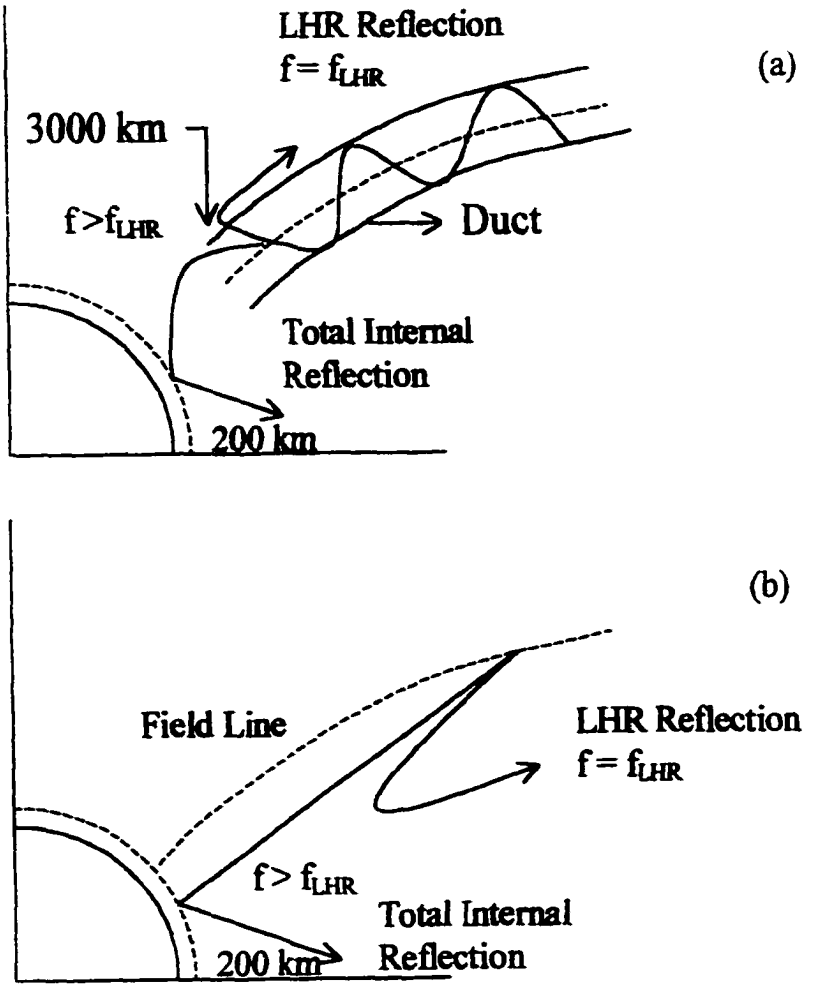

Figure 2.4.1. (a) Schematic illustrating ducted (IAH) wave propagation, and LHR and total internal reflection. (b) Schematic illustrating nonducted (CAH) wave propagation, and LHR and total internal reflection.

In this thesis, it is proposed that IAH propagates from the source region to a lower altitude (< 5000 km) in the ducted mode and CAH propagates in the nonducted mode. The two distinct propagation modes were chosen for AH based on the following considerations. (1) IAH shows dispersion characteristics of ducted propagation in which different frequency waves originate at different altitudes and propagate with different group velocities [*Siren*, 1972, 1975]. (2) IAH is observed when there is a visible aurora overhead [*Martin et al.*, 1960; *Helliwell and Morgan*, 1960], whereas CAH is observed <600 km equatorward of the associated visible aurora [*Swift and Kan*, 1975; *Srivastava*, 1976]. (3) IAH is associated with rather structured electron fluxes with $E_{||} \sim 1 - 10$ keV, while CAH is associated with structureless electron fluxes with $E_{||} \approx 0.1 - 1$ keV [*Hoffman and Laaspere*, 1972; *Mosier and Gurnett*, 1972; *Laaspere and Johnson*, 1973; *James*, 1973; *Beghin et al.*, 1989; *Winningham and Heikkila*, 1974; *Ondoh et al.*, 1981; *Ondoh* 1991]. The initial wave-normal angles corresponding to $E_{||} >$ 1 keV are small enough to be trapped in field-aligned ducts, while the initial wave-normal angles corresponding to $E_{||} \approx 0.1 - 1$ keV are too large to be trapped in ducts. Figure 2.4.2a and Figure 2.4.2b show the initial wave-normal angles as a function of energy for several reference densities. Figure 2.4.3 shows two examples of a limiting value (θ_{trap}) of initial wave-normal angles beyond which rays cannot be trapped in density depletions or enhancements. From Figure 2.4.3 it is seen that the initial θ of waves generated by resonant electrons with $E_{||} <\sim 1$ keV is too close to θ_R to be trapped by even large amplitude ducts ($\Delta N_e \sim \pm 90\%$). For example, in Figure 2.4.3a, rays with $\theta < 75.07°$ for $N_{e,ref} = 10$ el cm^{-3} can be trapped, but rays with $\theta > 75.07°$ cannot be trapped. Figure 2.4.3b shows similar results for $N_{e,ref} = 50$ el cm^{-3}. Later in this thesis report, it will be seen that this picture is consistent with other observed properties of IAH and CAH.

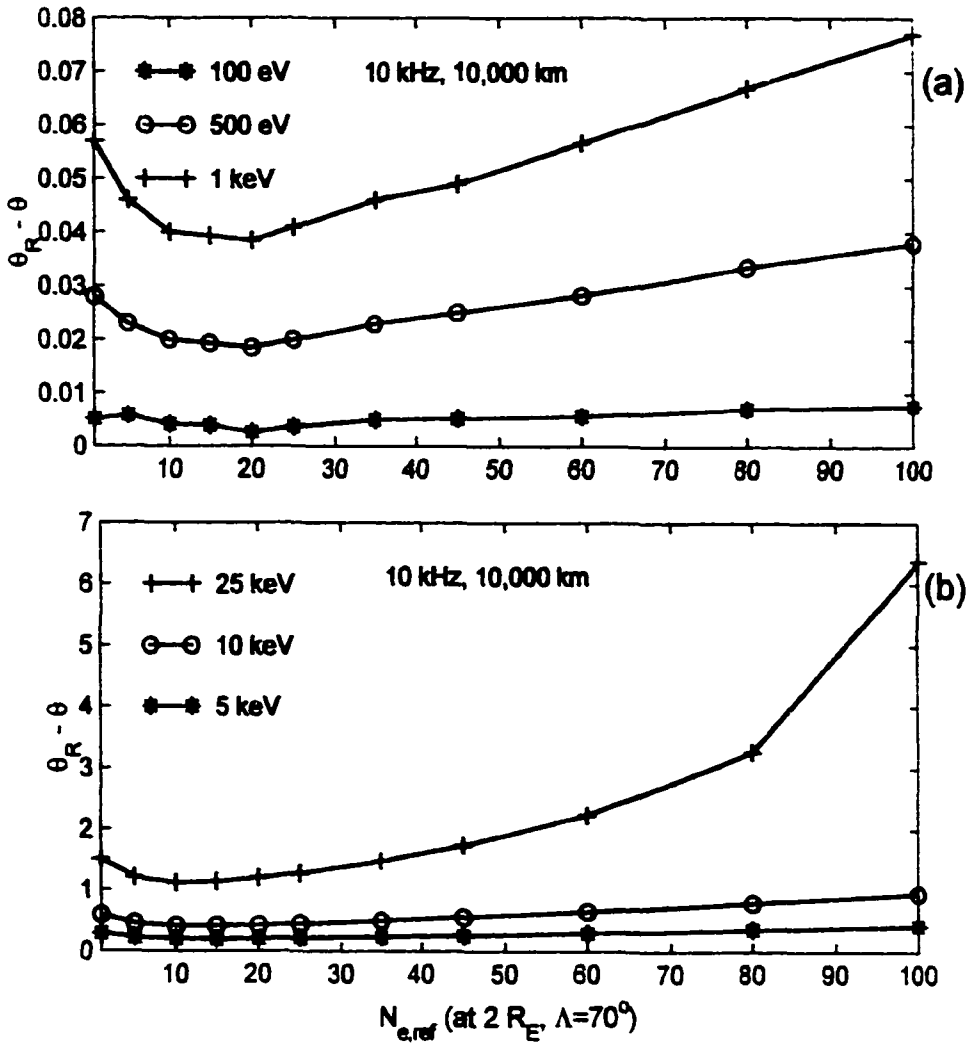

Figure 2.4.2. Plots of $(\theta_R - \theta)$ where θ is the injected wave-normal angle and θ_R is the resonance cone angle, as a function of several reference densities for various values of $E_{||}$: (a) $E_{||}$ in the 100 eV to 1 keV range. (b) $E_{||}$ in the 5 keV to 25 keV range.

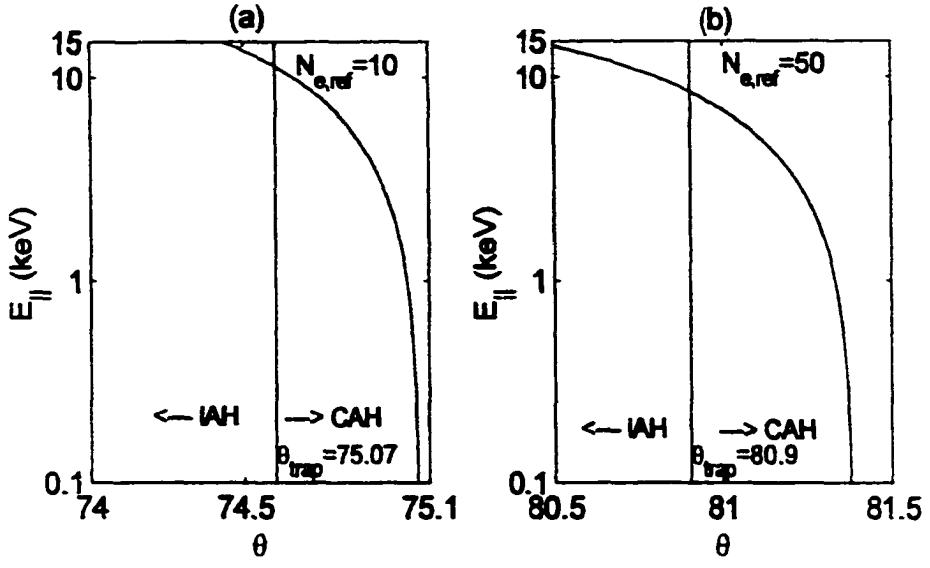

Figure 2.4.3. Parallel resonant energy ($E_{||}$) as a function of initial wave-normal angle θ for two reference densities. The energy was calculated for a 10 kHz wave injected at 10,000 km altitude in a −90% duct. For $\theta < \theta_{trap}$ the waves can be trapped in the duct whereas for $\theta > \theta_{trap}$ the waves cannot be trapped in the duct. (a) $N_{e,ref} = 10$ el cm^{-3}. (b) $N_{e,ref} = 50$ el cm^{-3}.

The resonant conditions required for the trapping of 10 kHz IAH generated at 10.000 km altitude by enhancement and depletions of various amplitudes are shown in Figure 2.4.4. For a given reference density $N_{e,\mathrm{ref}}$ at 2 R_E and duct amplitude $\Delta N_e/N_e$, using the ray-tracing program, the largest wave-normal angle θ_{trap} that can be trapped within the duct is calculated. A ray is defined as trapped if it remains close to the field line up to about ~3000 km altitude (so that the ray reaches the region of meter-scale irregularities discussed in the section 2.6). Using equation (2.3.2) and θ_{trap}, the minimum energy $E_{\parallel,\mathrm{min}}$ of the resonant electron that can generate AH that can be trapped in the given duct is calculated. The Figure shows that (1) density depletions are required to trap AH generated by <10 keV electrons, (2) the larger the amplitude of the depletions, the smaller the energy of the resonant electrons that generate AH, (3) AH generated by $\leq$ 1 keV electrons cannot be trapped at all, and (4) as the reference density increases, the waves are better trapped by both enhancements and depletions. The third result implies that AH generated by $\geq$ 1 keV electrons can be trapped by depletions, but AH generated by $<\sim$ 1 keV electrons cannot be. Duct widths as small as 0.005 L and as large as 0.1 L gave similar results. Similar results were also obtained for AH generation at different altitudes in the 5.000 - 20.000 km range and in the 3 - 30 kHz range. *Persoon et al.* [1983, 1988] have shown that density depletions up to $\Delta N_e \sim -99\%$ and $\Delta L \sim 0.001-0.2$ are commonly present in the auroral ionosphere, supporting the hypothesis about the assumed ducted mode of propagation for IAH. Ducted propagation may provide the answer as to why IAH is observed near the zenith where visible aurora is observed. From Figure 2.3.2, for a given altitude and given energy of electrons the initial wave-normal angle θ is closer to θ_R for lower frequencies. As the altitude increases, θ can be relatively further away from θ_R and thus will be easier to trap (Figure 2.3.2). Therefore it is assumed that IAH observed on the ground is generated at higher altitudes by the low frequencies and at lower altitudes by higher frequencies, giving rise to the observed dispersion. *LaBelle et al.* [1998] used data from AGO-P1 to discuss the AH observed at high geomagnetic latitudes. They estimated a rather low source altitude of $2000-5000$ km for hiss frequencies between 40 and 80 kHz.

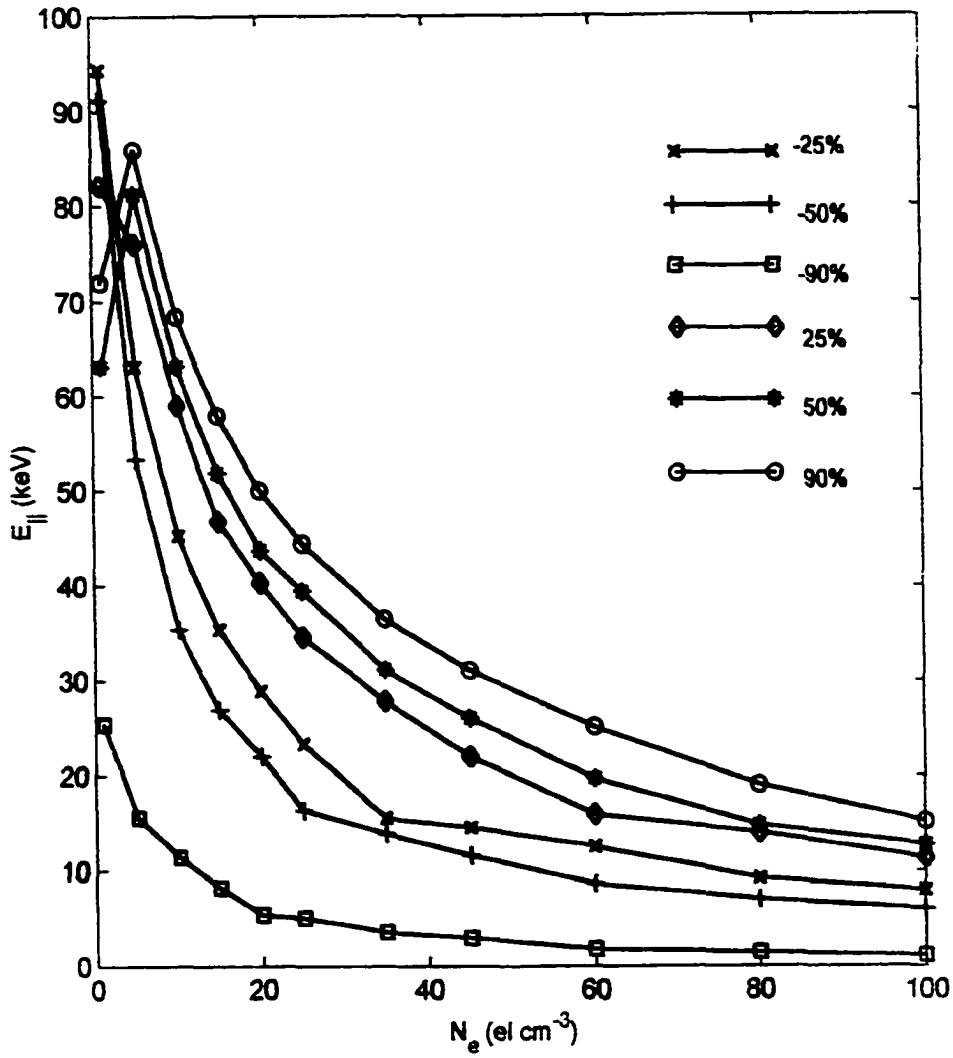

Figure 2.4.4. Minimum parallel resonant energy for 10 kHz ducted waves injected at 10,000 km altitude as a function of the reference density. As the density increases, waves are better trapped for all duct enhancements and depletions. Density depletions trap IAH generated by 1 – 10 keV electrons.

The upper frequency cutoff of IAH observed on the ground is most likely determined by a combination of several factors: (1) the energetic electron energy and flux and the wave growth they provide [*Yamamoto*, 1979; *Maggs and Lotko*, 1981]. (2) the density enhancement or depletion present to trap the waves, and (3) Landau damping as discussed below. The lower frequency cutoff of IAH is discussed in section 2.7.

As different frequency waves propagate at different speeds, a dispersion is observed in the IAH spectrum recorded on the ground. The observed dispersion of IAH (3-12 kHz) is of the order of ~ 35-200 ms [*Siren*, 1972]. From Figure 1.3.1 a dispersion time of ~ 1 s for frequencies between 7 and 17 kHz is observed. Calculations of the dispersion time over a 3-30 kHz frequency range for different frequencies generated at different altitudes in this thesis gives dispersion in the range of a few tens of milliseconds to 1 second, consistent with observations.

CAH, propagating in the nonducted mode, departs from the source field line and reaches a lower altitude of a few hundred kilometers from the ionospheric footprint of the source field line. This propagation path explains why CAH ionospheric exit points are a few hundred kilometers away from the location of the aurora. The equatorward detection of CAH exit points is related to transmission conditions at the Earth-ionosphere boundary as discussed in section 2.7.

Landau damping may be an important factor in the propagation of AH [*Morgan et al.*, 1994]. As CAH and IAH propagate downward, the wave-normal angle θ continues to increase toward θ_R and thus makes Landau damping significant [*Draganov et al.*, 1993]. The increased Landau damping with increasing frequency in the auroral magnetosphere may explain the observed upper frequency cutoff of CAH at ~30 kHz. The parallel resonant energy of electrons generating CAH is much lower than the parallel resonant energy of electrons generating IAH (Figure 2.4.2 and Figure 2.4.4). As Landau damping is expected to increase as the parallel resonant energy decreases. Landau damping of CAH at a given frequency is greater than the Landau damping of IAH. Hence IAH has a higher upper cutoff frequency compared to CAH, as observed. The lower cutoff frequency of CAH is discussed in section 2.6. The higher-frequency AH observed on the ground is most probably generated closer to the ground, because Landau damping is higher for higher frequencies.

The observed lower limit for the AH wavelength is $\sim$ 1 km according to *Morgan et al.* [1994]. The wavelength estimated by *Morgan et al.* [1994] is specific to their experiment and is for an upward propagating AH from a source at 10.000 km altitude. The AH wavelength measured from an auroral sounding rocket by *Ergun et al.* [1991] was $\sim$ 100 m. The wavelengths calculated at 5000 km altitude for a 10 kHz CAH generated by 1 keV electrons at 10.000 km altitude are of the order of 0.1 km for the high-density model ($N_{e,ref}$ = 100 el cm^{-3}) and 1.2 km for the low-density model ($N_{e,ref}$ = 1 el cm^{-3}). in this thesis. For 10 kHz waves generated at 10.000 km altitude it was found that the range of λ. measured at 5000 km altitude. for IAH propagating through a -90% duct for reference densities between 1 and 100 el cm^{-3} is 7 km to 0.3 km. These numbers are consistent with the estimated wavelengths by *Morgan et al.* [1994] and *Ergun et al.* [1991].

From the discussion presented in this section it is suggested that (1) IAH propagates in a ducted mode. (2) CAH propagates in a nonducted mode. (3) the upper frequency cutoff of CAH is probably determined by Landau damping. (4) IAH suffers less Landau damping compared to CAH and has a larger upper cutoff frequency compared to CAH at lower altitudes. (5) the hiss observed on the ground corresponds to higher-frequency waves generated at lower altitudes rather than to lower-frequency waves generated at higher altitudes. (6) the dispersion observed in the IAH spectra is from the different frequency waves that propagate from different source altitudes at different speeds to the ground. and (7) lower frequencies are generated at a higher altitude and higher frequencies are generated at a lower altitude. a result also suggested by previous studies [*Maggs*. 1976: *Siren*. 1972. 1975].

2.5 Reflection of Auroral Hiss at Low Altitudes

Both IAH and CAH arrive at low altitudes (<3000 km) with large wave-normal angles and are reflected by one of the two mechanisms. If the wave encounters a region where $f = f_{LHR}$. the wave is reflected by the LHR reflection mechanism [*Kimura*. 1966]. For example. from Figure 2.2.2. for a high-density

model ($N_{e,ref}$ = 100 el cm^{-3}) a 10 kHz wave will be reflected by LHR reflection near 3000 km altitude. However, for a lower-density model, the 10 kHz wave can propagate to lower altitudes ($\sim$ 200 km) without being LHR reflected. If $f > f_{LHR}$, AH continues to propagate to lower altitudes and is totally internally reflected if $\mu(\theta)\sin\delta > 1$, where δ is the wave-normal angle with respect to the vertical. Figures 2.5.1 and 2.5.2 show that in a smooth magnetosphere CAH and IAH, respectively, will always be reflected back into the magnetosphere. Specifically, Figure 2.4.1a shows a value of $\mu(\theta)\sin(\delta) \gg 1$ at $\sim$ 200 km altitude for a 10 kHz wave injected at 10,000 km altitude. Figure 2.5.1b shows that at high reference densities the wave undergoes LHR reflection within the magnetosphere. Figure 2.5.2 illustrates the reflection of IAH waves in a ($\Delta N_e = -90\%$) duct back into the magnetosphere. The rays were injected at 10,000 km with θ values as shown in Figure 2.5.2a. Figure 2.5.2b shows the energy required to trap the waves. Figure 2.5.2c shows that $\mu(\theta)\sin\delta$ at $\sim$ 200 km is in general $\gg 1$ for IAH (and CAH as seen in Figure 2.5.1) and thus by Snell's law, both ducted (Figure 2.5.2) and nonducted (Figure 2.5.1) waves will be totally internally reflected at the Earth-ionosphere boundary and cannot reach the ground. If rays are injected with θ values as shown in Figure 2.5.2d, the rays undergo LHR reflection at the different altitudes shown in Figure 2.5.2f for different densities. Figure 2.5.2e shows the energy required to trap the waves injected in Figure 2.5.2d. Thus both ducted (IAH) and nonducted (CAH) waves are either totally internally reflected at the Earth-ionosphere boundary or are LHR reflected into the magnetosphere.

Makita [1979] suggested that at the duct end near $\sim$ 3000 km, AH exits with all possible wave-normal angles, some with appropriate wave-normal angles such that the waves will reach the ground. In this thesis, duct merging with the background for various scale factors was considered to investigate propagation of AH as it exits from the duct (Figure 2.5.2). The typical scale heights with which ducts merge with the background are $\sim$ 800 km (daytime) to $\sim$ 1800 km (nighttime) [*Bernhardt and Park*, 1977]. In all the calculations, using the ray-tracing program that allows one to define duct parameters, duct merging scale heights as small as $\sim$ 30 km, roughly the width of the duct at 3000 km, gave similar results to those shown in Figure 2.5.2 for 800 km duct merging scale height. The AH wave-normal angle continues to increase toward θ_R as it exits

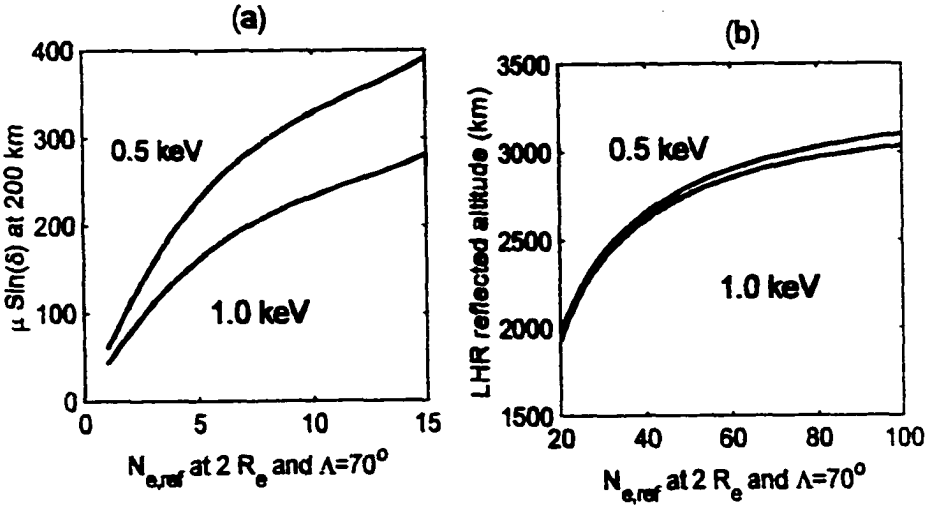

Figure 2.5.1. Reflection of 10 kHz nonducted (CAH) waves injected at 10,000 km altitude with initial wave-normal angles consistent with the generation of hiss by 0.5 and 1 keV energetic electrons. (a) Low reference density (1-15 el cm^{-3}): Waves propagate to lower altitudes ($\sim$ 200 km) and are totally internally reflected because $\mu sin(\delta) \gg 1$ where δ is the wave-normal angle relative to the vertical direction. (b) High reference density (20-100 el cm^{-3}): Waves are LHR reflected at higher altitudes.

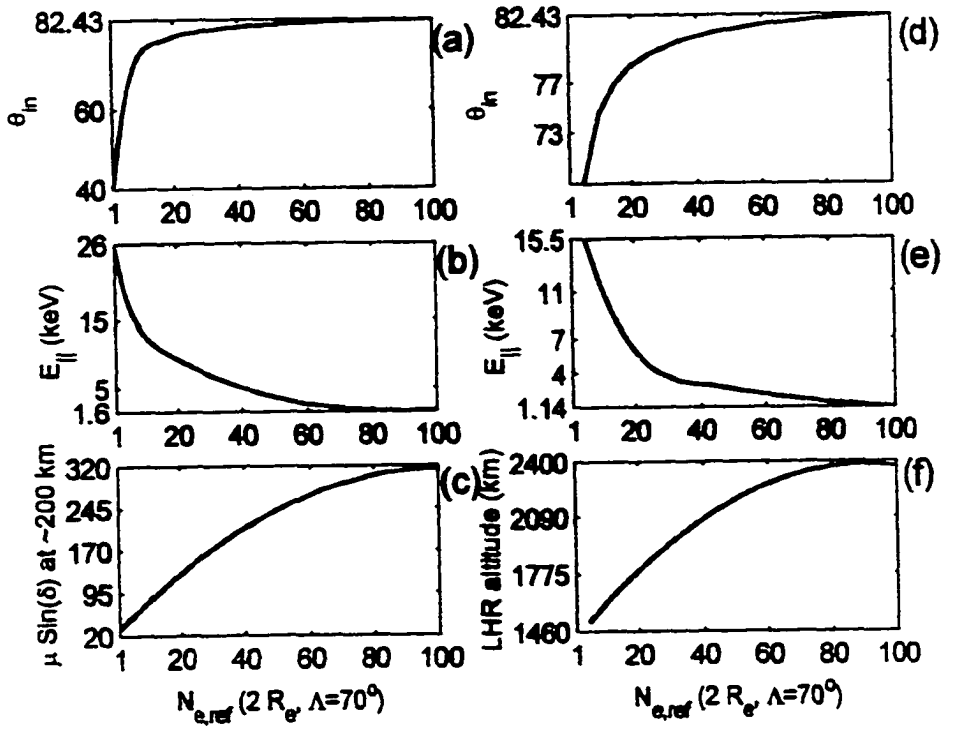

Figure 2.5.2 Reflection of 10 kHz ducted (IAH) waves injected at 10,000 km altitude. (a) The largest wave-normal angle (θ_{in}) at which the wave can be trapped as a function of density. (b) Parallel resonant energy $E_{||}$ of the trapped waves. (c) Value of $\mu(\theta)\sin(\delta) \gg 1$ at a low altitude ($\sim$ 200 km); for values much greater than 1, the ray will be totally internally reflected. (d) Value of (θ_{in}) at which LHR reflection is observed as a function of density. (e) $E_{||}$ as a function of density for the θ_{in} in Figure 2.5.2d. (f) The different altitudes at which LHR reflection is observed as a function of density.

the duct, keeping $\mu(\theta)\sin(\delta) \gg 1$. Therefore *Makita*'s [1979] assumption that waves exit the duct at all possible wave-normal angles is not justified, and his suggestion that a fraction of these waves fall in the transmission cone is not realizable.

Recently, *Matsuo et al.* [1998] proposed that large-scale irregularities ($\sim$ 10 – 100 km) can bend the AH wave-normal angles sufficiently to fall in the transmission cone. To prove their theory, a 5 kHz wave was injected at $\sim$ 5000 km altitude with an initial wave-normal angle 10° away from the resonance cone angle. The resonant energy of the electrons to generate AH in this case was $\sim$ 150 keV, which is very high compared to the $<$ 10 keV electrons associated with the generation of AH. Large-scale (10 km scale lengths) horizontal gradients present in the ionosphere can tilt the wave-normal angles of a whistler mode wave [*James*, 1972; *Singh and Singh*, 1978], but such tilts are small, about 5° – 20° [*James*, 1972; *Sonwalkar et al.*, 1984]. In general, large-scale irregularities cannot convert, by refraction, AH with large wave-normal angles into AH with sufficiently small wave-normal angles to penetrate to ground level.

The above results imply that an additional mechanism is required at altitudes of a few thousand kilometers which can convert the whistler mode waves with large θ into whistler mode waves with small θ that can propagate across the Earth-ionosphere boundary. One such mechanism is discussed below in section 2.6.

2.6 Scattering of Large Wave-Normal Angle Whistler Mode Waves Into Small Wave-Normal Angle Whistler Mode Waves

Both IAH (via a ducted mode) and CAH (via a nonducted mode) reach an altitude of a few thousand kilometers with large θ. From these altitudes, it is proposed, in this thesis, that IAH and CAH waves reach the ground via meter-scale irregularities, present up to a few thousand kilometers [*Fejer and Kelley*, 1980, and references therein; *Sonwalkar*, 1995], that convert large-θ whistler mode waves into whistler mode waves with θ small enough to penetrate to the ground (Figure 2.6.1). One mechanism by which the wave-normal angles of VLF waves

can be modified is the passive linear scattering mechanism provided by *Bell and Ngo* [1988, 1990].

Figure 2.6.1, adapted from *Bell and Ngo* [1990], is a geometric description of how an incident large wave-normal angle AH excites an electromagnetic low wave-normal angle whistler mode wave and an electrostatic large wave-normal angle whistler mode wave. Briefly, low wave-normal whistler mode waves and electrostatic waves are generated at the boundaries of the irregularity as a consequence of matching boundary conditions in a cold magnetoplasma. Chapter 3 discusses the passive linear mode conversion program developed by *Ngo* [1989] that is used in this thesis as the additional mechanism to bring waves with large θ to the ground. In the following sections the results obtained by using the program are discussed while the program itself is discussed in chapter 3.

In Figure 2.6.1, "INC AH" is the incident electrostatic wave or the whistler wave with θ that is propagating from high source altitudes to the ground. "REFL ES" and "TRANS AH" are quasi-electrostatic waves that are generated at the boundaries of the irregularity as a consequence of matching boundary conditions in a cold magnetoplasma. "TRANS WM" is also generated at the boundary of the irregularity, and is the electromagnetic wave with a small θ that will eventually fall in the transmission cone.

Figure 2.6.2 shows that meter-scale irregularities with relative densities ΔN_e from 10% to 50% can convert 0.1% to 10% of AH with large θ to low-θ ($<\sim 10°$) whistler mode waves that can penetrate to the ground. The dashed lines in the Figure represent irregularities that have a Gaussian density distribution, while the solid lines represent irregularities that have a rectangular density distribution. The solid line with the inverted triangles represents an irregularity that is a sharp boundary. For the low ($N_{e,ref}$ = 10 el cm^{-3}) and high ($N_{e,ref}$ = 50 el cm^{-3}) density models the transmitted power initially increases as the width of the irregularity increases. The width of the irregularity is shown in terms of λ, which is $\sim$ 1.75 m for $N_{e,ref}$ = 10 el cm^{-3} and $\sim$ 1 m for $N_{e,ref}$ = 50 el cm^{-3}. When the width of the irregularity is increased to values greater than $\sim 10\lambda$ for $N_{e,ref}$ = 50 el cm^{-3} and $\sim 100\lambda$ for $N_{e,ref}$ = 10 el cm^{-3}, the transmitted power decreases. Though not shown in Figures 2.6.2a and 2.6.2b, the transmitted power values for irregularity widths up to $\sim 200\lambda$ for both reference densities was

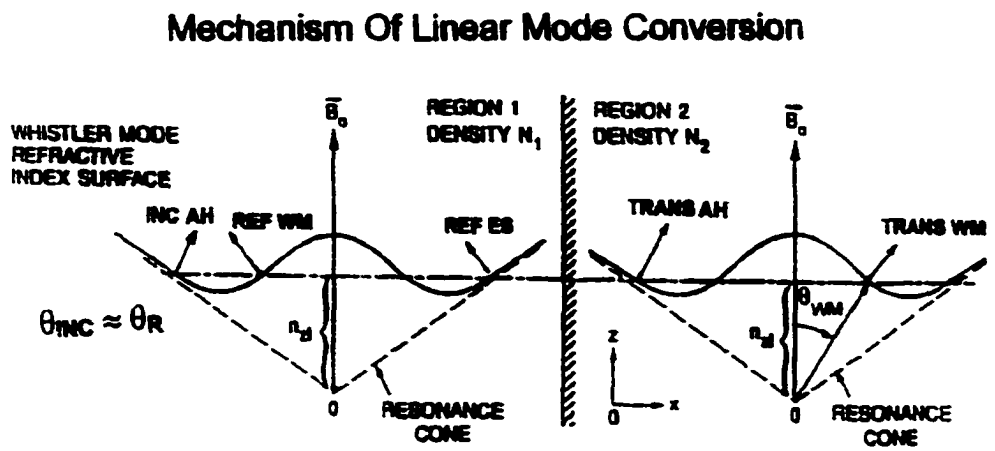

Figure 2.6.1. A geometric description of linear mode conversion of whistler mode waves. An incident large wave-normal ($\theta \sim \theta_R$) whistler mode wave (INC AH) is converted to a low wave-normal whistler mode transmitted wave (TRANS WM) and a reflected wave (REF WM), and a quasi-electrostatic reflected wave with a large wave-normal angle (REF ES) and a transmitted (TRANS AH) electrostatic wave (adapted from *Ngo* [1989] and *Bell and Ngo* [1988, 1990]).

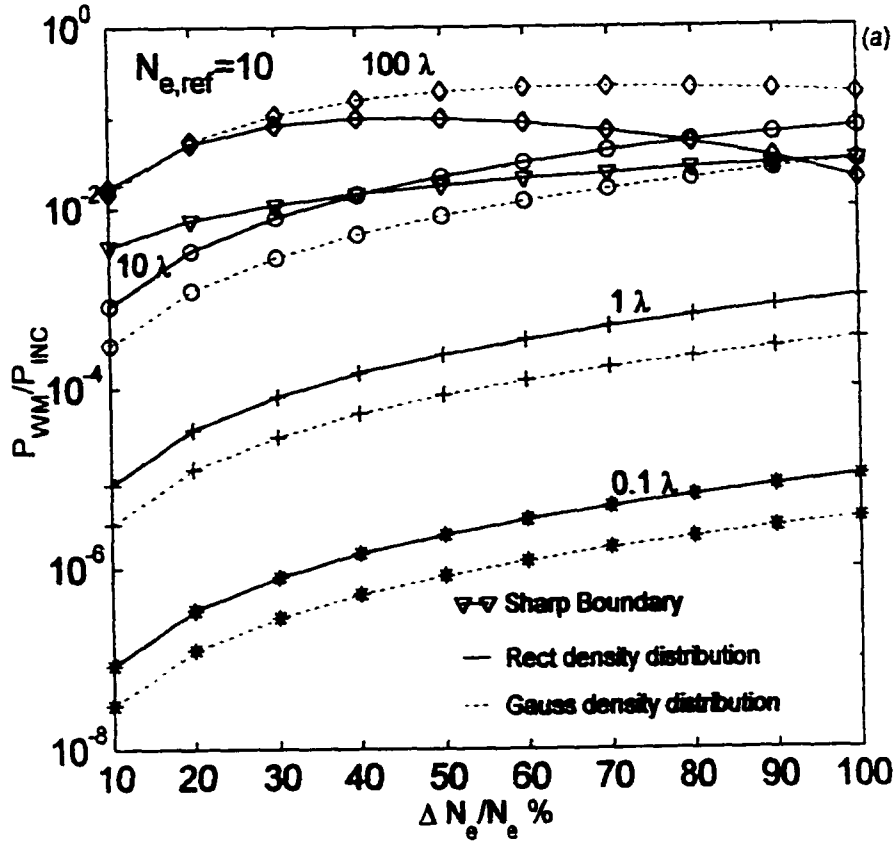

Figure 2.6.2a. Low wave-normal $\sim 10°$ whistler mode generation by linear mode conversion of large-θ whistler mode electrostatic wave for $N_{e,ref} = 10$ el cm^{-3}. Ratio of the transmitted whistler mode wave power to incident whistler mode wave power (P_{WM}/P_{INC}) is plotted as a function of fractional density enhancement in the irregularity. The width of the irregularity is defined in terms of the wavelength λ of the incident wave. The plots marked with inverted triangles represent a sharp boundary irregularity. The asterisks, pluses, open circles, and diamonds represent irregularities that are 0.1, 1, 10, and 100 λ wide respectively. The dashed lines represent a Gaussian density distribution while the solid lines, except the solid line with the inverted triangles, represent a rectangular (Rect) density distribution.

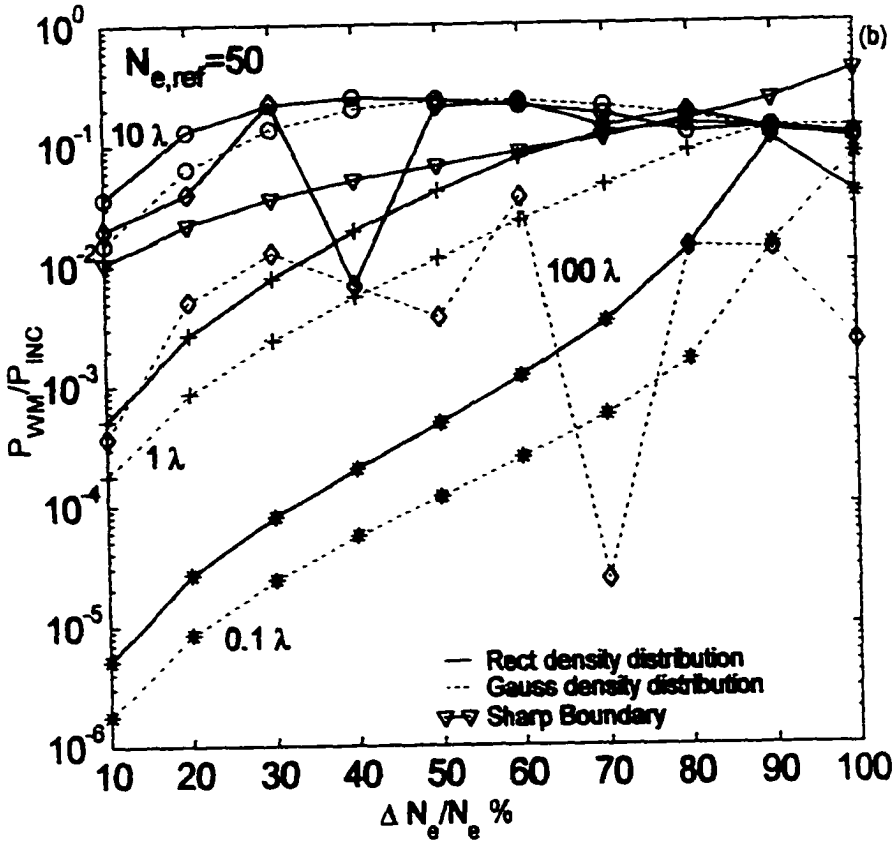

Figure 2.6.2.b. Low wave-normal ~ 10° whistler mode generation by linear mode conversion of large-θ whistler mode electrostatic wave for $N_{e,ref} = 50$ el cm^{-3}. Ratio of the transmitted whistler mode wave power to incident whistler mode wave power (P_{WM}/P_{INC}) is plotted as a function of fractional density enhancement in the irregularity. The width of the irregularity is defined in terms of the wavelength λ of the incident wave. The plots marked with inverted triangles represent a sharp boundary irregularity. The asterisks, pluses, open circles, and diamonds represent irregularities that are 0.1, 1, 10, and 100 λ wide respectively. The dashed lines represent a Gaussian density distribution while the solid lines, except the solid line with the inverted triangles, represent a rectangular (Rect) density distribution.

computed. When the density distribution in the irregularity is constant, as in the rectangular case, the transmitted power is larger than for a Gaussian distribution. The transmitted power shown in Figure 2.6.2 is computed for a whistler mode transmitted wave with $\theta \sim 10°$. In general, for all three distributions (rectangular, Gaussian, and sharp boundary) the peak transmitted power occurs for density enhancements > 30%.

IAH and CAH also suffer losses because of the D region absorption phenomenon. The absorption values through a range of 60 to 1500 km at 2 and 20 kHz for a geomagnetic latitude of 70° are ~ 1.2 and ~ 3 dB, respectively, for a nighttime ionosphere and ~ 8 and ~ 20 dB for a daytime ionosphere [*Helliwell*, 1965]. CAH additionally suffers transmission losses in the Earth-ionosphere waveguide depending on its exit point. *Tsuruda et al.* [1982] have measured a typical rate of attenuation with distance to be as high as -7 dB per 100 km, and *Walker* [1974] estimated an attenuation rate of -12 dB per 1000 km. IAH is observed overhead and will not suffer transmission losses in the Earth-ionosphere waveguide. The power spectral density ratios computed above for conversion of large wave-normal angle whistler mode waves to small wave-normal angle whistler mode waves are consistent with the power spectral density ratio of ground and satellite AH of 10^{-5} to 10^{-2}, accounting for 10 dB losses for the ionospheric absorption, reflection at the boundary, and spreading in the waveguide [*Helliwell*, 1965; *Srivastava*, 1974].

The f_{LHR} at the highest altitude up to which meter-scale irregularities exist determines the lower frequency cutoff for both IAH and CAH. Frequencies that have a f_{LHR} above this altitude will be reflected into the magnetosphere before reaching the meter-scale irregularities. Since the meter-scale irregularities extend up to a few thousand kilometers [*Fejer and Kelley*, 1980; *Sonwalkar*, 1995]. Figure 2.2.2 implies a low cutoff frequency of AH at a few kiloHertz, consistent with observations. The role of meter-scale irregularities in converting large wave-normal angle whistlers to small wave-normal angle whistlers is supported by a strong association found between the occurrence of auroral hiss and 18 MHz radar echoes from F region field-aligned irregularities ($\lambda \sim 16.7$ m) [*Hower and Gluth*, 1965]. In this study, out of 33 hiss events observed, 32 were associated with 18 MHz radar returns, indicative of ~ 10 m scale field-aligned irregularities.

Other mechanisms to convert small-θ whistler mode waves to large-θ whistler mode waves have been proposed by *Titova et al.* [1984] and *Groves et al.* [1988]. *Groves et al.* [1988] have suggested a nonlinear scattering mechanism of VLF signals by ionospheric density fluctuations with scale lengths of several tens of meters to scatter VLF waves to produce electrostatic modes with large wave vectors. *Titova et al.* [1984] have proposed that ion acoustic or ion cyclotron waves cause small-scale ionospheric irregularities that transform small-θ whistlers to large-θ whistlers by resonant scattering of VLF waves. It is possible that some of these other mechanisms may be able to convert large-θ whistler mode waves to small-θ whistler mode waves and could also be operative alongside the passive linear scattering mode discussed in this paper.

2.7 Wave Transmission at the Earth-Ionosphere Boundary

The Earth-ionosphere boundary is an abrupt boundary at VLF frequencies. Whistler mode waves have a refractive index $\mu \geq 10 - 20$ on the ionosphere side and unity on the Earth side. By Snell's law only those ionospheric waves that satisfy $\mu(\theta) \sin\delta < 1$ can penetrate to the ground. This gives $\delta \sim 3° - 6°$. The geomagnetic field, with a tilt toward the equator, makes an angle of $\sim 10°$ with the local vertical at invariant latitude $\Lambda = 70°$. Thus wave-normal angles $\theta \leq 13° - 16°$, tilted toward the equator, can penetrate to the ground. The wave-normal angles of $\theta \sim 5° - 10°$ of whistler mode waves, generated by the scattering of downcoming AH by meter-scale irregularities, fall into this range and will thus penetrate to the ground. The wave-normal angles tilted away from the equator cannot penetrate to the ground (Figure 2.7.1). This propagation restriction explains why CAH is observed equatorward of the visible aurora. In Figure 2.5.1, for reference densities between 1 and 15 el cm^{-3} CAH generated by 0.5 and 1 keV electrons propagates to low altitudes ($\sim$ 200 km). From ray-tracing calculations it was found that for a 10 kHz CAH wave generated by 0.5 keV energy electrons and propagating from 10,000 km altitude to $\sim$ 200 km, the exit point was $\sim$ 1310 km away from the original field line ($L = 8.55$). For CAH generated by 1 keV electrons, the exit point was $\sim$ 1290 km away from the original field line ($L = 8.55$).

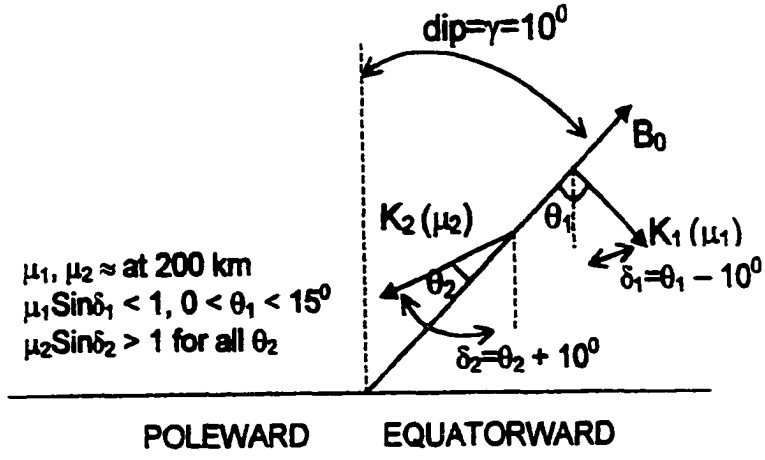

Figure 2.7.1. Schematic illustrating that whistler mode waves propagating with wave-normal angle $\theta < 15°$ equatorward will be transmitted to the ground. Wave-normal angles tilted away from the equator will not propagate to the ground.

The numbers provided are for a low-reference-density model, $N_{e,ref} = 1$ el cm^{-3}. As the reference density increases, the waves come closer to the field line at lower altitudes, and for $N_{e,ref} = 15$ el cm^{-3} the wave was ~ 280 km away.

3. Geomagnetic Field Model. Cold Plasma Density Model and Linear Mode Conversion Model

In this chapter. the software programs and the models used to determine the ray path and convert the large θ AH to small θ AH are discussed. These programs will be used in chapter 4 to determine the density concentrations along auroral field lines. energetic electron energy. and source region of AH. from the AH spectra using the mechanism proposed in chapter 2. Two software programs are used to invert (or make inferences from observed data) the AH spectra data: (1) the "ray-tracing" [*Burtis*. 1974] program. and (2) the "linear mode conversion" [*Ngo*. 1989] program. The ray-tracing program was initially developed in 1974 and designed predominantly to determine ray path and other plasma parameters for whistlers propagating at low altitudes and low latitudes. To ensure that the ray-tracing program can be used to give correct results for AH propagating from high latitudes and high altitudes to the ground. the different models that make up the program are analyzed in the sections 3.1 and 3.2. The 2-D ray-tracing [*Burtis*. 1974] program. evaluates a system of 5 differential equations: the 4 *Haselgrove* [1964] equations and an equation to compute the variation of group delay and check the accuracy of the code [*Yabroff*. 1961: *Kimura*. 1966]. A 3-D ray-tracing program was not used because AH is along the field line or in the magnetic meridional plane and rays injected in the magnetic meridional plane spread little in longitude [*Sonwalkar et al.*. 1994]. The 2-D ray-tracing program uses a dipole field model to model the Earth's magnetic field. a diffusive equilibrium model to calculate the cold plasma density within the plasmasphere and a collisionless model (R^{-n}) to calculate the density outside the plasmasphere [*Inan and Bell*. 1977]. In section 3.1 it is determined if a dipole field model can reasonably represent the Earth's magnetic field at the AH source altitudes and latitudes so that it can be used in this thesis. In section 3.2 the diffusive equilibrium density model and the R^{-n} collisionless density model are analyzed to determine how the user input parameters need to be modified and adapted to represent the magnetospheric density determined by past satellite and ground observations.

In chapter 2 it was proposed that AH reaches the ground by scattering. on meter-scale irregularities. into whistler waves with small θ that can penetrate

to the ground. The scattering mechanism involves recomputing the angles and amplitudes of the incident, reflected and transmitted waves. The equations used to determine the angles and the amplitudes of the waves incident on a boundary are programmed in the linear mode conversion program [*Ngo*, 1989]. For this thesis, the "linear mode conversion" [*Ngo*, 1989] program is adapted and used to calculate the amplitudes of the electrostatic and electromagnetic waves that are the results of an input whistler wave scattering from a plasma density irregularity. Meter-scale irregularities can be modeled as a sharp boundary or a slab with a a rectangular or gaussian density distribution. In section 3.3, the passive linear scattering mechanism of the linear mode conversion program [*Ngo*, 1989] is discussed and the different plasma irregularity density distributions are considered.

3.1 Geomagnetic Field Model

The solar wind interacts with the Earth's magnetic field and distorts it. Close to the Earth's surface, the geomagnetic field can be represented by a dipole field model. For a dipole field, the magnetic flux density is given by

$$B(r,\lambda) = \frac{M}{r^3}(1+3\sin^2\lambda)^{\frac{1}{2}} \tag{3.1.1}$$

where M is the dipole moment, r is the geocentric radial distance and λ is the geomagnetic latitude. The geomagnetic field components in the r and λ directions are

$$B_r = -\frac{2M\sin\lambda}{r^3}. \tag{3.1.2a}$$

$$B_\lambda = \frac{M\cos\lambda}{r^3} \tag{3.1.2b}$$

The dipole field is symmetric about its axis so that $B_\phi = 0$. The dipole field approximation of the Earth's geomagnetic field is fairly accurate for geocentric

distances between 3 and 4 R_E where R_E is the radius (6370 km) of the Earth. The equation of a dipolar field line is derived from the geomagnetic field components as shown in the following equations

$$\frac{B_\lambda}{B_r} = \frac{r d\lambda}{dr} = \frac{-1}{2\tan\lambda} \tag{3.1.3}$$

Integrating the above equation with respect to r. the equation of a dipole field line is

$$r = r_0 \cos^2\lambda \tag{3.1.4}$$

For $\lambda = 0$ (along the equator). $r = r_0$ and it is the greatest distance of the field line from the Earth. Figure 3.1a is a schematic of a dipole field model. Figure 3.1b is a schematic of the actual field model. From Figures 3.1a and 3.1b. it is clearly seen that on the far side of the sun the Earth's magnetic field is distorted by the solar wind and the dipole field model is a poor representation of the actual magnetic field. To determine if a dipole model can reasonably represent the Earth's magnetic field at the AH source altitudes and latitudes. in Figure 3.1c the Earth's actual field is compared with the field calculated from the dipole model. In Figure 3.1c the magnetic field strength of a dipole field model is compared with an actual field model (IRI 95 for June 30. 1996 02 UT) for a L-shell value of 27.47 or invariant latitude $\Lambda = 79°$. [The actual field strength model result was obtained from the web pages of NASA's National Space Science Data Center. International Reference Ionosphere -IRI-95]. A L-shell value was selected that best represents the particular data set. From Figure 3.1c it is seen that the dipole field model is a good representation of the actual field model for the data set. Data was collected from South Pole (SP). $\lambda_g = 90°$ between May and July1996 [*Courtesy Stanford University*].

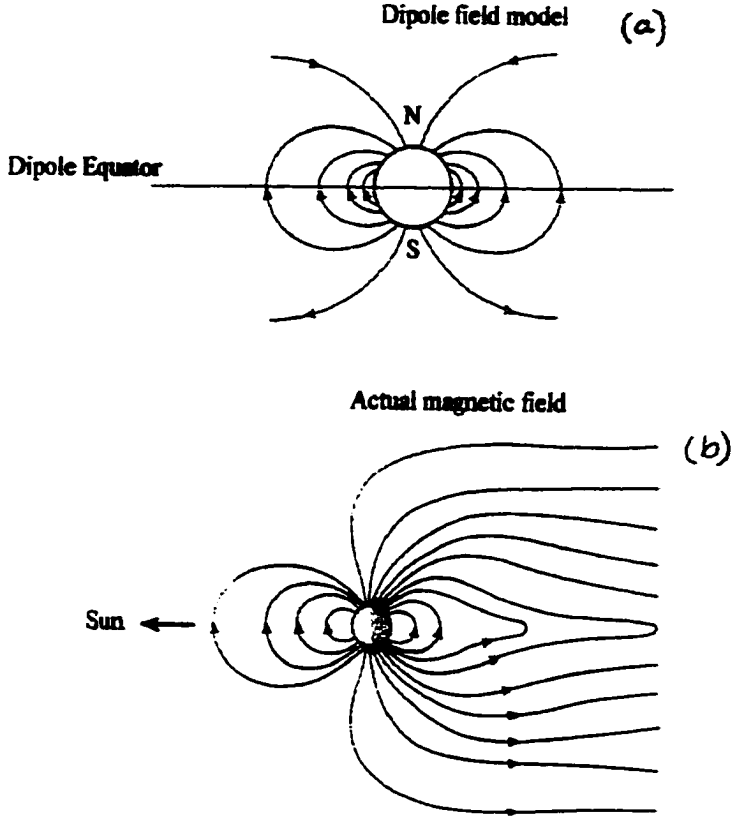

Figure 3.1.1. (a) Schematic of a dipole field model. (b) Schematic of the Earth's actual magnetic field.

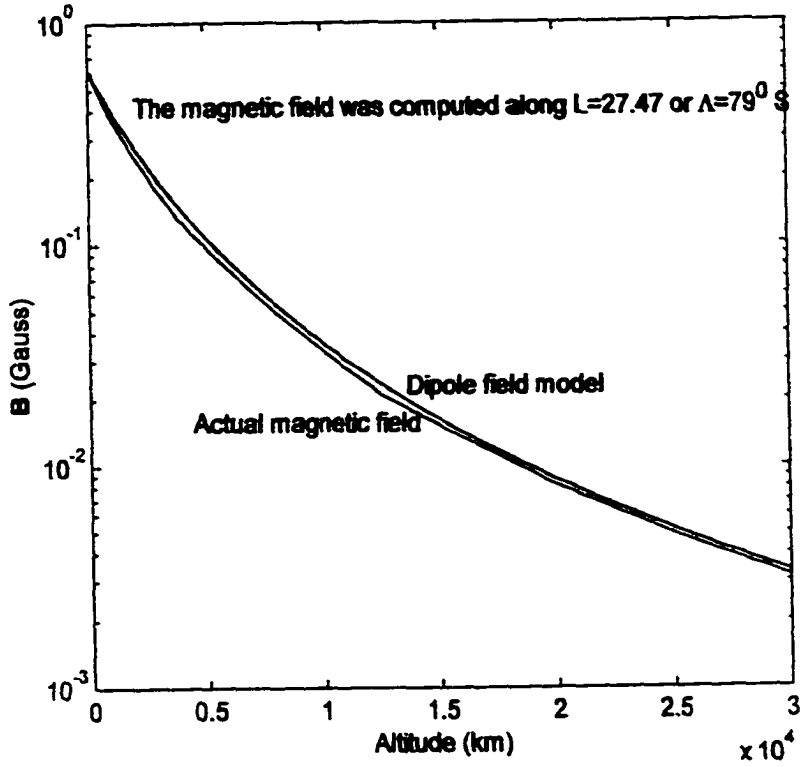

Figure 3.1.1c. The Earth's magnetic field as a function of altitude computed along L=27.47 or $\Lambda = 79°$ S. The graph shows that the magnetic field values computed using a dipole field model matches the actual magnetic field values [*IRI 95*, June 30, 1996, 02 UT].

3.2 Cold Plasma Density Model

The ray-tracing model uses a diffusive equilibrium model for density within the plasmasphere and a collisionless model (R^n) outside the plasmasphere. In the following paragraphs, the different parameters of the density model and the ray-tracing model input parameters are discussed.

The electron density is a product of five factors: electron density ANE0 at the base of the diffusive equilibrium model, diffusive equilibrium (ANR), lower ionosphere (ANLI), plasmapause (ANLK), and ducts (ANL).

ANE0: The electron density at the base of the diffusive equilibrium model is calculated from the reference density ($N_{e,ref}$) specified at a certain altitude and geomagnetic latitude. In this thesis, $N_{e,ref}$ is varied between 1 and 100 el cm^{-3} at 2 R_E altitude and 79° invariant latitude. The electron density generally decreases with radial distance, beyond the F2 peak.

ANR: The factor due to diffusive equilibrium [*Angerami and Thomas*, 1964] is

$$ANR(r) = [\sum_{I=2,NUM} ALPHA0(I)\epsilon^{-GPH/SH(I)}]^{1/2} \qquad (3.2.1)$$

where

$$GPH = RBASE(1 - \frac{RBASE}{r}) \qquad (3.2.2)$$

$$SH(I) = 1.1506(THERM)(\frac{RBASE}{7370})^2\frac{1}{(4)^{I-2}} \qquad (3.2.3)$$

r is the radial distance

RBASE is the geocentric distance (km) to the base of the diffusive equilibrium model.

ALPHA0 is the relative concentration of H^+, H_e^+ and O^+ in the diffusive equilibrium model at RBASE.

THERM is the temperature used in the diffusive equilibrium model.

From the above equations it is clear that density factor due to diffusive equilibrium depends on RBASE and THERM. Figure 3.2.1 shows the ANR dependence on RBASE and THERM. For Figure 3.2.1 a reference density of 1 el cm^{-3} was defined at an altitude of 2 R_E and $\Lambda = 79°$. The ion concentrations are a function of RBASE and THERM. At $r = RBASE.GPH = 0$ and the density $ANR = 1$. For a given RBASE and THERM. ANR is a decreasing exponential function. As RBASE increases ANR increases whereas ANR decreases as THERM increases.

ANLI: The factor due to the lower ionosphere is

$$ANLI(r) = 1 - \epsilon^{-(\frac{r-RZERO}{SCBOT})^2} \tag{3.2.4}$$

where

r is the radial distance.

RZERO is the geocentric distance (km) to the level at the bottom of the lower ionosphere ($\sim$ 6450 – 6470 km) where the density goes to zero [*Carpenter and Park*, 1973]. RZERO for the model used in this thesis is 6460 km. i.e., it is assumed that the bottom of the ionosphere is at an altitude of 90 (6460-R_E) km. SCBOT is the scale height (km) of the bottomside of the lower ionosphere. The ionospheric region of the Earth's atmosphere extends between 80 and 1000 km. There are several different ionospheric layers. The main ones are the E-layer at $\sim$ 100 km and the F-layer at $\sim$ 300 km with an ion and electron concentration of about $10^5 - 10^6$ el cm^{-3}. Scale height is the height the ray must descend to see a fall in density of 1/e from its reference value. From *Davies* [1969], if ρ_o is the reference density value at reference height h_o then density ρ at height h is given by:

$$\rho = \rho_o \epsilon^{-(h-h_o)/H} \tag{3.2.5}$$

where H is the scale height.

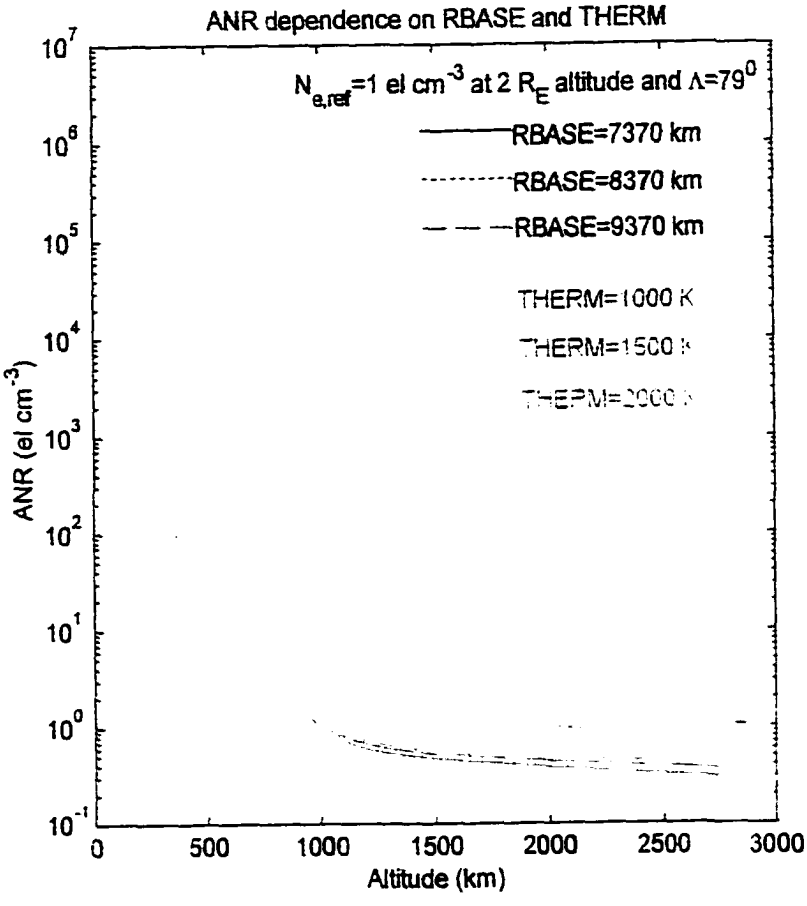

Figure 3.2.1. Density factor from the diffusive equilibrium model as a function of altitude for different temperatures and diffusive equilibrium models. Density within the plasmasphere is determined by the diffusive equilibrium model. RBASE is the geocentric distance to the base of the diffusive equilibrium model and at altitudes greater than RBASE, there is no density contribution from the diffusive equilibrium model. THERM is the temperature used in the diffusive equilibrium model and as temperature increases the density decreases. RBASE and THERM play an important role in the fall in density from the F2 peak.

The electron density as a function of ionospheric altitude varies as follows:

Table 1: Electron Density for Different Ionospheric Altitudes (SP 6/30/96. 02 UT)

Altitude (km)	Density (el cm^{-3})
100	1685
200	2626
300	82937
400	56279
500	25589
600	12589
700	7882
800	6045
900	5260
1000	4905

[*The model result was obtained from the web pages of NASA's National Space Science Data Center. International Reference Ionosphere - IRI-95*]. From Table 1. the median SCBOT for the ionosphere is $\approx 120 - 140$ km. At $r = RZERO$. density is 0. For $r > RZERO$. ANLI is an increasing exponential function. SCBOT determines the rate at which ANLI increases as r increases. Figure 3.2.2 shows the ANLI dependence on SCBOT.

Density at different altitudes below RBASE is a product of ANR and ANLI density factors and SCBOT plays an important role in determining the F2 peak. Figure 3.2.3 is the density observed due to different ANR and ANLI terms as a function of altitude for $\Lambda = 79°$ or $L = 27.47$. At different RBASE heights the electron concentration and ion composition vary. Hence. Figure 3.2.3 indirectly also includes the effect of the ANE0 term in its plots. The ion composition used to graph the subplots in Figure 3.2.3 are as shown in Table 2.

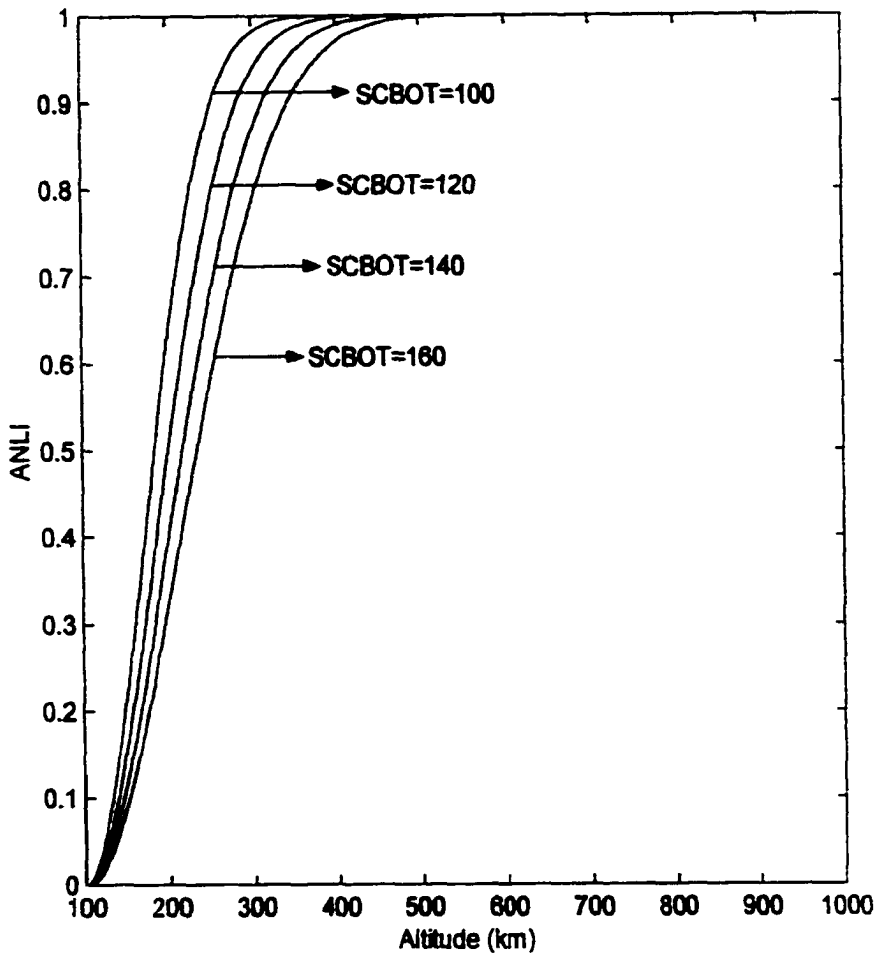

Figure 3.2.2. Density due to the lower ionospheric factor as a function of altitude for different scale heights. Density in the ionosphere peaks at $\sim$ 300 km. ANLI is a number that adjusts the density to show the influence of the lower ionosphere. At altitudes greater than 300 km the density decreases. SCBOT is the height the ray must descend to see a $1/e$ fall in density from its reference value.

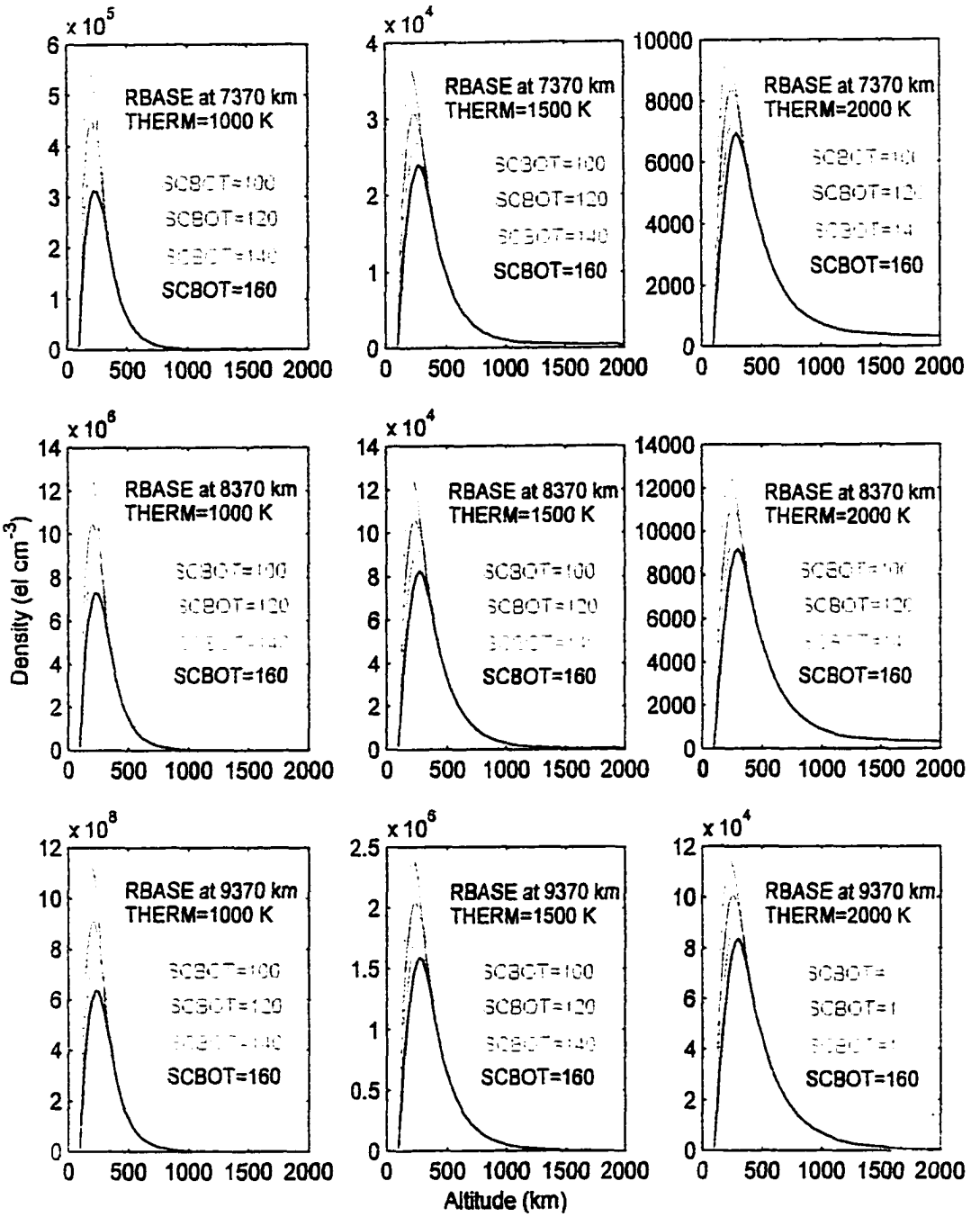

Figure 3.2.3. Density due to the diffusive equilibrium model and the lower ionosphere as a function of altitude for different diffusive equilibrium models, temperatures and scale heights. Density factor due to diffusive equilibrium is ANR while ANLI is the density factor due to the lower ionosphere. ANR and ANLI together determine the fall in density from the F2 peak as the altitude increases. $N_{e\_ref} = 1$ el cm^{-3} at 2 R_E altitude and $\Lambda = 79°$ for this figure.

Table 2: Ion Composition for Different Altitudes

Altitude (km)	$N(H^+)/N$	$N(H_e^+)/N$	$N(O^+)/N$
1000	0.3	0.1	0.6
2000	0.89	0.01	0.1
3000	0.98	0.01	0.01

ANLK: The factor due to the plasmapause is

$$ANLK(r, L) = e^{-ARGL} + (1 - e^{ARGL})[TRM + (1 - TRM)e^{-(ARGR)^2}] \quad (3.2.6)$$

where

$$ARGL = \frac{(L - LK)^2}{(DDK)^2} \quad (3.2.7)$$

$$ARGR = \frac{r - RCONSN}{SCR} \quad (3.2.8)$$

$$TRM = (\frac{RCONSN}{r})^{EXPK} \quad (3.2.9)$$

r is the radial distance L is the L-shell value
LK is the L-value of the inner edge of the plasmapause or "knee". The plasmapause can be observed between L=3 ($\Lambda = 54.7°$) and L=7 ($\Lambda = 67.8°$) [*Carpenter and Park*, 1973]. The plasmapause L value in the post midnight period can be computed as a function of magnetic disturbance (k_p) using the formula

$$L_{plasmapause} = 5.7 - 0.47K_p \quad (3.2.10)$$

where K_p is the maximum 3-hour K_p value in the preceding 12 hours [*Carpenter and Park*, 1973]. A plasmapause at $L = 4$, a location generally found on relatively quiet days, was selected for this thesis. Since the auroral magnetosphere

typically lies outside the plasmasphere. the exact location of the plasmapause is not important for the density model calculations in this thesis.

DDK is the half-width (in L) of the knee. The center or steepest gradient of the knee is at LK+DDK. The duct width at the equator for a L-shell value of 4 varies between 223 km and 1260 km [*Angerami.* 1970. *Carpenter et al.*. 1981. and *Koons et al.*. 1989]. A half-width of 0.1L (637 km at the equator) for the knee half-width was selected for this thesis.

RCONSN is the geocentric distance (km) to the level at which the density outside the knee is equal to the density inside the knee. It defines the plasmapause termination altitude in kilometers from the Earth center. The inner edge of the plasmasphere is taken as the altitude at which protons replace oxygen as the dominant species in the ionospheric plasma and it usually occurs at ~600 to 1000 km altitude. At $r = RCONSN$. $ARGR = 0$. $TRM = 1$ and density due to the plasmapause factor (ANLK) is 1. The RCONSN value specified for the ray-tracings in this thesis is 7000 km.

SCR is the scale height of the radial density decrease above RCONSN outside the knee. At the plasmapause. equatorial electron density decreases with distance by a factor of 10-100 [*Carpenter.* 1995. *Park and Carpenter.* 1978]. A density decrease by factor of 100 gives a scale height of $\approx$ 3000 km. SCR is equal to 3000 km for the ray-tracing model used in this thesis.

EXPK determines the exponential component of density decrease beyond the knee. In essence. EXPK determines the collisionless model (R^{-n}) that is used outside the plasmasphere. where EXPK represents the n in R^{-n}. A density variation of ($R^{-4.5}$) to ($R^{-5.5}$) outside the plasmasphere is defined in this thesis so that the density values conform to the entire range of experimental density measurements by [*Persoon et al.*. 1983: *Persoon.* 1988: *Persoon et al.*. 1988]. *Persoon et al.* [1983] suggest exponent values for R between -3.53 and -4.17 for L values greater than 10 or invariant latitudes greater than 71.6°. *Persoon* [1988] expanded the data set of Persoon et al. [1983] over a higher altitude range with more data from lower altitudes and redefined the exponent values for R to -4.92 through -5.76 for invariant latitudes greater than 70^0.

ANLK is a function of both. the radial distance and the L-shell. ANLK is 1 for $L < LK$ and is a rapidly decreasing exponential function for $L > LK$. Since

the auroral magnetosphere typically lies outside $\Lambda = 70°$ or $L \geq 8.55$ the density factor due to ANLK as a function of L plays a very small role.

The electron and ion composition of the Earth's ionosphere is highly variable. In this thesis two sets of density models are used to represent the electron density between the surface of the EARTH and 20.000 km altitude. One set of density models represent the density observed in the magnetosphere between $\sim 3000 - 5000$ km and 20.000 km altitude. Figure 3.2.4 compares the density models of the magnetosphere used in this thesis with experimental results [*Persoon et al.*. 1983: *Persoon et al.*. 1988: *Persoon* 1988: *Kletzing et al.*. 1998]. and theoretical models of the auroral region plasma density [*Maggs and Lotko*. 1981: *Gurnett* 1978: *Jorgensen* 1968]. Figure 3.2.4 shows density values from 100 km altitude to 20.000 km altitude. however. the models shown in the figure will be used from $\sim 3000 - 5000$ km to 20.000 km altitude. The entire range of altitudes is shown in order to illustrate the complete density value range of *Gurnett* [1978]. *Jorgensen* [1968]. *Kletzing et al.*. [1998]. and *Maggs and Lotko* [1981]. The input parameters for the models in Figure 3.2.4 are as given in Table 3.

Table 3: Input Parameters for the Density Models Shown in Figure 3.2.4

RBASE (km)	THERM (°K)	SCBOT (km)
7370	2000	140

Figure 3.2.5 shows the second set of density models used in this thesis. The density models in Figure 3.2.5 model the Earth's atmosphere between 100 km and $\sim 3000 - 5000$ km. The electron density and ion composition in the Earth's ionosphere is highly variable and to optimally represent the ionosphere four density models were defined. The model parameters are as given in Table 4. The lowest density curve in Figures 3.2.4 and 3.2.5 show $f_{pe} \approx 500$ kHz or $N_e \approx 3000$ el cm^{-3} at 1400 km altitude. From *Benson and Grebowsky* [2001]. ISIS-2 N_e contours show $N_e < 3000$ el cm^{-3} for 1400 km altitude during 3 passes of ISIS-2 over the Canadian telemetry station in Resolute Bay. Thus there are ISIS-2 observations that yield density values lower than the minimum curve shown in Figures 3.2.4 and 3.2.5 for altitudes less than 1500 km. However in this thesis. downcoming $\vec{AH}$ is scattered by meter-scale irregularities present between

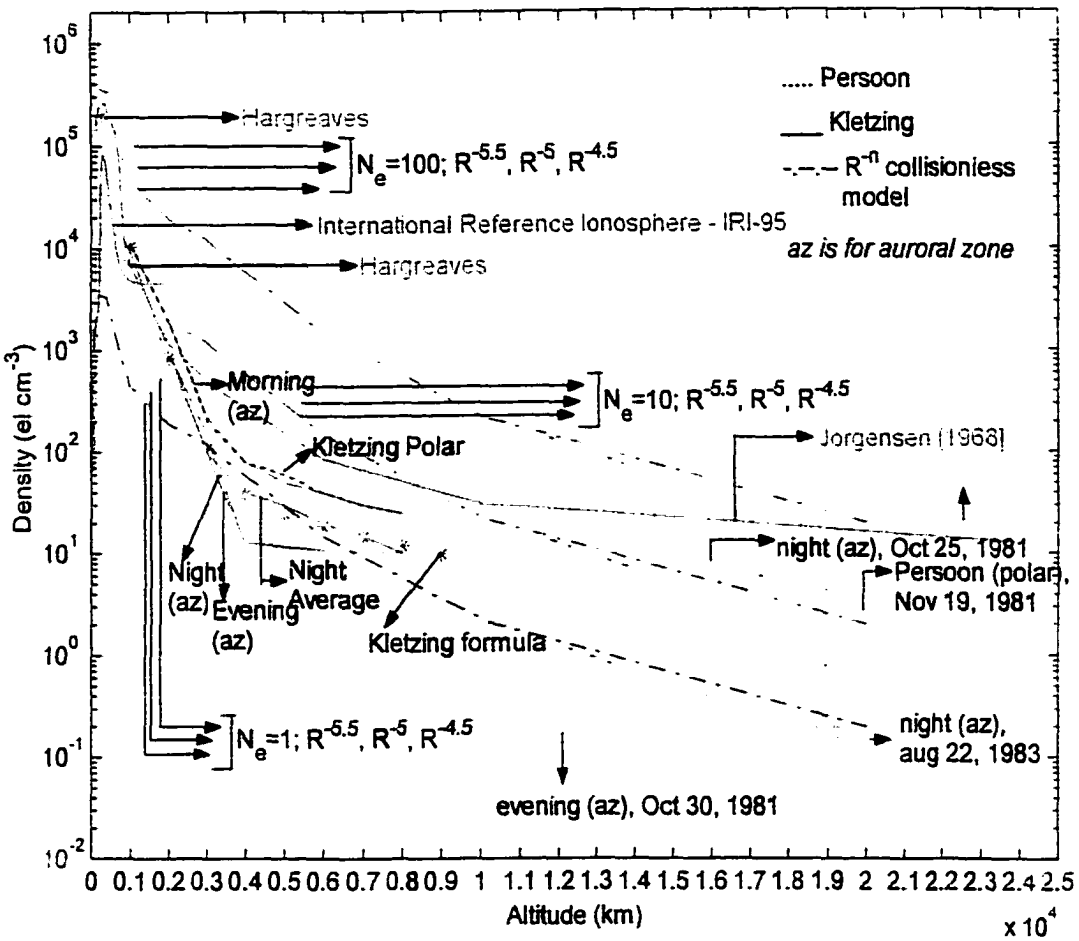

Figure 3.2.4. Comparison of collisionless R^{-n} models with density models from previous work. $N_{e,ref}$ =1, 10, 100 el cm^{-3} at 2 R_E altitude and $\Lambda = 79°$ for the different R^{-n} models. For completeness, the figure shows density as a function of altitude from 100 km to 25,000 km. The altitude region of interest in the figure, for this thesis, is between $\sim 3000 - 5000$ km and 20,000 km.

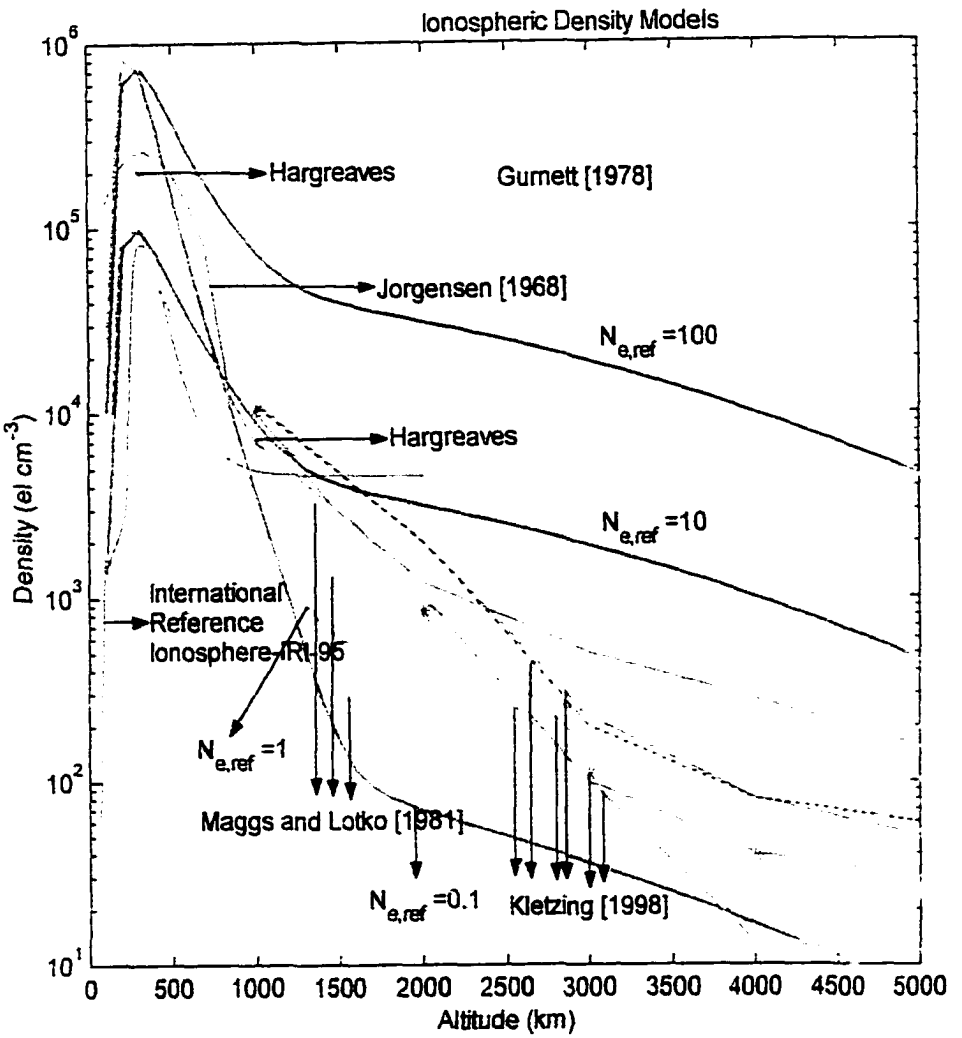

Figure 3.2.5. Comparison of the four density models, $N_{e,ref}$ =0.1, 1, 10, and 100 el cm^{-3} at 2 R_E altitude and $\Lambda = 79°$, used in this thesis for altitudes between 100 km and 5000 km with theoretical and observed density values in literature.

3000-5000 km altitude and hence a precise density model is not necessary for altitudes less than 3000 km altitude.

Table 4: Ionospheric Density Model Parameters

$N_{e,ref}$ at $2\ R_E$, $\Lambda = 79°$ (el cm^{-3})	RBASE (km)	THERM (°K)	SCBOT (km)	$\frac{N(H^+)}{N}$	$\frac{N(He^+)}{N}$	$\frac{N(O^+)}{N}$
0.1	8370	1000	140	0.89	0.1	0.01
1	8370	1500	120	0.89	0.1	0.01
10	8370	2000	140	0.89	0.1	0.01
100	7370	2000	140	0.3	0.1	0.6

ANL: The factor due to the Kth duct is

$$ANL(r, L) = 1 + DEF(K)e^{-1/2(\frac{L-L0(K)}{DD(K)})^2} . FRDUCT \qquad (3.2.11)$$

where

$$FRDUCT = \begin{cases} e^{\frac{[RDUCTL(K)-r]^2}{HL2(K)}} & \text{if r < RDUCTL} \\ 1 & \text{if RDUCTL < r < RDUCTU} \\ e^{\frac{[r-RDUCTU(K)]^2}{HU2(K)}} & \text{if r > RDUCTU} \end{cases} \qquad (3.2.12)$$

r: is the radial distance L is the L-shell value
L0(K) is the L-shell value of the center of the K^{th} duct.
DD(K) is the half width (in L) of the K^{th} duct
RDUCTL(K) is the geocentric distance (km) to the lower end of the K^{th} duct. Below RDUCTL the duct enhancement begins to merge into the background density.

HL2(K) is the square of HDUCTL(K). HDUCTL(K) is the radial scale height (km) with which the lower end of the K^{th} duct merges into the background density.
RDUCTU(K) is the geocentric distance (km) to the upper end of the K^{th} duct. Above RDUCTU the duct enhancement begins to merge into the background density.
HU2(K) is the square of HDUCTU(K). HDUCTU(K) is the radial scale height (km) with which the upper end of the K^{th} duct merges into the background density.

Duct end altitude and scale height with which the duct merges into the background density: During winter and equinoxes, VLF ducts extend down to 300 km altitude at night and terminate above 1800 km during the day, and in summer ducts terminate above 1000 km altitude at all local times (*Bernhardt and Parks* [1977]). A duct is said to have merged with the background density when the density in the duct is one tenth its value at 3000 km (*Bernhardt and Parks*, [1977]). From *Bernhardt and Parks* [1977], it can be calculated that if a 15% duct terminates at 3000 km altitude and merges into the background density at 1800 km then the duct has merged with the background density in 1200 km. This gives a scale merge height of ~800 km ($e^{-(1200/scaleheight)^2} = 0.1$). The data used to test the model was collected at South Pole between May and July 1996. Additionally, the data was collected between 2335 and 0235 UT. There is a 12 hour difference between UT and South Pole local time and South Pole experiences winter during the months of May, June and July. So for the examples in this thesis, the VLF ducts terminate around 1800 km with a scale height of 800 km.

Duct width and enhancement/depletion factors: To estimate the duct width, enhancements and depletions in the auroral zone, DE wideband analog data from *Persoon et al.* [1988] was used. In *Persoon et al.* [1988] the authors examine the electron density depletions which occur on nightside auroral field lines at geocentric radial distances of $2 - 4\ R_E$ at $70° \pm 5°$ invariant latitudes. Table 5 is a synopsis of the analysis of the graphs and data presented by *Persoon et al.* [1988].

Table 5: (Analysis of "clearly known" data presented in *Persoon et al.* [1988])

	8/22/83	10/25/81 (*)	10/30/81 (*)	11/19/81
Density (el cm^{-3})	0.01-2.2	2.25-8.5	1.75-7	1.91-5.6
Average Density	0.47	5.01	3.51	3.57
Number of density enhancements	62	23	32	22
Number of density depletions	58	20	25	29
Number of density no changes	3	16	13	13
Average value of density during enhancements	0.55	5.56	4.02	4.35
Average value of density during depletions	0.37	4.08	2.88	3.13
max depletion (%)	-96.7	-47.2	-61.1	-47.8
max enhance (%)	900	96	90	96.3
max L value	12.87	42.39	52.6	148.59
min L value	9.42	10.15	7.51	17.2
min (change in L) or ΔL_{min}	0.0003	0.0041	0.0002	0.6137
max (change in L)or ΔL_{max}	0.1152	4.56	5.74	6.31
Average ΔL for enhancement	0.027	0.38	0.45	1.84
Average ΔL for depletion	0.029	0.29	0.47	1.81

*This column does not include those density values in the analysis that *Persoon et al.* [1983] said "were not clearly known". Table 6 is the unmodified data set determined from the figures in *Persoon et al.*, [1988].

Table 6: (Analysis of all the data presented in *Persoon et al.* [1988])

	8/22/83	10/25/81	10/30/81	11/19/81
Density (el cm^{-3})	0.01-2.2	0.63-8.5	0.16-7	1.91-5.6
Average Density	0.47	4.44	3.1	3.57
Number of density enhancements	62	26	35	22
Number of density depletions	58	26	33	29
Number of density no changes	3	18	14	13
Average value of density during enhancements	0.55	4.95	3.78	4.35
Average value of density during depletions	0.37	3.37	2.31	3.13
max depletion (%)	-96.7	-52.7	-79.3	-47.8
max enhance (%)	900	96	115.4	96.3
max L value	12.87	42.39	52.6	148.59
min L value	9.42	6.86	5.64	17.2
min (change in L) or ΔL_{min}	0.0003	0.015	0.0002	0.6137
max (change in L)or ΔL_{max}	0.1152	4.82	5.74	6.31
Average ΔL for enhancement	0.027	0.52	0.45	1.84
Average ΔL for depletion	0.029	0.3	0.38	1.81

In Table 6, the data for days 10/25/81 and 10/30/81 includes all density values in the analysis including those that *Persoon et al.*, [1988] said "were not clearly known". A range of density values and enhancement/depletion ducts are considered in this thesis and hence data from Table 5 or Table 6 can be used.

Other duct width numbers obtained from previous work for lower L shells are as given in Table 7:

Table 7: Duct Width for Lower Latitudes or L-Shells From Past Work

Reference	L-shell	Duct Width at the Equator (km)
Smith and Angerami. [1968]	3	400
Angerami. [1970]	4.1-4.7	223-430
Scarf and Chappell. [1973]	3.1-3.5	68-850
Carpenter et al., [1981]	4-5	630-1260
Koons. [1989]	4-5	~500
Sonwalkar et al., [1994]	2.94	367

In Table 7, duct width is specified at the equator for whistler ducts that extend between hemispheres. In this thesis, the ducts represent the auroral cavities and density enhancements in the polar and auroral regions of the magnetosphere. These cavities and enhancements modify the wave propagation path but unlike the whistler ducts, the auroral hiss need not be trapped in these cavities for the entire path of propagation. From Table 5 and Table 6, it is seen that the average ΔL varies between 0.03L and 1.8L. A minimum change of 0.0002L was observed on 10/30/81 when density changed from 4.75 to 4.5 el cm^{-3} at ~ 1302 UT, 3.6 R_E, and ~ L = 15.6. A maximum change of 6.31L was observed on 11/19/81 when density stayed constant at 3.75 el cm^{-3} between 1855 UT and 1856 UT for radial distance R_E between 3.87 and 3.9 and ~ L = 142.3 and 148.6. The duct width in km for the data presented in Table 5 and Table 6 are as follows in Table 8.

Table 8: Duct Width (km) at 2 and 4 R_E for the Data in Tables 5 and 6

Duct Width in 'L'	Duct Width at 2 R_E	Duct Width at 4 R_E
0.0002	0.01 km	0.04 km
0.03	2 km	6 km
1.8	116 km	338 km
6.31	406 km	1183 km

In Figure 3.2.6, the enhancement and depletion cavities observed by *Persoon et al.*, [1983] are simulated using the ray-tracing program with the parameters

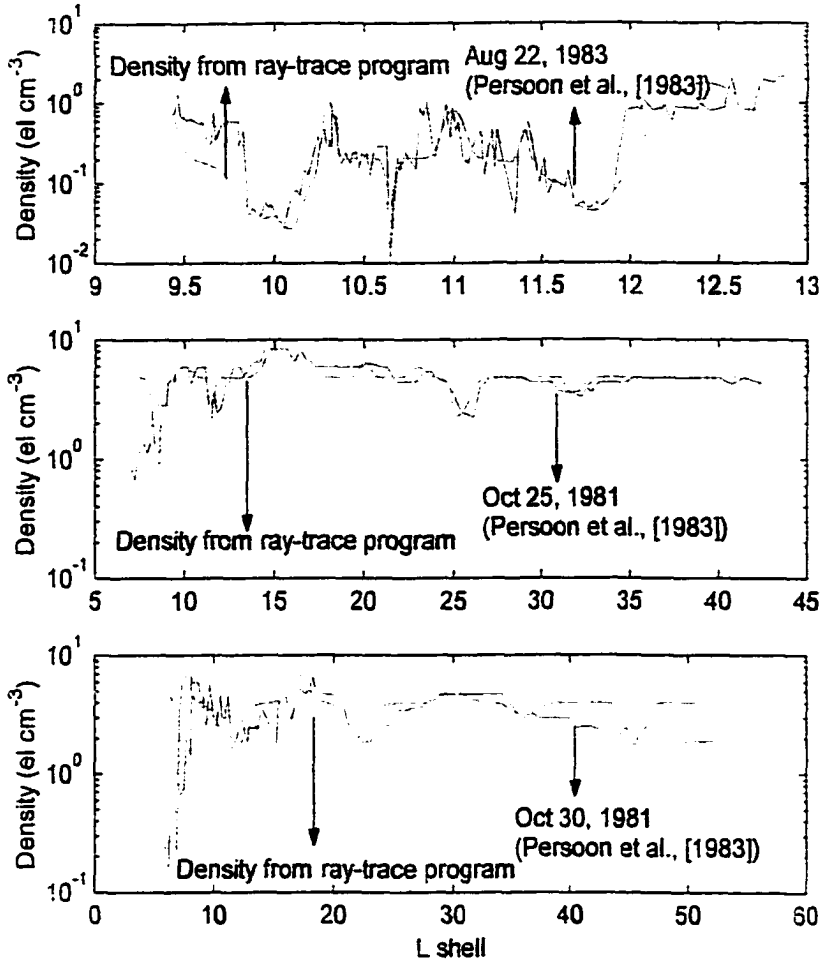

Figure 3.2.6. Modeling of density enhancement and depletion ducts to represent the auroral density enhancements and cavities. Density enhancement and depletion ducts can be modeled in the ray-tracing program to represent the auroral density enhancements and cavities. The solid red line is an approximation, obtained by using the ray-tracing program, of the auroral cavities and enhancements observed by DE 1 (solid blue line) [*Persoon et al.*, 1983] on (a) August 22, 1983; (b) October 25, 1981; (c) October 30, 1981.

discussed in this chapter. Figure 3.2.6a represents the auroral cavities and enhancements observed by DE 1 on August 22. 1983. The approximate altitude of the satellite during the pass was 18800 km and the universal time varied between 0105 UT and 0140 UT. The data shown in Figure 3.2.6b was observed by DE 1 on October 25. 1981 at an approximate altitude of 15300 km between 1610 UT and 1710 UT. Figure 3.2.6c shows the enhancements and cavities observed in the auroral zone on October 30. 1981 at $\sim$ 15925 km altitude between 1230 UT and 1335 UT.

3.3 Linear Mode Conversion Model

The AH propagation model developed in this thesis suggests that an additional mechanism. meter-scale irregularities. is required at altitudes of a few thousand kilometers to convert whistler mode waves with large θ into whistler mode waves with small θ that can propagate across the Earth-ionosphere boundary. The "linear mode conversion model" [*Ngo*. 1989] is used in this thesis to calculate the amplitude of the scattered electromagnetic and electrostatic waves. In this section the program and the selection of input parameters to the program are discussed.

Meter-scale irregularities are magnetic-field-aligned plasma density irregularities of spatial length $1-100$ m. They are present up to a few thousand kilometers [*Fejer and Kelley*. 1980. and references therein: *Sonwalkar*. 1995]. In order to specify some typical altitude bounds for meter-scale irregularities. the altitudes in the magnetosphere and ionosphere where lower hybrid waves are commonly excited by the meter-scale irregularities are used. Lower hybrid waves are excited by VLF transmitter pulses at altitudes between $\sim 1000-3500$ km for $L > 2.5$ [*Sonwalkar* 1995] and this suggests that a possible altitude where meter-scale irregularities can be found is $\sim$ 3500 km. For $L < 2.5$ meter-scale irregularities are present at altitudes as high as 8200 km [*Ngo*. 1989]. Figure 3.3.1 is a schematic of the region where meter-scale irregularities can be found. In *Ngo* [1989] and *Sonwalkar* [1995] the altitude limits were specified when spectral broadening of the initially narrowband signal was observed on a moving satellite. However. in

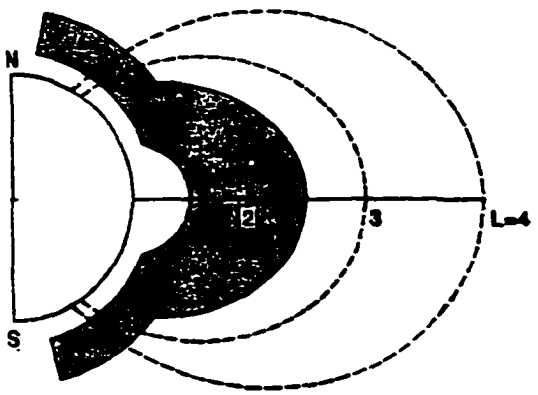

Figure 3.3.1. Regions of the magnetosphere and topside ionosphere where meter-scale irregularities convert large $\theta \sim \theta_R$ whistler mode waves into small θ whistler mode waves [*Sonwalkar*, 1995].

reality meter-scale irregularities can and may be present at altitudes greater than 3500 km. For this thesis, meter-scale irregularities are assumed to exist at altitudes between 3000 km and 5000 km.

The density enhancement of the meter-scale irregularities is variable and can vary between $10 - 150\%$ [*Ngo*, 1989]. A possible explanation for the variation in density is that at the boundary of the meter-scale irregularity electromagnetic waves are converted to electrostatic and electromagnetic waves. The stimulated electrostatic waves produce scattering and precipitation of electrons which in turn enhances the plasma density of the irregularity [*Bell and Ngo*, 1988]. To reasonably represent the meter-scale irregularities, density enhancements between 10 and 100% are considered. Additionally, meter-scale irregularities are assumed to have different shapes and sizes. The three shapes considered for the meter-scale irregularities are (1) a sharp boundary, (2) meter-scale irregularities with a rectangular slab density distribution where the width of the slab varied from 1λ to 100λ (scattering occurs across the width of the slab), and (3) meter-scale irregularities with a Gaussian density distribution where the width of the slab varied from 1λ to 100λ. For reference, λ is ~ 1.75 m for $N_{e,ref} = 10$ el cm^{-3} at 2 R_E altitude and $\Lambda = 70°$ and ~ 1 m for $N_{e,ref} = 50$ el cm^{-3} at 2 R_E altitude and $\Lambda = 70°$.

Full wave linear scattering program developed by *Ngo* [1989] and modified for this thesis to perform numerical calculations is used to convert large-θ AH to small-θ AH that can eventually fall in the transmission cone and penetrate to ground. The computer program solves the problem of a whistler mode plane wave scattering from a plasma density irregularity. The code implements the method of full wave solution to find the amplitudes of the waves stimulated by an input wave that scatters from a plasma density irregularity. The code finds the amplitude of the waves stimulated by an input wave by dividing the irregularity into a number of layers and applying full wave solution techniques to each layer. A complete discussion of the equations programed in the code are given by *Bell and Ngo* [1990].

For a simple explanation of the code consider Figure 2.5.1. Figure 2.5.1 characterizes the magnetoplasma as two homogeneous semi-infinite regions, 1 and 2, where the boundary is parallel to the ambient magnetic field $\overline{B_o}$. The

cold plasma density in each region differs slightly. In Figure 2.5.1 and in the passive full wave linear scattering program, the quartic dispersion relation is used to characterize a uniform cold magnetoplasma. For any given direction of propagation, four normal wave modes exist. Thus when a normal wave mode scatters from a magnetic-field-aligned irregularity, four normal wave modes are excited. Two of the four excited normal wave modes are quasi-electrostatic and have relatively short wavelengths. By Snell's law, for an incident wave at large wave-normal angle that propagates toward the boundary from the left and excites four normal mode waves, the component of the refractive index parallel to the boundary for the four normal mode waves should have the same value. The refractive indices for the scattered waves in Figure 2.5.1 are represented by the dot-dash line $n_{z1} = n_1 \cos\theta_{inc}$. This line intersects the refractive index surface at the four points that define a normal mode solution to the wave equation. "REFL ES" and "TRANS AH" in Figure 2.5.1 have their wave-normal vector very close to θ_R and are quasi-electrostatic waves. "TRANS WM" in Figure 2.5.1 is an electromagnetic wave that has a small θ and is also the wave that will eventually fall in the transmission cone of the proposed model. A point to note for the sharp boundary case is that only those stimulated waves that carry energy away from the boundary physically exist. In general, for a stratified medium all four normal modes are physically realizable in each region.

4. Determination of Auroral Hiss Source Region, Cold Plasma Electron Density, and Energetic Electron Energy From Auroral Hiss Observations

In this chapter, auroral hiss observations are used to determine the hiss source region, energetic electron energy and the cold plasma electron density along the auroral field line. The new mechanism of AH propagation from source latitudes to the ground, proposed in chapter 2 is used for remote sensing of the magnetosphere in this chapter with the AH spectra recorded at South Pole (SP) station (Figure 1.3.1c). By way of an example, this chapter shows a method to remotely sense from the ground the cold plasma electron density in the auroral magnetosphere. These measurements to date have only been made on spacecraft. The significance for such measurements are discussed in section 1.4.

AH has distinct spectral features. When the AH spectrum is structureless and steady over minutes and hours it is called CAH. The upper and lower cut-off frequency can be determined from CAH spectra. However, because of its structureless spectra it is difficult to make other inferences from its spectra. IAH spectra on the other hand, is highly structured, fluctuates over seconds and shows dispersion. The frequency-time data (or dispersion data) from the IAH spectrum is used in this thesis to make inferences about the source region of AH, the energetic electron energy of the electrons generating AH and the cold plasma electron density along the auroral field line.

A number of steps are involved in the process of determining the cold plasma electron density from IAH spectra. Section 4.1 provides a theoretical approach to determine the cold plasma electron density from AH dispersion data. In section 4.2 the sample data used to illustrate the remote sensing method proposed in this thesis is presented. Section 4.2 also discusses the various steps involved to invert (or make inferences from the observed data) the AH spectral data. In section 4.3 data from South Pole station, collected on July 09, 1996 is used as an example to illustrate how the AH dispersion data can be inverted.

4.1 Theoretical Approach to Determine Electron Density Along Auroral Field Lines From Ground Observations of Auroral Hiss

In this section a theoretical outline of the approach that is used to measure the auroral hiss source region, energetic electron parallel resonance energy, $E_{\|}$, and the cold plasma electron density along auroral field lines is provided. Given an IAH spectra the first step in the process to invert data involves determining the auroral field line(s) along which the hiss observed in the spectra could have traveled. The auroral field line(s) can be estimated from the recording station location. For example, in this thesis the IAH spectra used, was recorded at South Pole (SP). The invariant latitude at the South Pole station is 79° (L=27.47). This implies that the hiss recorded at SP station must have traveled along invariant latitudes around 79°. The geometry to determine the field lines along which the hiss could have traveled is discussed in the next section. The next step would be to determine the dispersion (time delays of various frequencies relative to a fixed frequency) for the different frequencies from the discrete IAH spectra. The IAH spectra also shows the lower and upper cutoff frequencies. The lower cutoff frequency or frequencies give information on the location of meter-scale irregularities. AH penetrates the ground after scattering from the meter-scale irregularities and the location of the meter-scale irregularities plays an important role in the observed dispersion data.

A tentative density model(s) is next constructed from past auroral density models. For example, in this thesis the initial density model is constructed with experimental data results from *Persoon et al.*, [1983, 1988], *Persoon* [1988]; and *Kletzing et al.*, [1998] and from theoretical models of the auroral region plasma density [*Maggs and Lotko*, 1981; *Gurnett* 1978; *Jorgensen* 1968]. Using this tentative density model, ray-tracing simulations can be performed to determine the group time for a few (say 4 to 5) frequencies observed in the IAH spectra to reach the ground. Since AH is generated by energetic electrons that can have a range of values, ray-tracing simulations have to be done for a range of energy ($E_{\|}$) values or initial wave-normal angles (θ) ($E_{\|}$ is a function of the initial wave-normal angle, equation 2.3.2). Also, different frequency waves can be generated at different altitudes. The f_{pe} and f_H for each density model uniquely determines

the upper altitude limit for each frequency while f_{LHR} sets the lower altitude limit. Ray-tracing simulations have to consider the different possible altitudes at which the different frequencies could have been generated. Dispersion can then be computed from the calculated group time (t_g) and compared with the measured dispersion. If a satisfactory match is obtained the estimated source location of AH can then be used with another set of frequencies to improve the density model. This will be an iterative process until a good match is obtained between the measured dispersion and that calculated from the ray-tracing simulation. If photometer data is available, then the energy of the electrons from photometer data can be used to estimate the initial wave-normal angles at which these frequency waves were injected. If the ionospheric exit point of hiss is known from a HF direction finder, for instance, then the minimum depletion or enhancement required to trap the wave along a particular field line can be estimated. In the absence of photometer data or a direction finder, as in the case of this thesis, a match in dispersion is obtained for a range of possible $E_{||}$ values along possible field line(s) that can have a different electron concentrations.

4.2 Analysis of Auroral Hiss Spectra

Auroral hiss is a broadband whistler mode plasma wave emission. The spectrum for AH resembles that of a band-limited noise. AH has distinct spectral characteristics. When it is structureless and steady over minutes and hours it is called CAH. It is called IAH when it is highly structured, shows dispersion and fluctuates over seconds. In this thesis, the dispersive feature in IAH spectra is used along with the lower cutoff frequency data from the spectra to make inferences about the auroral magnetosphere. In this section the IAH spectra recorded at SP is analyzed using the proposed mechanism, developed in chapter 2.

4.2.1 Auroral Hiss Spectra Data

Auroral Hiss spectra used to test the proposed mechanism and for data analysis in this thesis and in particular this chapter are shown in Figures 4.2.1.1 (a-f). These spectrograms (Figures 4.2.1.1(a-f)) were collected by the VLF group of Stanford University, California, at a South Pole (SP), Antarctica station (Λ = 79°, λ_g = 90°). The spectrograms show 6 days of data. On each day, except July 09, 1996, (0050 UT) ~ 54 seconds of AH data was recorded. On July 09, 1996 (0050 UT) 30 seconds of AH data was recorded. The hiss events observed on each day and used for data analysis in this thesis are as marked on each IAH spectra. A total of 204 hiss events were selected from these 6 days of data: 36, 50, 28, 20, 22, and 48 hiss events were selected from July 09 (0050-0051 UT), July 01 (0120-0121 UT), June 30 (0250-0251 UT), June 30 (0235-0236 UT), May 16, (0005-0006 UT), and May 15, (2335-2336 UT) respectively.

The IAH spectra shown in Figures 4.2.1.1(a-f) were all measured between 2335 UT and 0235 UT during the months of May, June and July. South Pole experiences winter during the months of May, June and July. So for the examples in this thesis, the VLF ducts terminate around 1800 km with a scale height of 800 km. The lowest frequency reading on each hiss event for each day provides an approximate altitude at which meter-scale irregularities must have been present to scatter the AH data to the ground. On every spectrogram it is seen that there is more than one lower cutoff frequency. This implies that meter-scale irregularities must be present over a range of altitudes to scatter the AH impinged on them. The lowest AH frequency observed on all 6 days on different field lines was ~ 6 – 7 kHz. The highest frequency observed from these 6 days of data was ~ 20 kHz, set by the receiver. Based on these numbers the data analysis in the consecutive sections are done for 6, 10, 15 and 20 kHz AH emissions.

To show how IAH spectra data can be used to study the auroral magnetosphere, one day of IAH spectra was selected. The choice was made after observing the following characteristics in each spectra. A maximum of 50 hiss events were observed on July 01, 1996. However, the lowest frequency observed on this day from the IAH spectra was ~ 6.3 kHz and the highest frequency observed was ~ 13.5 kHz. It was felt that this range of frequencies was rather small to be

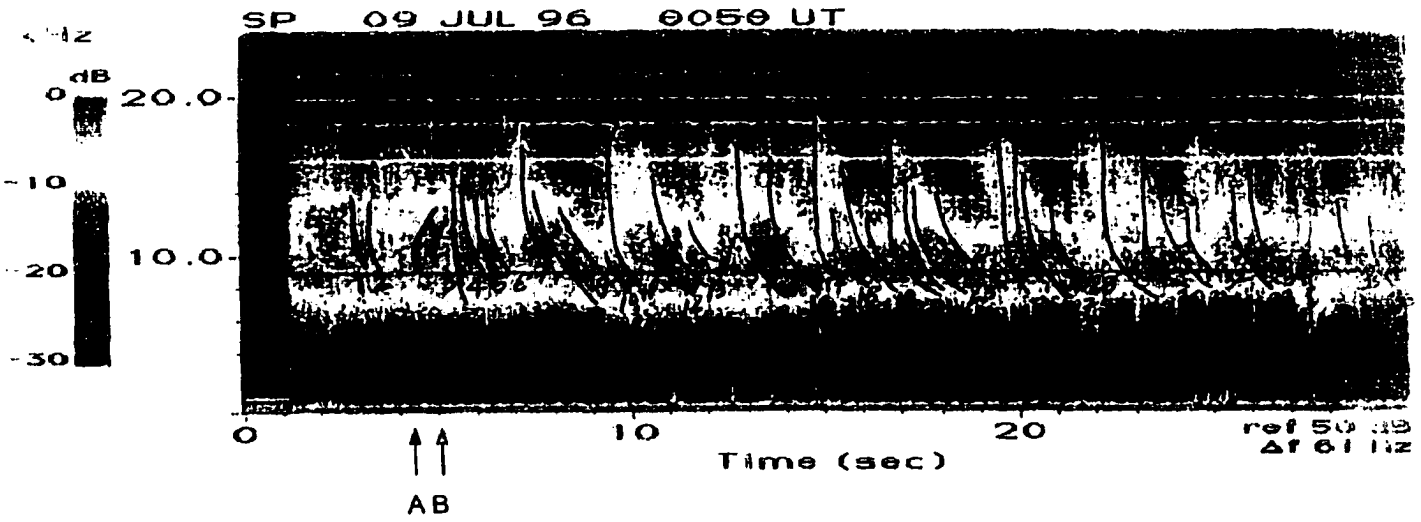

Figure 4.2.1.1a. *Examples of* IAH spectra observed at South Pole, Antarctica on July 09, 1996 (0050 UT). The 36 hiss events used for data analysis is marked on the spectrogram.

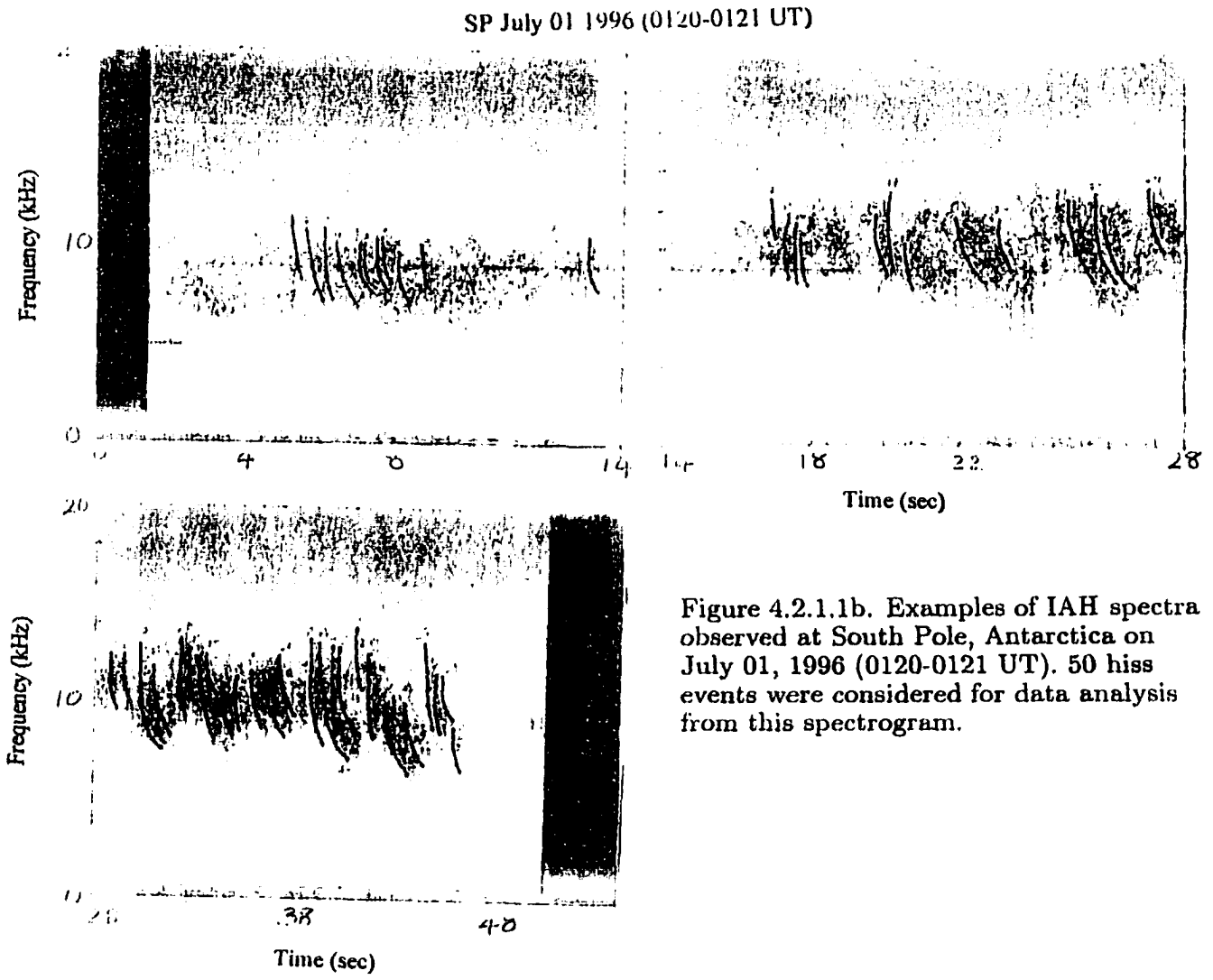

Figure 4.2.1.1b. Examples of IAH spectra observed at South Pole, Antarctica on July 01, 1996 (0120-0121 UT). 50 hiss events were considered for data analysis from this spectrogram.

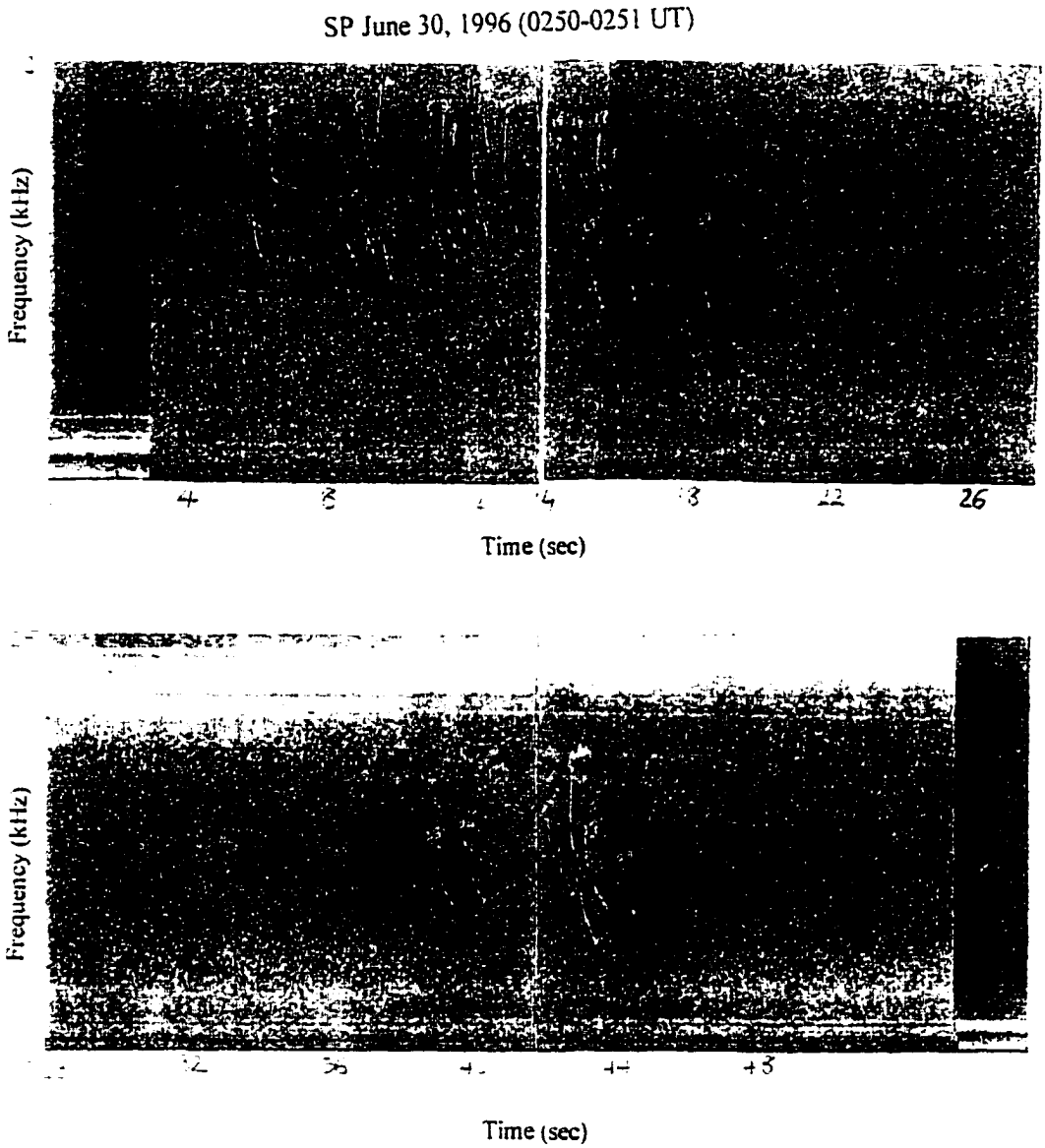

Figure 4.2.1.1c. Examples of IAH spectra observed at South Pole, Antarctica on June 30, 1996 (0250-0251 UT). 28 hiss events were considered for data analysis from this spectrogram and are as marked on the spectrogram.

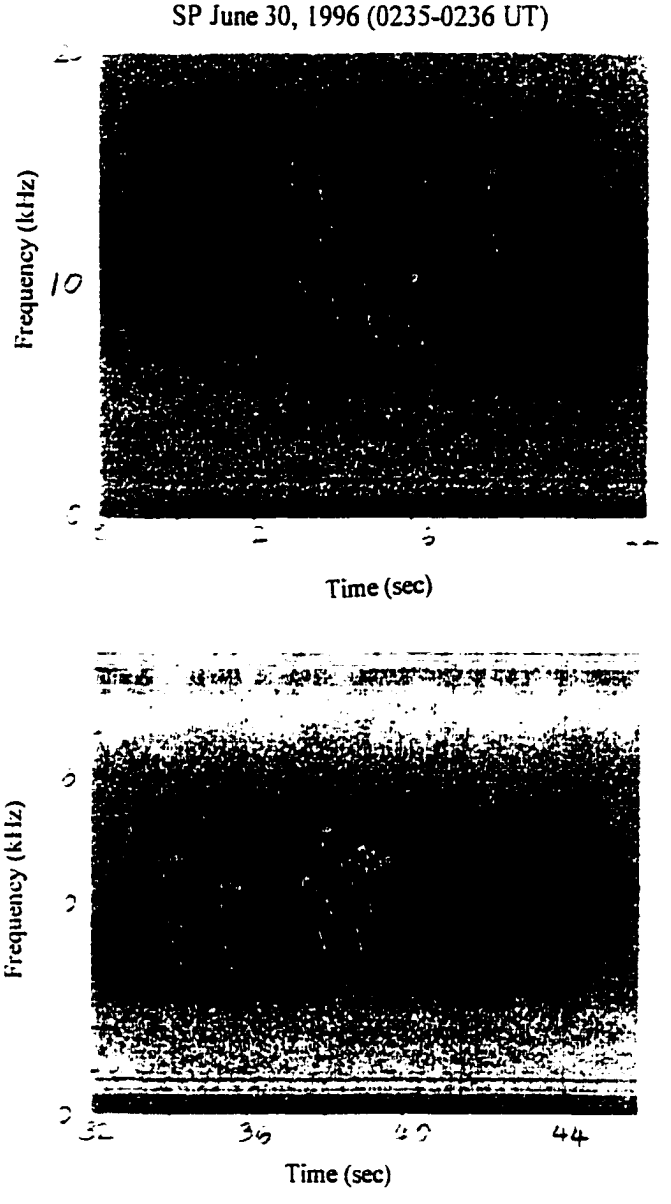

Figure 4.2.1.1d. IAH spectra recorded at South Pole, Antarctica on June 30, 1996 (0235-0236 UT). A total of 20 hiss events were traced for this time period. 10 hiss events each were observed between 02:35:08-02:35:22 and 02:35:32-02:35:46.

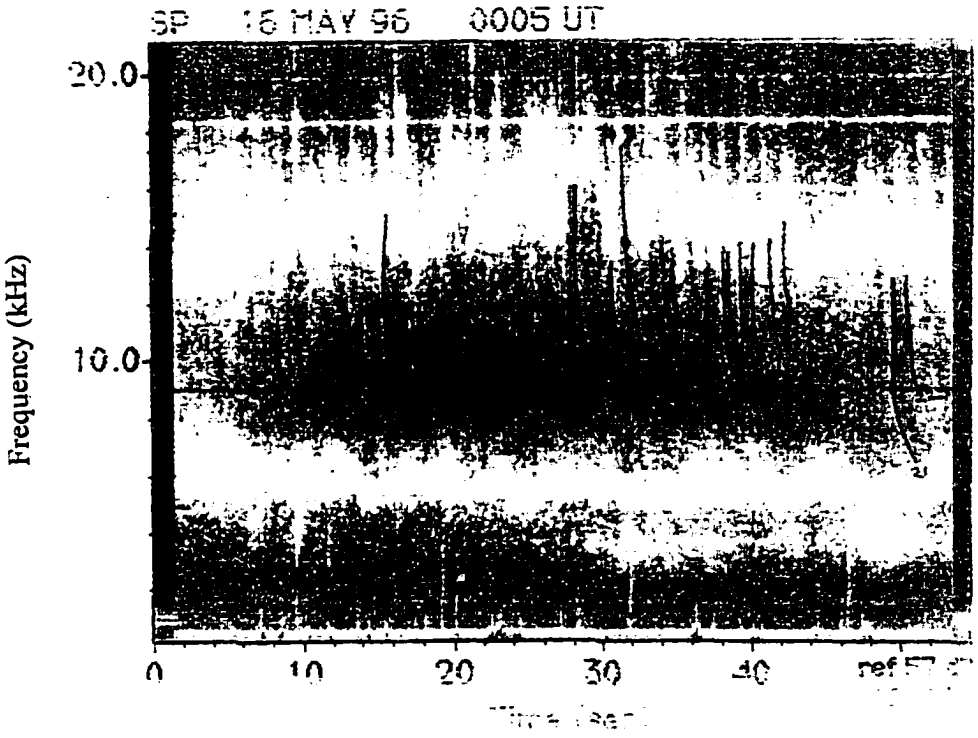

Figure 4.2.1.ie. Examples of IAH spectra observed at South Pole, Antarctica on May 16, 1996 (0005-0006 UT). 22 hiss events were considered for data analysis from this spectrogram.

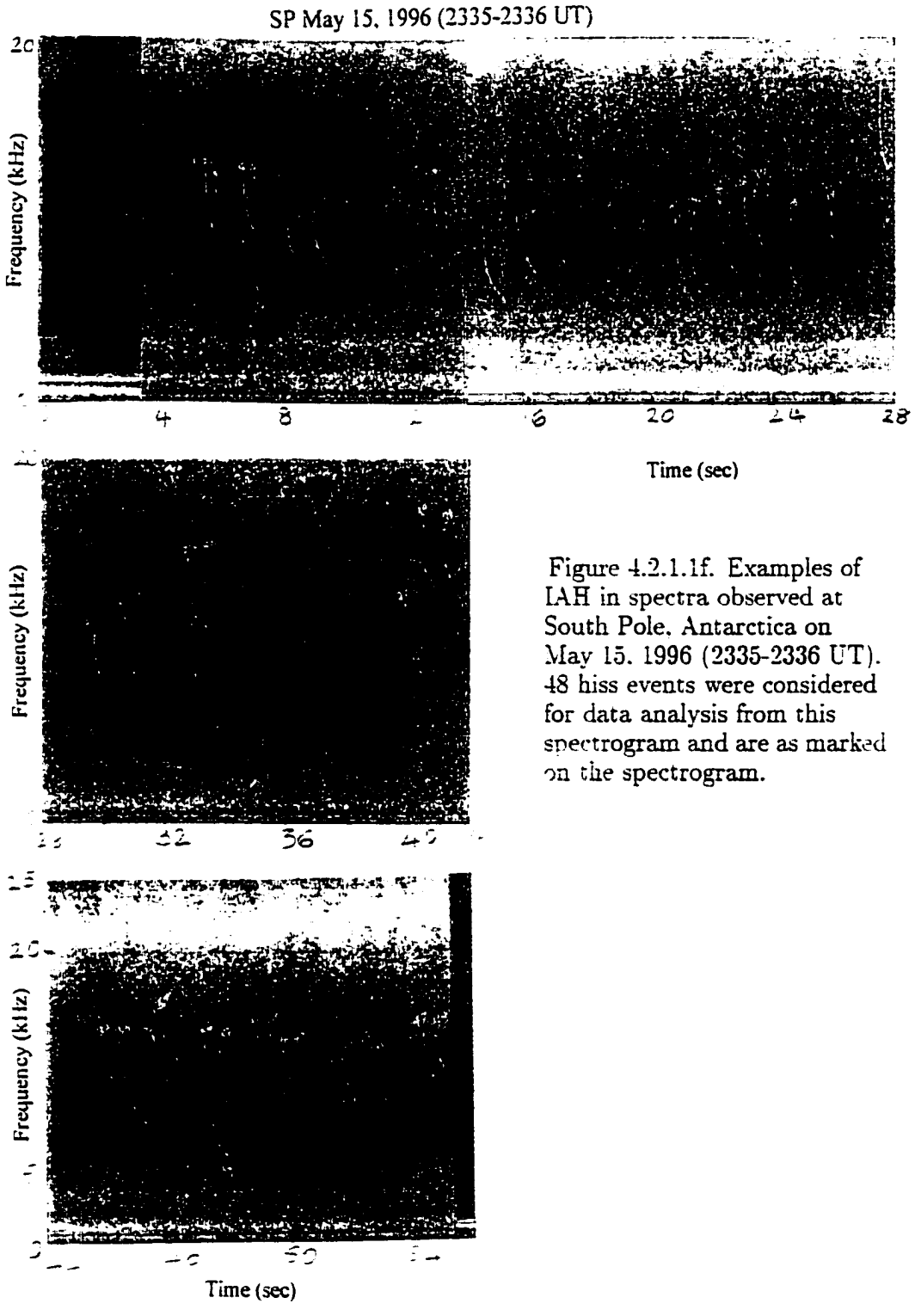

Figure 4.2.1.1f. Examples of IAH in spectra observed at South Pole, Antarctica on May 15, 1996 (2335-2336 UT). 48 hiss events were considered for data analysis from this spectrogram and are as marked on the spectrogram.

considered as a good representative of sample data. The next choice was May 15, 1996 (2335 UT) when 48 hiss events were observed and July 09, 1996 (0005 UT) when 36 hiss events were observed. July 09, 1996 (0005 UT) was selected as the sample data set because it covered a wider frequency range from $\sim 6.9 - 20$ kHz versus $\sim 6 - 17$ kHz for May 15, 1996 (2335 UT). Additionally, the IAH spectra for July 09, 1996 (0005 UT) shows distinct hiss events that vary from a few seconds to a second. Data collected on June 30, 1996 at both times 0250 UT and 0235 UT was not used as a sample data set because at both times fewer hiss events than July 09, 1996 were recorded and the hiss events were concentrated within the first 20 seconds and the last 20 seconds of data with no hiss events in between for either case. The spectra for May 16, 1996 only showed 22 hiss events and a frequency range from 6 kHz to 17 kHz. As a result, the data collected on July 9, 1996 was considered as the best sample data set.

The IAH spectrogram recorded on July 09, 1996 (Figure 4.2.1.1a) is resized and repeated in figure 4.2.1.2a to clearly show the hiss events so that it can be used as an example to invert AH data to determine the cold plasma electron density, energetic electron parallel resonance energy and source region of AH along auroral field lines. The 36 hiss events marked on the spectrogram in Figure 4.2.1.2a is reproduced in 4.2.1.2b, as an example, to show the accuracy of the data collected for this thesis.

The IAH spectra in Figure 4.2.1.2 shows that there is more than one lower and upper frequency cutoff for the hiss events recorded on this day. The spectra also shows a range of dispersion values between the same two frequencies. For example, consider hiss events numbered 1, 4, 11, 24, 32, and 35 in Figure 4.2.1.2. The lower cutoff frequency for hiss events 1, 4, and 35 is 9 kHz and the upper cutoff frequency is 14 kHz. The dispersion (time delay difference) observed between 14 kHz and 9 kHz for these three hiss events are 200 ms, 370 ms and 790 ms respectively. Similarly, the lower and upper cutoff frequency for hiss events 11 and 24 is 8 and 14 kHz, respectively, but the dispersion between frequencies 14 kHz and 9 kHz is 430 ms and 1.21 s, respectively. Hiss event 32 has a lower and upper cutoff frequency of $\sim$ 8.8 and 14 kHz and the dispersion observed between 14 and 9 kHz for this event is 710 ms. The above data suggests that the difference in dispersion values for the same 2 frequency waves may be a

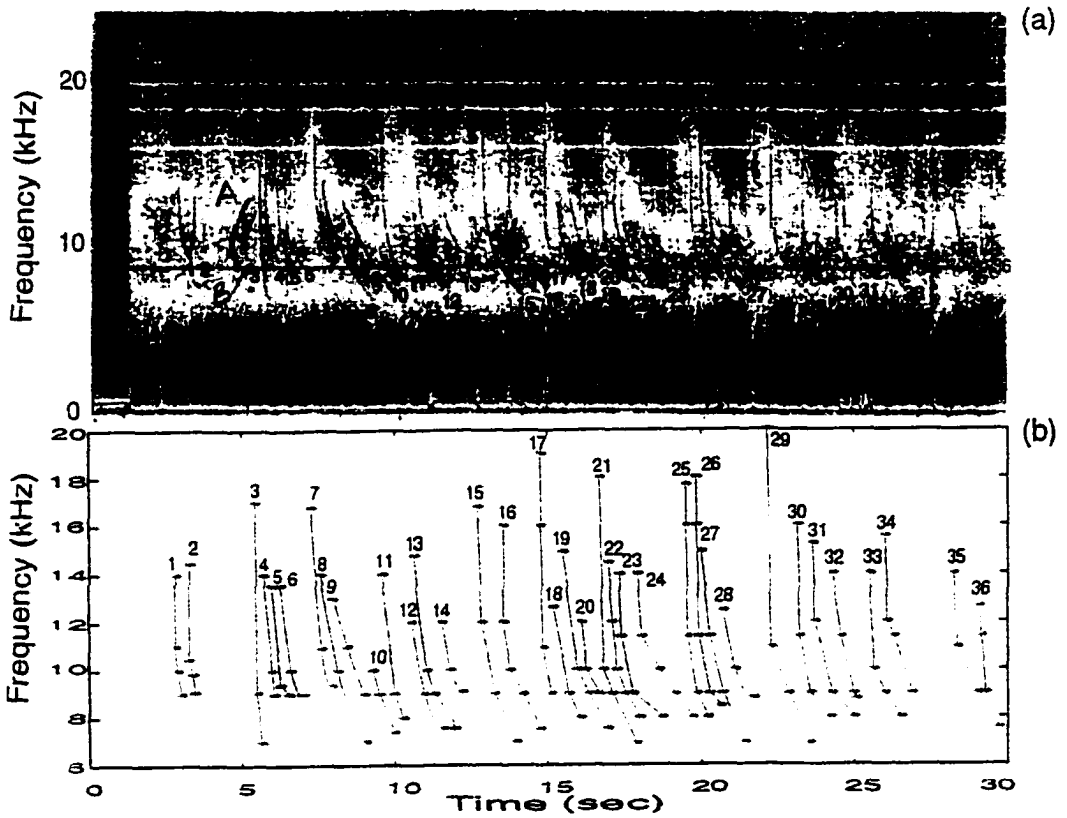

Figure 4.2.1.2. (a) IAH spectra recorded at South Pole, Antarctica on July 09, 1996 (0050-0051 UT). Dispersion was computed from the 36 hiss events marked on this spectrogram. (b) Reproduction of the 36 hiss events, marked in figure 4.2.7a, from the dispersion data collected to show the accuracy of data collected.

result of (1) the 2 frequencies being generated at the same altitude in one case and different altitudes in another case. and/or (2) the 2 frequencies propagating along different field lines. and/or (3) the 2 frequencies are generated by different energetic electrons for each event. In section 4.2.3 and 4.2.4. group time for each frequency is studied as a function of source altitude. cold plasma electron density. and energetic electron energy and in these sections it will be shown that dispersion is a function of frequency. source altitude. background electron density. and energetic electron energy that generates the hiss.

The horizontal lines in all the IAH spectra (Figures 4.2.1.1(a-f)) at ~2. 9. 16. 18. 20 kHz seem to be local power line noise. The IAH spectra also shows events with a falling tone or discrete parabolic shapes (for example please refer to the 2 events marked A and B. where the low frequency wave travels faster than the high frequency wave). These events are not specifically numbered in the figures because they are not used in the sample data set. However. they are briefly discussed later in section 4.2.4. Lastly. the range of dispersion observed for each frequency in the IAH spectra could be the result of AH scattering from meter-scale irregularities. It could also be due to the hiss being generated over a period of time.

4.2.2 Determination of Auroral Field Line

The main objective in this section is to determine the field line or lines along which AH must have propagated to penetrate the ground and be recorded in the spectrogram. The location of the recording station gives an idea of the auroral field line along which the hiss could have propagated from its source region to the ground. In the new mechanism proposed in this thesis. large wave-normal AH penetrates the ground when it scatters from meter-scale irregularities. From chapters 2 and 3. it is clear that hiss propagating along more than one field line can scatter from meter-scale irregularities and fall in the transmission cone. In this section and the following paragraphs. the range of auroral field lines along which the observed IAH in our example data could have propagated is determined.

Impulsive auroral hiss (IAH) is observed when there is a visible aurora overhead [*Martin et al.*, 1960; *Helliwell et al.*, 1960] while continuous hiss (CAH) is observed equatorward about 600 km from a steady auroral arc [*Swift and Kan*, 1975; *Srivastava*, 1976]. To define the spatial distribution of aurora and the region of observed auroral hiss, *Makita* [1979] statistically examined 50 events, at 8 kHz (CAH) and 64 kHz (IAH), observed by an all-sky camera. He then divided the photographs into 4 parts along the geomagnetic latitude with elevation angles of 0° to 45° and 45° to 90° both in the north and south directions. He further assumed the altitude of the aurora at 100 km. Of the 50 events he observed, 50% of CAH correlated to aurora more than 100 km from the zenith (i.e., it was not within the 45° cone) while 60% of IAH related to aurora were located within 100 km in the $N - S$ direction from the zenith (i.e., it was within the 45° cone).

In this thesis, using Makita's [1979] observations, $\sim$ 100 km radius area on either side of the field line on the ground is assumed to be the region 'beneath' an overhead aurora. Now, if a transmission cone of 10° on the ground is assumed, then at 5000 km altitude IAH has to be within $\sim$ 440 km of the field line to penetrate to the ground. However, with $\sim$ 100 km radius range around the field line on the ground the distance on either side of the field line at 5000 km altitude increases to $\sim$ 540 km. These numbers imply that if IAH is recorded on the ground then the IAH could have propagated along any field line within $\sim$ 540 km (Figure 4.2.2.1) of the receiving station field line at 5000 km altitude before scattering from meter-scale irregularities. For example, consider the hiss events observed in the sample data set, July 09, 1996 (Figure 4.2.1.2). The data was recorded at South Pole where L=27.47 ($\Lambda = 79°$). If the AH observed on the ground scattered from meter-scale irregularities at 5000 km then the hiss could have traveled along on any field line between L=19.81 and 40.83 or ($77° \leq \Lambda \leq 81°$) before scattering into the transmission cone.

Figure 4.2.2.1 shows the geometry of how the angles and numbers were derived. Briefly, if IAH can be observed within 100 km of the receiving station field line then the transmission cone is $\sim$ 12°. The transmission cone is on the surface of the Earth. The same angle from the center of the Earth is $\tan^{-1}(537/11370) = 2.7°$.

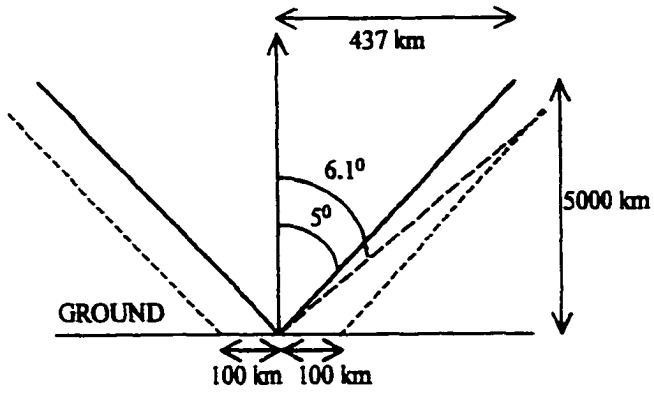

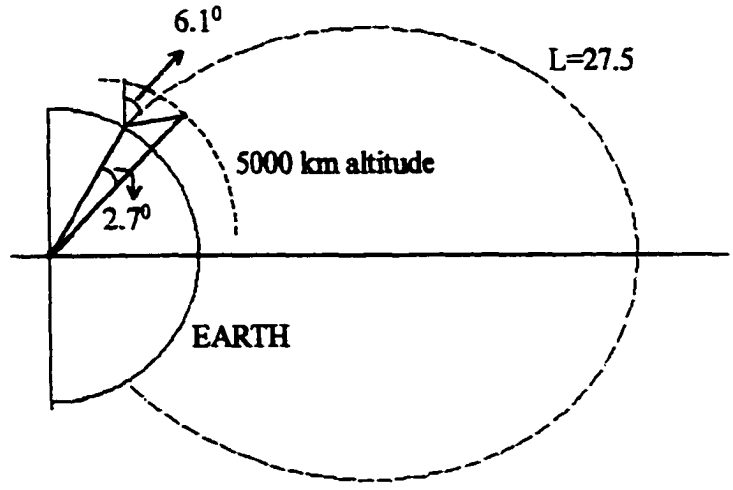

Figure 4.2.2.1. Schematic of the geometry to show how the transmission cone angle at the foot of the field line can be projected to determine the area around the field line where IAH can be observed. AH that is scattered within (437+100) km penetrates the ground and is observed within ~ 100 km of an overhead aurora.

If R_E is the radius of the Earth and λ_m is the angle from the center of the Earth to the field line at 5000 km altitude then for $L = 27.5$. $\lambda_m = \cos^{-1}((R_E + 5000)/(6370 * 27.5))^{1/2} = 75.2$. Since IAH can fall within 2.7° of the field line the L-shell limits are: $(R_E + 5000)/(R_E * \cos^2(75.2 + 2.7)) = 40.8$ ($\Lambda = 81°$) and $(R_E + 5000)/(R_E * \cos^2(75.2 - 2.7)) = 19.8$ ($\Lambda = 77°$).

4.2.3 Ray-Tracing Simulations

In this section the group time for 6. 10. 15. and 20 kHz waves to travel from source region to the ground is calculated. 6. 10. 15. and 20 kHz frequency waves are selected because the data set discussed in section 4.2.1 shows that the frequency range in the data set is between 6 and 20 kHz. To reasonably analyze the data. four frequencies (6. 10. 15. and 20 kHz) are selected. These four frequencies are generated by 0.5. 1 and 10 keV energetic electrons at different altitudes for various density models of the magnetosphere and ionosphere. The choice of 0.5. 1. and 10 keV energetic electrons was made because IAH is associated with precipitating electrons with energies $\geq$ 1 keV while CAH is associated with precipitating electrons with energies $<$ 1 keV [*Hoffman and Laaspere*. 1972: *Mosier and Gurnett*. 1972: *Laaspere and Johnson*. 1973: *James*. 1973: *Beghin*. 1989: *Winningham and Heikkila*. 1974: *Ondoh et al*.. 1981: *Ondoh* 1991]. $E_{\|}$ determines the initial wave-normal angle for a given density model. The tentative density models used to represent the density in the magnetosphere and ionosphere are discussed in the next paragraph. The source altitudes for the four frequencies are determined by the respective f_{pe} and f_H for each density model. These ray-tracing simulations are done to calculate dispersion that can be compared with the dispersion measured in the sample data set. When a suitable match is found inferences can then be made about the AH source region and cold plasma electron density along auroral field lines. The invariant latitude used in the ray-tracing simulations is 79°. $\Lambda = 79°$ is selected because the sample data set used in this thesis was recorded at a South Pole station which is at 79° S.

The density in the Earth's ionosphere is highly variable and. as discussed in section 3.2. four density models along with Table 4 and Figure 3.2.5 are used

to model the Earth's atmosphere up to $\sim$ 3000 – 5000 km altitude. Figures 4.2.3.1, 4.2.3.2, 4.2.3.3, and 4.2.3.4 show the density, plasma frequency (f_{pe}), gyrofrequency (f_H), and lower hybrid frequency (f_{LHR}) as a function of altitude for the four ionospheric density models $N_{e,ref}$ = 0.1, 1, 10, and 100 el cm^{-3} defined at 2 R_E altitude and $\Lambda = 79°$. Figure 4.2.3.5 shows the four density models of the Earth's magnetosphere from $\sim$ 5000 – 20,000 km altitude used in this thesis. Figure 3.2.4 shows that the variation in density values at altitudes > 5000 km between $R^{-4.5}$, R^{-5}, and $R^{-5.5}$ collisionless density models is small and either model can be used at these altitudes. Hence for this thesis, for any given reference density, R^{-5} collisionless density model outside the plasmasphere for altitudes > 3500 km is used. Figure 4.2.3.5 shows the density, plasma frequency, gyrofrequency, and lower hybrid frequency as a function of altitude for the four reference magnetospheric density models $N_{e,ref}$ = 0.1, 1, 10, and 100 el cm^{-3} defined at 2 R_E altitude and $\Lambda = 79°$. The other parameters for these density models are as defined in Table 3.

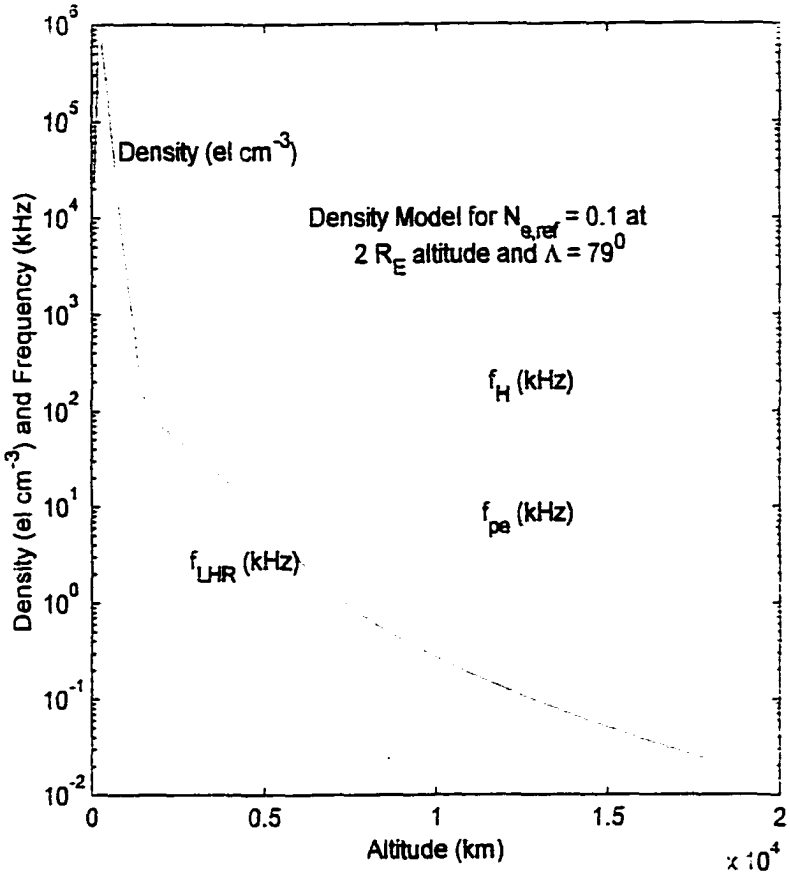

Figure 4.2.3.1. Density of the Earth's atmosphere is determined by the cold plasma density model within the plasmasphere and a R^{-n} collisionless model outside the plasmasphere. Figure shows density as a function of altitude if $N_{e,ref} = 0.1$ el cm^{-3} at 2 R_E altitude and $\Lambda = 79°$ and a R^{-5} collisionless model is used.

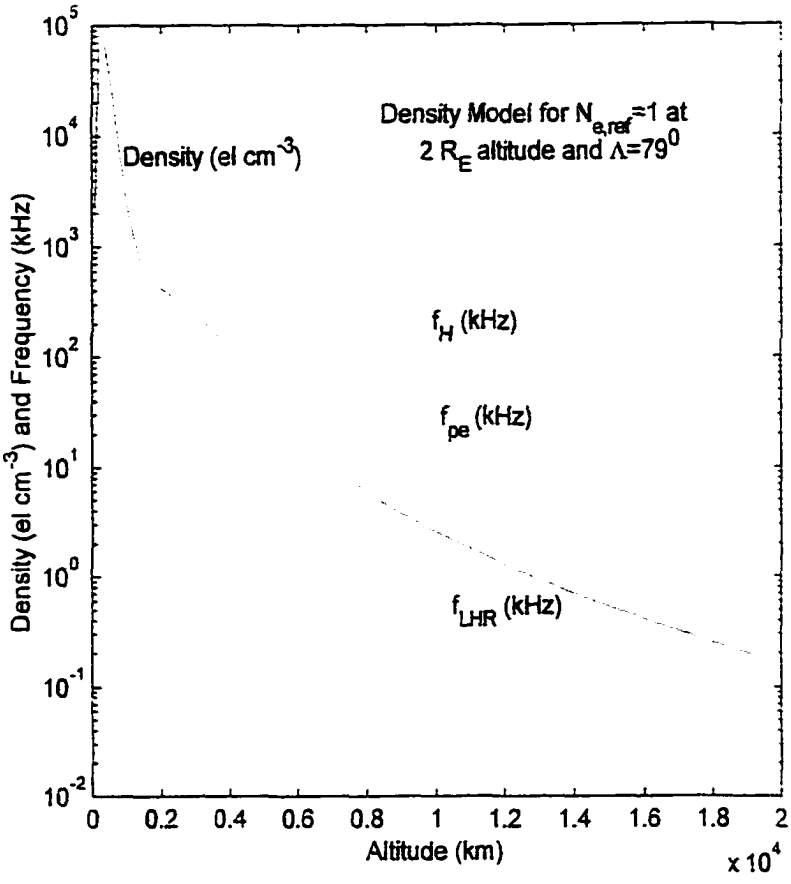

Figure 4.2.3.2. Density of the Earth's atmosphere is determined by the cold plasma density model within the plasmasphere and a R^{-n} collisionless model outside the plasmasphere. Figure shows density as a function of altitude if $N_{e,ref} = 1$ el cm^{-3} at 2 R_E altitude and $\Lambda = 79°$ and a R^{-5} collisionless model is used.

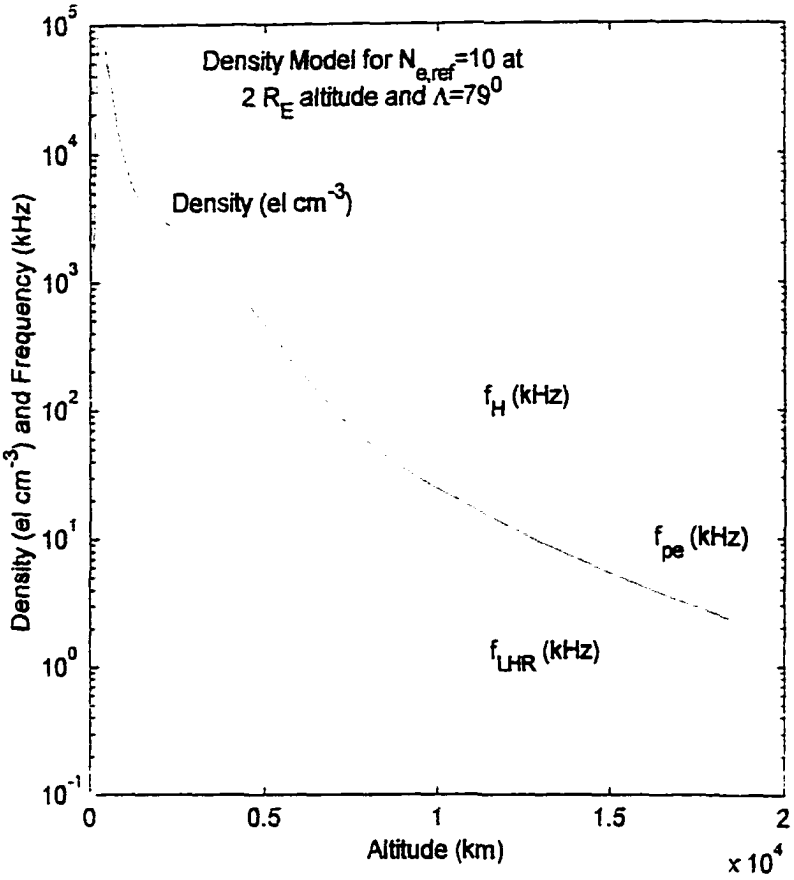

Figure 4.2.3.3. Density of the Earth's atmosphere is determined by the cold plasma density model within the plasmasphere and a R^{-n} collisionless model outside the plasmasphere. Figure shows density as a function of altitude if $N_{e,ref}$ = 10 el cm^{-3} at 2 R_E altitude and Λ = 79° and a R^{-5} collisionless model is used.

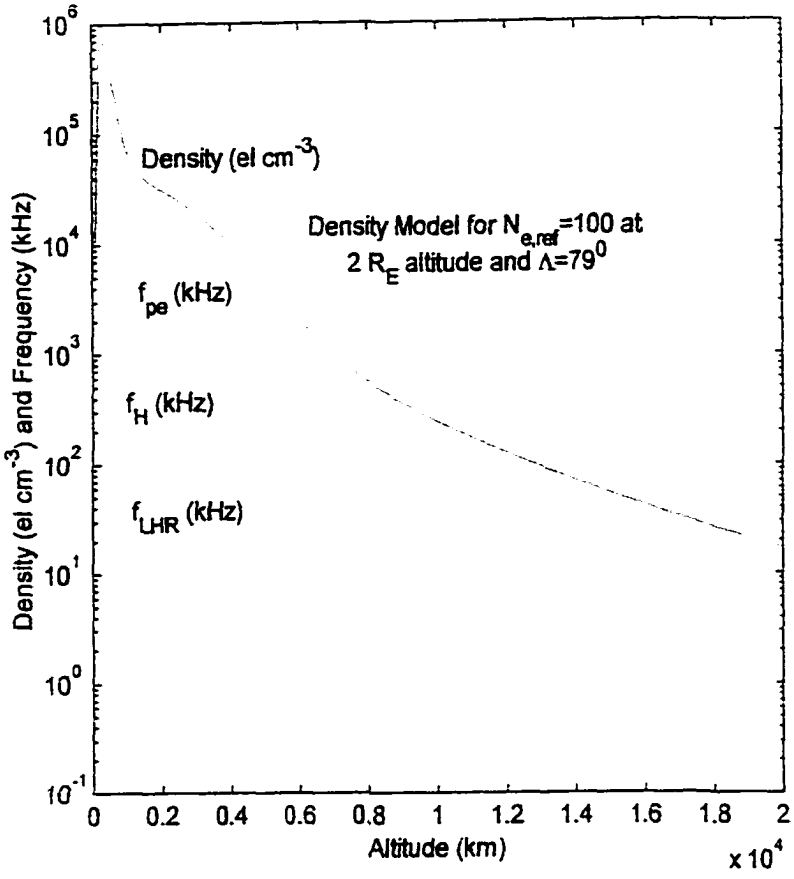

Figure 4.2.3.4. Density of the Earth's atmosphere is determined by the cold plasma density model within the plasmasphere and a R^{-n} collisionless model outside the plasmasphere. Figure shows density as a function of altitude if $N_{e,ref} = 100$ el cm^{-3} at 2 R_E altitude and $\Lambda = 79°$ and a R^{-5} collisionless model is used.

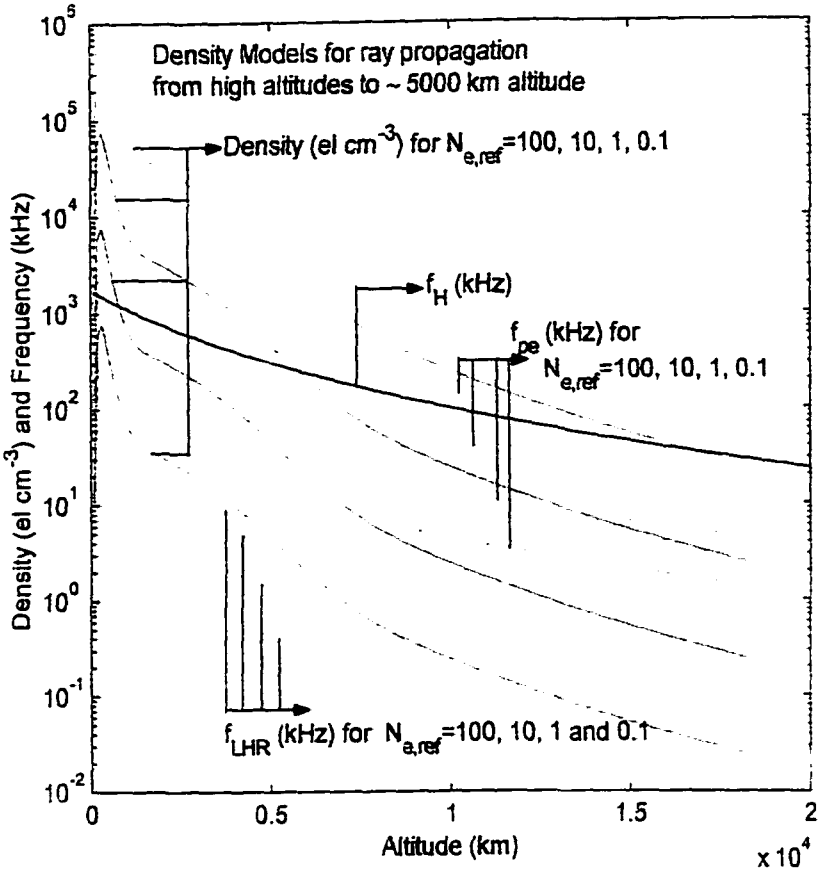

Figure 4.2.3.5. The different density models ($N_{e,ref}$ =0.1, 1, 10, and 100 el cm^{-3} at 2 R_E altitude and $\Lambda = 79°$) of the Earth's atmosphere used to study auroral hiss propagation from high altitudes ($\sim 20,000$) km to $\sim 3000 - 5000$ km. Outside the plasmasphere a R^{-5} collisionless model was used in all cases.

In the following paragraphs, the computed group time t_g for the different frequencies generated by energetic electrons at various altitudes using the density models discussed in the previous paragraph are discussed. For all computations in this chapter, the reference density $N_{e,ref}$ is defined at 2 R_E altitude and 79° invariant latitude. The ray-tracing program discussed in chapter 3 was used to compute the group time. Consider Figure 4.2.3.6(a-c). Figures 4.2.3.6(a-c) show the group time (t_g) of a 6 kHz wave as a function of altitude for different density models. Figure 4.2.3.6a shows t_g as a function of altitude for a 6 kHz wave generated by 0.5 keV electrons for different magnetospheric models. Similarly, Figures 4.2.3.6b and 4.2.3.6c show t_g as a function of altitude for a 6 kHz wave generated by 1 and 10 keV electrons respectively, for different plasma density models. The dotted lines indicate the time taken by a 6 kHz wave generated at high altitudes to reach 3000 km altitude. The solid lines indicate the time taken by a 6 kHz generated at high altitudes to reach 5000 km altitude. Meter-scale irregularities are assumed to be located at 3000 km and 5000 km altitudes to represent a general case (please refer to section 3.3 for details). The red, blue, green and black colors represent the 4 density models. $N_{e,ref}$ = 0.1, 1, 10, 100 el cm^{-3} respectively. Figure 4.2.3.6 shows that t_g decreases as the energetic electron parallel resonance energy, $E_{\|}$, increases because $\theta_{initial}$ decreases. t_g increases as $N_{e,ref}$ increases. This implies that a 6 kHz wave will take longer to reach the meter-scale irregularities if it is generated at high altitudes by low energy electrons along a field line with enhanced density. Figure 4.2.3.6 also shows that a 6 kHz wave scattered by meter-scale irregularities at 5000 km altitude reaches the ground faster than a 6 kHz wave scattered by meter-scale irregularities at 3000 km altitude. As a result, for example, a 6 kHz wave generated by 0.5 keV electrons and scattering from meter-scale irregularities at 3000 km altitude with $N_{e,ref}$ = 1 el cm^{-3} takes longer than a 6 kHz wave generated by the same 0.5 keV electrons and scattering from meter-scale irregularities at 5000 km altitude with $N_{e,ref}$ = 10 el cm^{-3}.

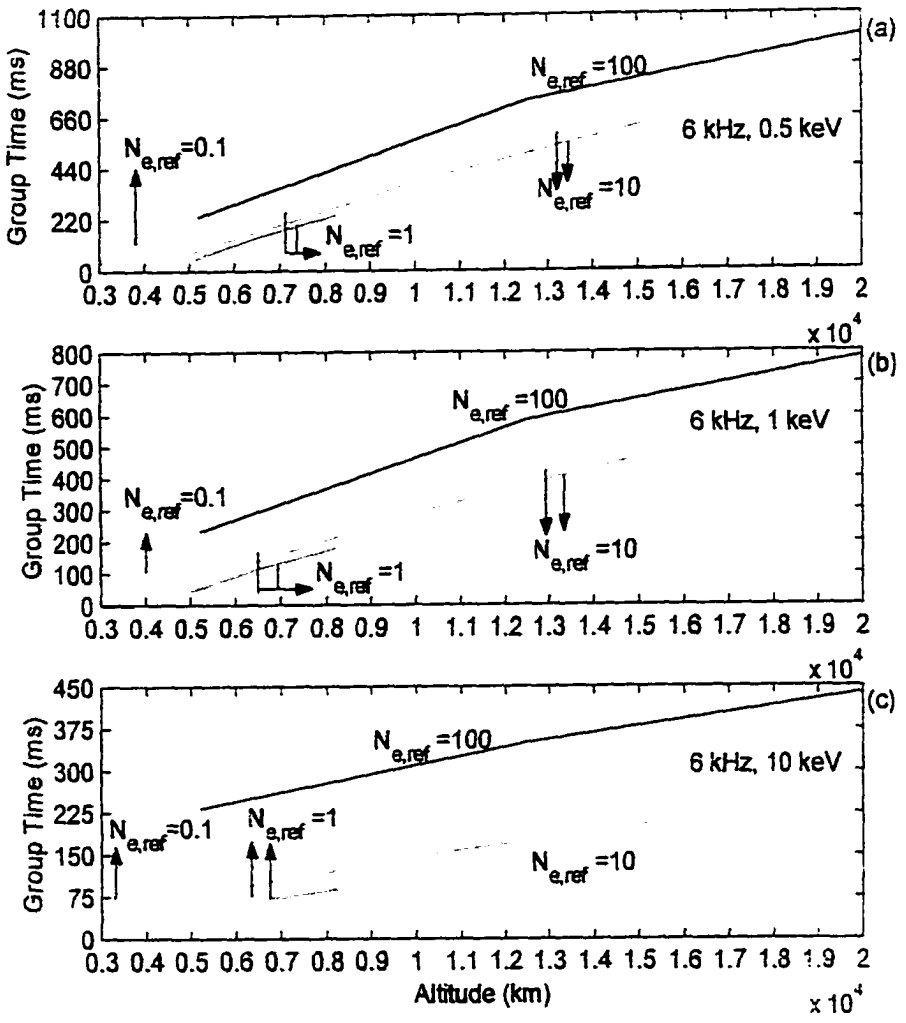

Figure 4.2.3.6. Group time (t_g) of a 6 kHz wave as a function of altitude for different density models and electron parallel resonance energies. The solid lines indicate the group time taken by the wave to scatter from meter-scale irregularities located at 5000 km altitude while the dotted lines indicate the group time taken by the wave to scatter from meter-scale irregularities located at 3000 km altitude. (a) $E_{\|} = 0.5$ keV; (b) $E_{\|} = 1$ keV; (c) $E_{\|} = 10$ keV.

Similarly, consider Figures 4.2.3.7, 4.2.3.8, 4.2.3.9 that show t_g as a function of altitude for 10, 15 and 20 kHz waves. Figures 4.2.3.6, 4.2.3.7, 4.2.3.8, and 4.2.3.9 follow the same format and color code. Similar to a 6 kHz wave, 10, 15 and 20 kHz waves all take longer to reach the meter-scale irregularities if they are generated at high altitudes by low energy electrons. Additionally, all four frequencies reach the ground faster if they are scattered by meter-scale irregularities at 5000 km than by meter-scale irregularities at 3000 km altitude. However as the frequency increases, for $E_{||} \leq 1$ keV the wave travels faster along field lines with enhanced electron density (Figures 4.2.3.8 and 4.2.3.9). Consider Figure 4.2.3.9a where a 20 kHz wave is generated by energetic electrons with $E_{||} = 0.5$ keV. At $\sim$ 8000 km altitude, t_g for the 20 kHz wave with a background electron density defined by $N_{e,ref} = 1$ el cm^{-3} is the same as the t_g for a 20 kHz wave with a background electron density defined by $N_{e,ref} = 100$ el cm^{-3}. These observations show that at low frequencies, t_g increases as $E_{||}$ increases and electron density increases but at high frequencies t_g increases as $E_{||}$ increases but does not necessarily increase as electron density or f_{pe} ($f_{pe} = 9(\text{density})^{1/2}$) increases. The relation between group time, wave frequency and plasma frequency is discussed in detail, later in section 4.2.4.

To compare the group time of each frequency with another frequency, the data shown in Figures 4.2.3.6, 4.2.3.7, 4.2.3.8, and 4.2.3.9 are re-plotted in Figures 4.2.3.10, 4.2.3.11, 4.2.3.12, and 4.2.3.13 such that each figure shows the t_g of the four frequencies for a given $E_{||}$ and and $N_{e,ref}$ density model. The red, blue, green, and black lines represent the group times for 6, 10, 15, and 20 kHz waves. The solid lines represent t_g for waves scattered from meter-scale irregularities at 5000 km altitude while the dash lines represent t_g for waves scattered from meter-scale irregularities at 3000 km altitude. Figures 4.2.3.10, 4.2.3.11, 4.2.3.12, and 4.2.3.13 show that at low altitudes, for a given density model and $E_{||}$, low frequency waves have a higher t_g compared to higher frequency waves. For example, Figure 4.2.3.10a shows that for $N_{e,ref} = 0.1$ el cm^{-3}, below $\sim$ 3300 km $t_g(f = 6) > t_g(f = 10) > t_g(f = 15) > t_g(f = 20)$ and this altitude increases to $\sim$ 4200 km when $E_{||} = 10$ keV (Figure 4.2.3.10c).

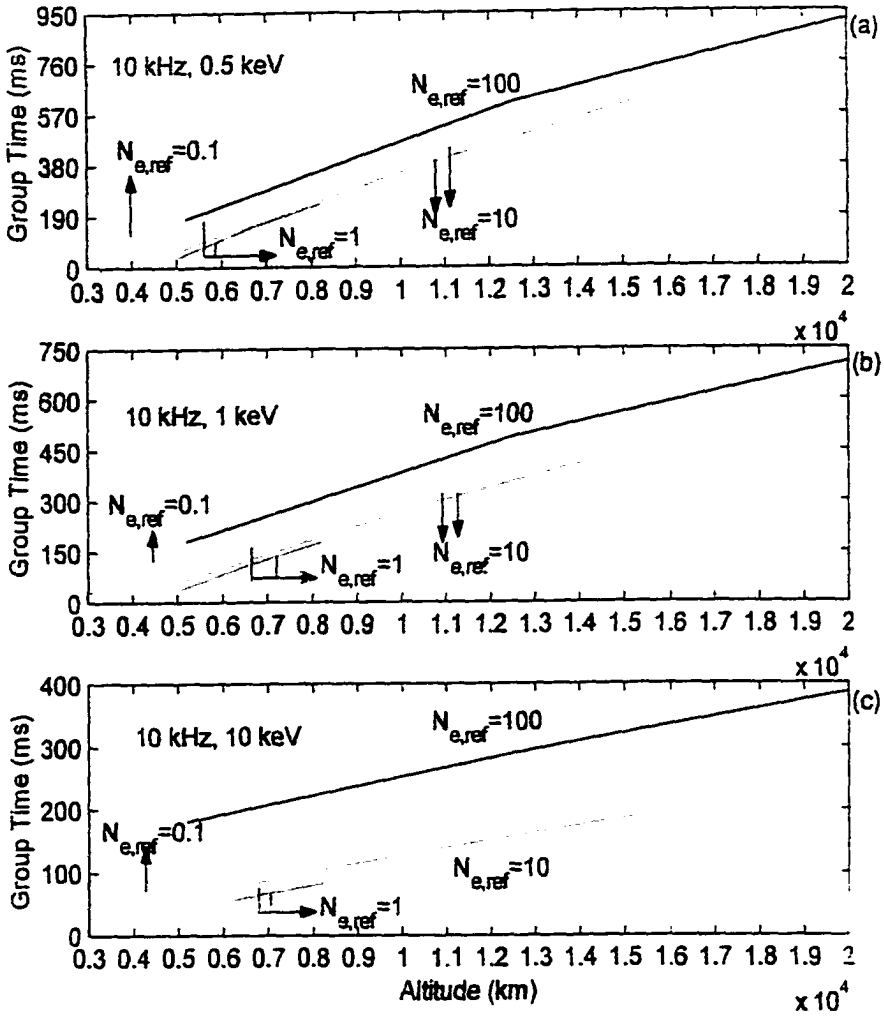

Figure 4.2.3.7. Group time (t_g) of a 10 kHz wave as a function of altitude for different density models and electron parallel resonance energies. The solid lines indicate the group time taken by the wave to scatter from meter-scale irregularities located at 5000 km altitude while the dotted lines indicate the group time taken by the wave to scatter from meter-scale irregularities located at 3000 km altitude. (a) $E_{\parallel} = 0.5$ keV; (b) $E_{\parallel} = 1$ keV; (c) $E_{\parallel} = 10$ keV.

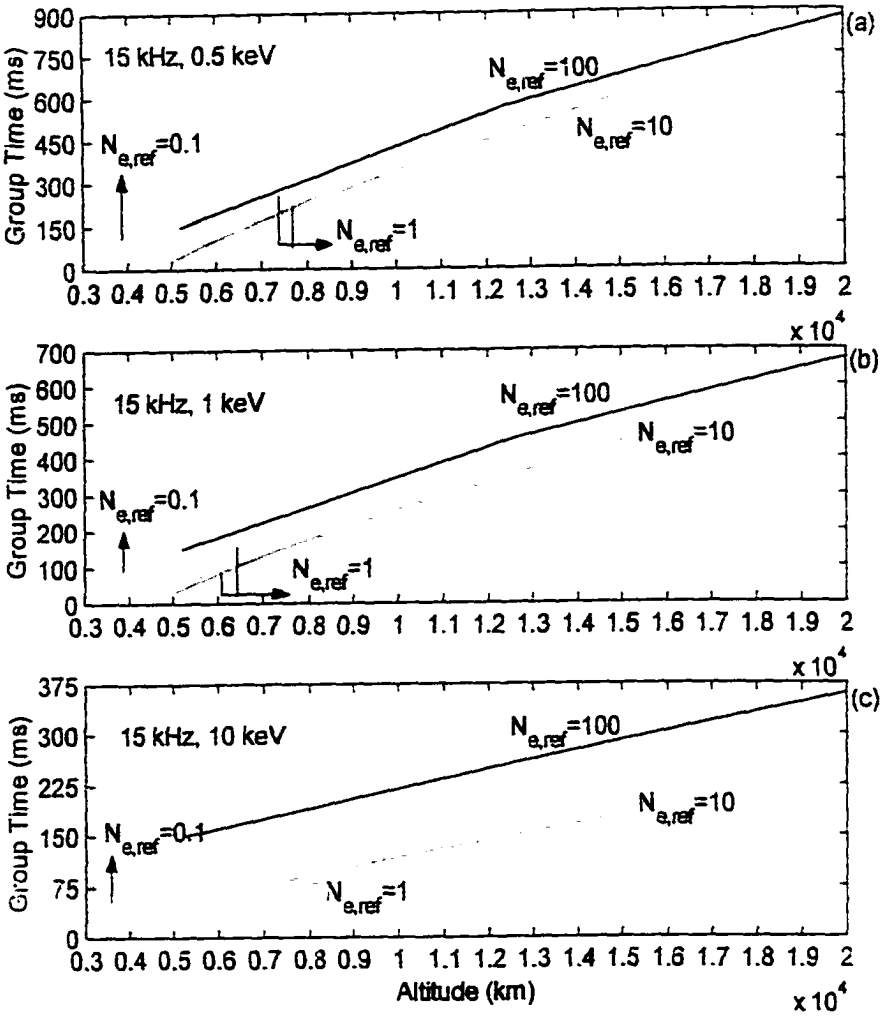

Figure 4.2.3.8. Group time (t_g) of a 15 kHz wave as a function of altitude for different density models and electron parallel resonance energies. The solid lines indicate the group time taken by the wave to scatter from meter-scale irregularities located at 5000 km altitude while the dotted lines indicate the group time taken by the wave to scatter from meter-scale irregularities located at 3000 km altitude. (a) $E_{\|} = 0.5$ keV; (b) $E_{\|} = 1$ keV; (c) $E_{\|} = 10$ keV.

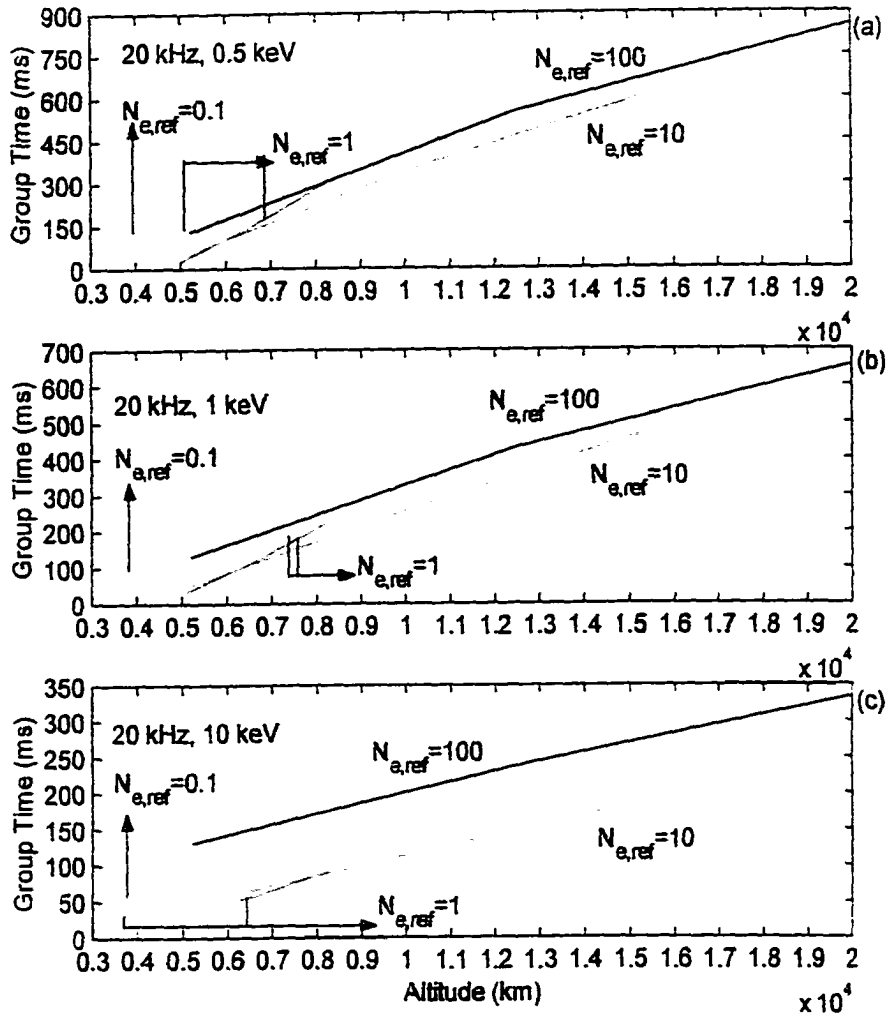

Figure 4.2.3.9. Group time (t_g) of a 20 kHz wave as a function of altitude for different density models and electron parallel resonance energies. The solid lines indicate the group time taken by the wave to scatter from meter-scale irregularities located at 5000 km altitude while the dotted lines indicate the group time taken by the wave to scatter from meter-scale irregularities located at 3000 km altitude. (a) $E_{\|} = 0.5$ keV; (b) $E_{\|} = 1$ keV; (c) $E_{\|} = 10$ keV.

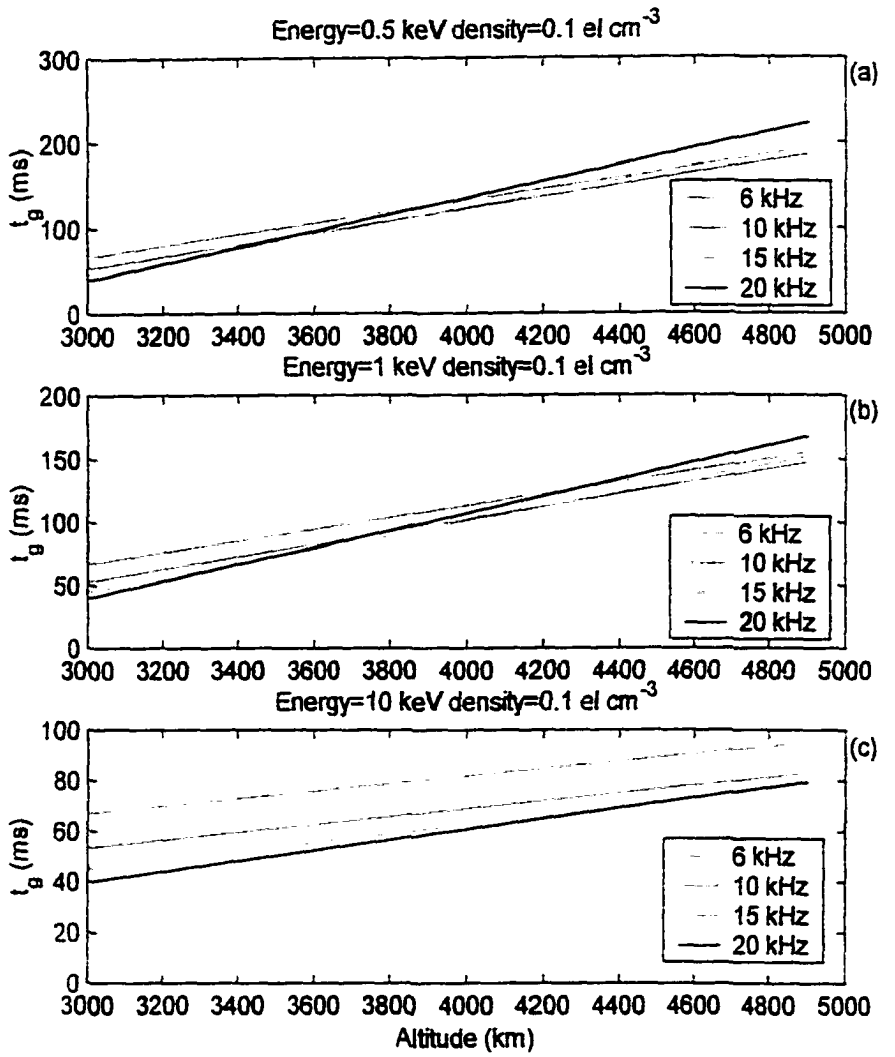

Figure 4.2.3.10. Comparison of the group time (t_g) between 6, 10, 15, and 20 kHz waves scattered from meter-scale irregularities located 5000 km altitude. $N_{e,ref} = 0.1$ el cm^{-3} at altitude= $2R_E$ and $\Lambda = 79°$. (a) $E_\parallel = 0.5$ keV; (b) $E_\parallel = 1$ keV; (c) $E_\parallel = 10$ keV. t_g is comparable between frequencies generated at the same altitude.

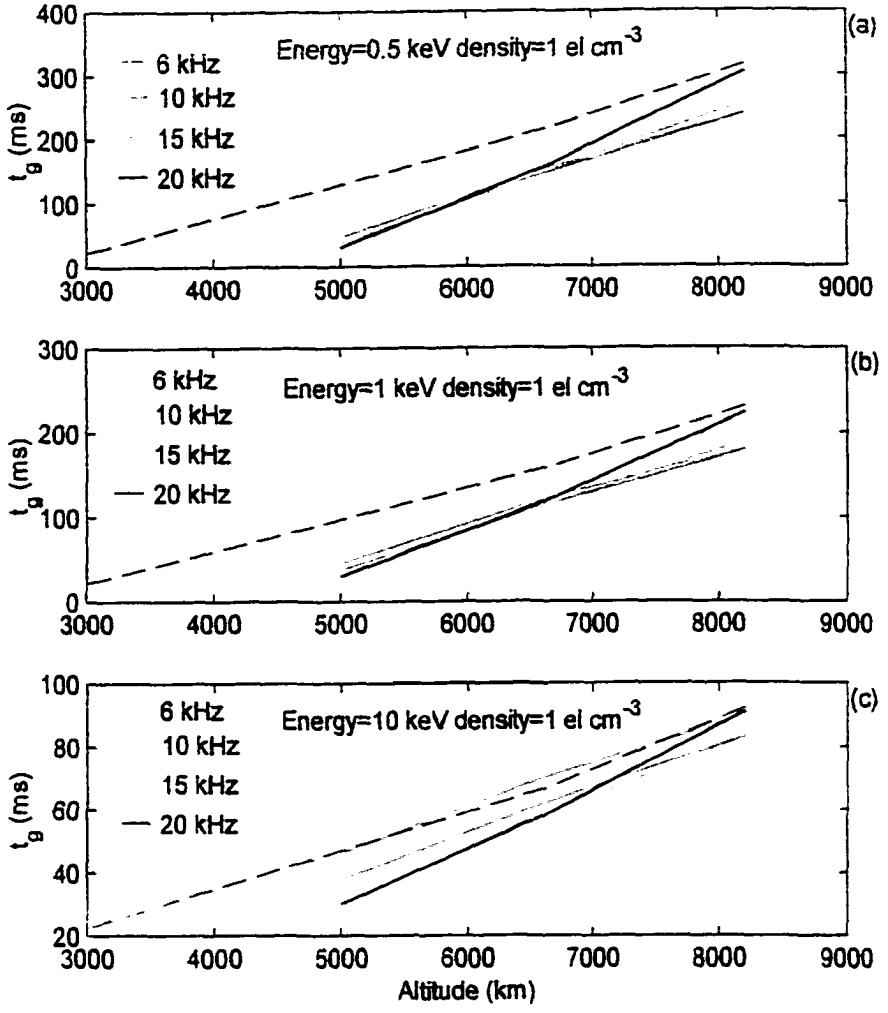

Figure 4.2.3.11. Comparison of the group time (t_g) between 6, 10, 15, and 20 kHz waves scattered from meter-scale irregularities located 5000 km (solid lines) and 3000 km (dashed lines) altitude. $N_{e,ref} = 1$ el cm^{-3} at altitude$= 2R_E$ and $\Lambda = 79°$. (a) $E_{\|} = 0.5$ keV; (b) $E_{\|} = 1$ keV; (c) $E_{\|} = 10$ keV. t_g is comparable between frequencies generated at the same high altitude and scattered from the same low altitude.

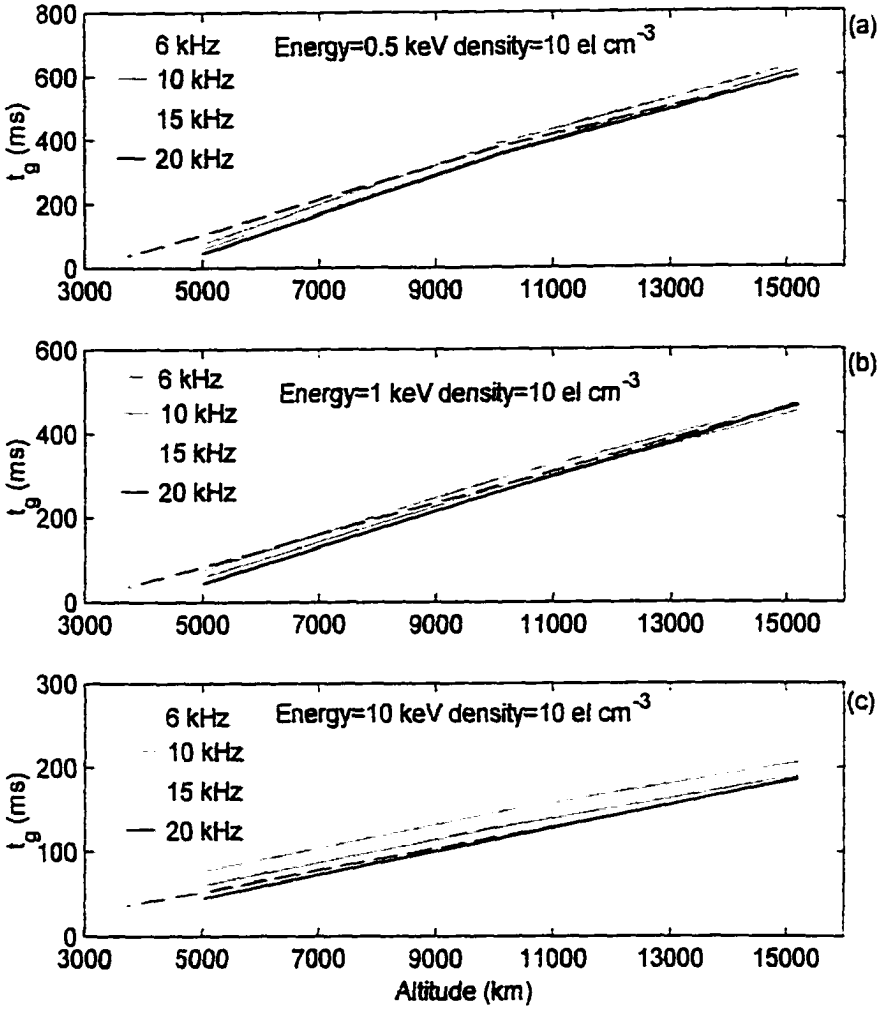

Figure 4.2.3.12. Comparison of the group time (t_g) between 6, 10, 15, and 20 kHz waves scattered from meter-scale irregularities located 5000 km (solid lines) and 3000 km (dashed lines) altitude. $N_{e,ref}$ = 10 el cm^{-3} at altitude= $2R_E$ and $\Lambda = 79°$. (a) $E_{\|}$ = 0.5 keV; (b) $E_{\|}$ = 1 keV; (c) $E_{\|}$ = 10 keV. For any given frequency, t_g is practically independent of the location of meter-scale irregularities. Additionally, t_g is comparable between frequencies generated at the same altitude.

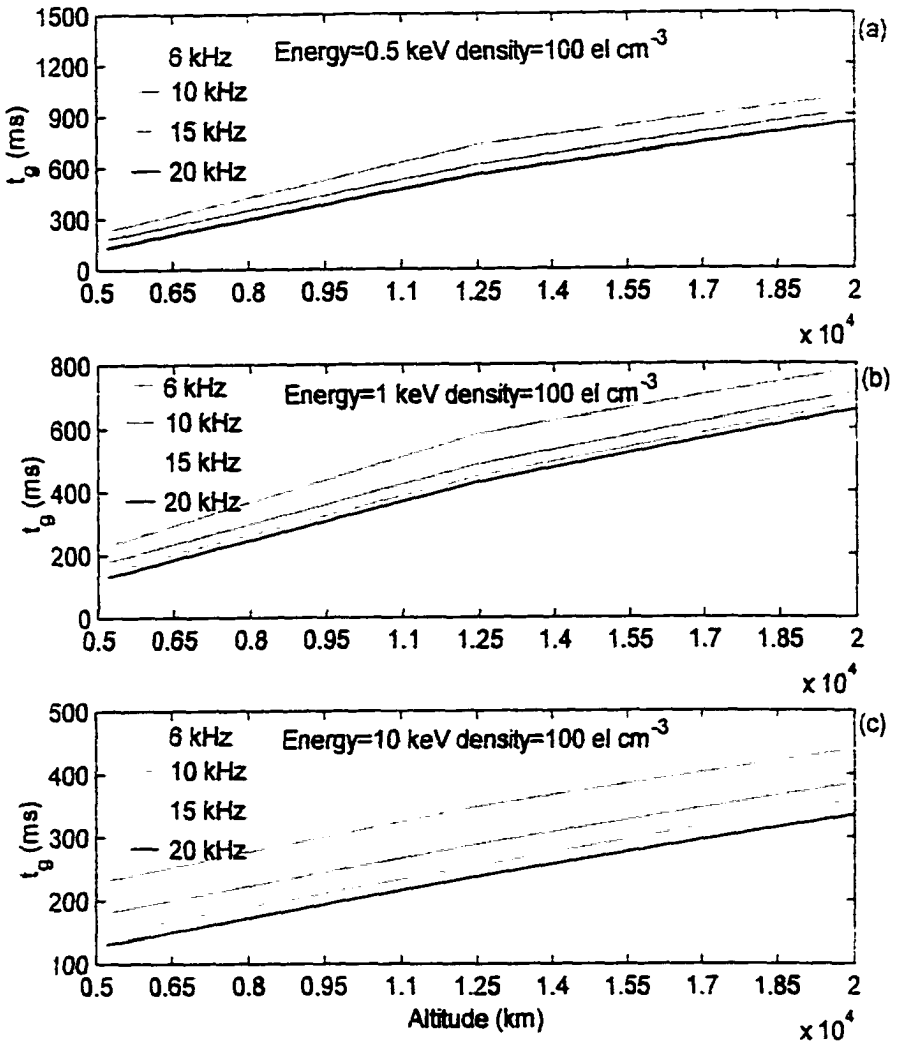

Figure 4.2.3.13. Comparison of the group time (t_g) between 6, 10, 15, and 20 kHz waves propagating from high altitudes to $\sim$ 5000 km altitude. $N_{e,ref} = 100$ el cm^{-3} at altitude$= 2R_E$ and $\Lambda = 79°$. (a) $E_{\|} = 0.5$ keV; (b) $E_{\|} = 1$ keV; (c) $E_{\|} = 10$ keV. t_g is comparable but distinct between frequencies generated at the same altitude. High frequency waves propagate faster than low frequency waves.

Figure 4.2.3.11 compares the t_g of 6. 10. 15. and 20 kHz waves as a function of altitude for $N_{e,ref}$ = 1 el cm^{-3}. The group time for the different frequency waves to reach meter-scale irregularities at 3000 km altitude is distinct but within 10 ms of each other up to ~ 6500 km. However. t_g for the same set of waves is not distinct when the waves scatter from meter-scale irregularities at 5000 km altitude. The t_g for the different frequency waves are comparable while the altitudes at which they scatter seems to categorize them into 2 groups that is ~ 100 and ~ 30 ms apart at 5000 and 8200 km altitude respectively. The difference in t_g between the 2 groups of waves decreases as $E_{||}$ increases and for $E_{||}$ = 10 keV the t_g for both groups of waves are comparable and within 15 ms of each other. Figure 4.2.3.12 compares the t_g of 6. 10. 15. and 20 kHz waves as a function of altitude for $N_{e,ref}$ = 10 el cm^{-3}. From Figure 4.2.3.12 it can be inferred that. as the local plasma density increases the difference in t_g between the 2 groups of waves decreases. For high parallel resonant energies and high local electron densities the group distinction is lost and the time taken by a wave to reach the ground from high source altitudes by scattering from either 5000 or 3000 km altitude meter-scale irregularities is comparable. Figure 4.2.3.13 compares the t_g of 6. 10. 15. and 20 kHz waves as a function of altitude for $N_{e,ref}$ = 100 el cm^{-3}. Scattering from meter-scale irregularities at 3000 km is not considered in this figure as 6 kHz waves are reflected ($f < f_{LHR}$) at ~ 5200 km altitude. The t_g for the different frequency waves are distinct but within 100 ms of each other for $E_{||}$ = 0.5. 1. and 10 keV. Additionally for all the three cases of $E_{||}$ considered in Figure 4.2.3.13. $t_g(f = 6) > t_g(f = 10) > t_g(f = 15) > t_g(f = 20)$.

4.2.4 Discussion of Results From Ray-Tracing Simulations

Figures 4.2.3.6 through 4.2.3.13 clearly show that to invert the data to find the source altitude of auroral hiss from the dispersion data is complex and may not be possible in many cases. Data can be inverted for the following cases. Suppose. as in the data used for this thesis. the receiving station was at L=27.47 or $\Lambda = 79°$ and the LAH spectra showed dispersion in the order of ~ 1 second. The data recorded in the spectrogram can include frequencies that traveled along L shells between 19.8 and 40.8. From Figures 4.2.3.6 through 4.2.3.13 it is clear

that if the frequencies are generated at the same altitude their group times are comparable and dispersion in the order of a second is not possible. Therefore the frequency waves showing a dispersion of 1 second or more must have different source altitudes. Also the low frequency wave has to be generated at high ($\sim$ 16.000 km and above) altitudes. with $E_{||} < 1$ keV to have a $t_g \approx 1$. Once the source region of the low frequency wave is determined the source region of the high frequency wave can be determined from Figures similar to 4.2.3.9. for example. From the source region of the frequencies. $E_{||}$ can be determined either from figures similar to Figure 4.2.3.6 or from figures similar to Figure 2.4.4. By way of an example. this procedure is discussed in detail in section 4.3.

A couple of other inferences that can be made from the ray-tracing simulations in section 4.2.3 are that if t_g for any frequency (6-20 kHz) is greater than $\sim$ 300 ms. the source altitude for the frequency must be $\geq$ 5.000 km. Again. if t_g for any frequency (6-20 kHz) is less than $\sim$ 100 ms . the source altitude for the frequency is $\leq$ 8.000 km.

To determine the source altitude of frequencies observed in the IAH spectra that cannot be inferred from the discussion presented in this section. more information is needed. From Figures 4.2.3.10-4.2.3.13 it is clear that $t_{g,low\,frequency}$ is not always greater than $t_{g,high\,frequency}$. The ray-tracing simulations also showed that as frequency. f. approaches f_{pe} and/or f_H the group time is modified or affected. Since inversion of data is very closely related to all parameters that affect group time of different frequencies. in the following paragraphs the dispersion relation is analyzed in relation to the different plasma parameters that affect t_g.

At low altitudes the t_g for low frequency waves is greater than the t_g for high frequency waves. Figures 4.2.3.6. 4.2.3.7. 4.2.3.8. and 4.2.3.9 show that when waves scatter from meter-scale irregularities located at either 5000 km or 3000 km altitude. with small θ. $t_{g,lower\,frequency} > t_{g,higher\,frequency}$. However at mid and high altitudes this relationship does not always hold true. Also. as the injection altitude increases. f approaches f_{pe} and/or f_H and for large θ all three terms affect t_g. This could be one of the reasons why a high frequency wave travels slower than a low frequency wave at high altitudes. To understand the different plasma parameters that affect t_g. group velocity (v_g) (v_g is inversely proportional to t_g) is analyzed as a function of altitude. cold plasma electron

density and frequency.

The approximate dispersion relation equation for quasi electrostatic whistler waves in cold plasma [*Draganov et al.*, 1993] is

$$D(\omega, k) = -1 + \frac{\omega_{pi}^2}{\omega^2} + \frac{\omega_{pe}^2}{\omega^2} cos^2\theta - \frac{\omega_{pe}^2}{\omega_H^2} = 0 \qquad (4.2.4.1)$$

where $\cos\theta = k_{||}/k$ and $k_{||}$ is a component of the wave vector k parallel to the ambient magnetic field. ω_{pe}, ω_{pi}, and ω_H are the plasma electron, ion and electron gyro frequencies. Equation 4.2.4.1 assumes that $\omega \ll \omega_{pe}$ and $\omega \ll \omega_H$. In this thesis, the only whistler relation assumed is $f < min(f_H, f_{pe})$. As a result equation 4.2.4.1 is used to only explain those cases where the assumptions $\omega \ll \omega_{pe}$ and $\omega \ll \omega_H$ holds true. At high altitudes, assuming a cold hydrogen plasma, the equations for ray trajectory can be obtained in parametric form [*Draganov et al.*, 1993] as $\overline{k} = \overline{k}(\tau)$, $\overline{r} = \overline{r}(\tau)$, $t = t(\tau)$ by differentiating the function $D(\omega, \overline{k})$:

$$\frac{d\overline{k}}{d\tau} = \frac{\partial D(\omega, \overline{k})}{\partial \overline{r}} \qquad (4.2.4.2)$$

$$\frac{d\overline{r}}{d\tau} = -\frac{\partial D(\omega, \overline{k})}{\partial \overline{k}} \qquad (4.2.4.3)$$

$$\frac{dt}{d\tau} = \frac{\partial D(\omega, \overline{k})}{\partial \overline{\omega}} \qquad (4.2.4.4)$$

From the above equations the group velocity v_g is:

$$v_g = \frac{dr}{dt} = \frac{dr}{d\tau}\frac{d\tau}{dt} \qquad (4.2.4.5)$$

where r is the radial distance and τ is a parameter. In terms of parallel and perpendicular components

$$v_{g\perp} = \frac{dr_\perp}{dt} = \frac{dr_\perp}{d\tau}\,\frac{d\tau}{dt} \tag{4.2.4.6}$$

$$v_{g\parallel} = \frac{dr_\parallel}{dt} = \frac{dr_\parallel}{d\tau}\,\frac{d\tau}{dt} \tag{4.2.4.7}$$

From *Draganov et al.*, [1993]

$$\frac{dt}{d\tau} = \frac{\partial D(\omega,k)}{\partial\omega} = \frac{-2}{\omega}(1+\frac{\omega_{pe}^2}{\omega_H^2}) \tag{4.2.4.8}$$

$$\frac{dr}{d\tau} = \frac{-\partial D(\omega,k)}{\partial k} \tag{4.2.4.9}$$

Using equations 4.2.4.1, 4.2.4.8, and 4.2.4.9

$$v_{g\perp} = -\frac{(k_\parallel^2)(k_\perp)}{\omega k^4}(\frac{1}{\frac{1}{\omega_{pe}^2}+\frac{1}{\omega_H^2}}) \tag{4.2.4.10}$$

$$v_{g\parallel} = \frac{(k_\parallel)(k_\perp^2)}{\omega k^4}(\frac{1}{\frac{1}{\omega_{pe}^2}+\frac{1}{\omega_H^2}}) \tag{4.2.4.11}$$

$$v_g = \frac{(k_\parallel)(k_\perp)}{\omega k^3}(\frac{1}{\frac{1}{\omega_{pe}^2}+\frac{1}{\omega_H^2}}) \tag{4.2.4.12}$$

or

$$v_g = \frac{cos\theta\ sin\theta}{\omega k}(\frac{1}{\frac{1}{\omega_{pe}^2}+\frac{1}{\omega_H^2}}) = \frac{sin2\theta}{2\omega k}(\frac{\omega_H^2\,\omega_{pe}^2}{\omega_H^2+\omega_{pe}^2}) \tag{4.2.4.13}$$

Equation 4.2.4.13 shows that v_g is a function of f_{pe}, f_H, $\sin(2\theta)$, and $E_\parallel$ (equation 2.3.2). In the magnetosphere f_{pe} and f_H decrease with altitude (Figure 3.2.4). For a given altitude and frequency, θ_R decreases with altitude as θ_R

decreases with decreasing background electron density. However, v_g depends on $\sin 2\theta$ which approaches 0 as θ_R approaches 0° or 90°. For quasi-electrostatic whistler wave propagation, calculations show that $(\theta_R - \theta) \leq 1.3°$ for $N_{e,ref} = 0.1, 1, 10$ el cm^{-3} and $E_{\|} \leq 15°$. This implies that at low altitudes, the high values for v_g from high f_H and f_{pe} could be offset by low values for $\sin 2\theta$ for $0 < \theta_R < 15°$ or $75° < \theta_R < 90°$. Similarly, at high altitudes a high value of $\sin 2\theta$ can offset the reduced value of f_{pe}. For $N_{e,ref} = 100$ el cm^{-3} and $E_{\|} \leq 15°$, $\theta_R - \theta \leq 5.4°$ for altitudes up to 15,000 km and $\theta_R - \theta \leq 13°$ for altitudes up to 20,000.

Figure 4.2.4.1a compares v_g as a function of $(\theta_R - \theta)$ at 3000 km altitude for different frequencies and density models. 6, 10, 15, and 20 kHz waves are represented by red, blue, green and black lines respectively. The dotted lines represent v_g computed using equation 4.2.4.13 and the solid lines are the exact values of v_g obtained using the ray-tracing program. For a given frequency Figure 4.2.4.1b compares v_g as a function of $(\theta_R - \theta)$ at 3000 km altitude. Similarly Figures 4.2.4.2, 4.2.4.3, 4.2.4.4, 4.2.4.5, 4.2.4.6, and 4.2.4.7 compare v_g as a function of $(\theta_R - \theta)$ at 5000, 7000, 10,000, 12,000, 15,000, and 20,000 km altitude respectively. For a given f_H (f_H is a function of altitude) and f_{pe}, v_g decreases as the frequency increases, as shown in equation 4.2.4.13, except at 3000 km altitude and $N_{e,ref} = 100$ el cm^{-3}. At 3000 km altitude and $N_{e,ref} = 100$ el cm^{-3}, θ_R for a 15 kHz wave is 88.9° while θ_R for a 20 kHz wave is 88.1°. As discussed in the previous paragraph the difference in $\sin 2\theta$ ($\sin(2*88.9)=0.04$, $\sin(2*88.1)=0.07$) is marginal and insufficient to offset the difference in v_g for different frequencies and we have $v_g(20 \text{ kHz}) \approx 1.3\ v_g(15 \text{ kHz})$. For low density models (eg $N_{e,ref} = 1$ el cm^{-3}) when $f \approx f_{pe}$, equation 4.2.4.13 fails. For high density models (eg $N_{e,ref} = 100$ el cm^{-3}), $(\theta_R - \theta) \approx 13°$ and v_g computed using equation 4.2.4.13 is not a good approximation. Also at high altitudes, for $f \approx f_{pe}$ or $f \approx f_H$ equation 4.2.4.13 fails.

From equation 2.3.2, $E_{\|}$ increases as θ increases and decreases as μ increases. However, as θ moves towards θ_R the refractive index μ approaches infinity. As the product of μ and $cos\theta$ determine $E_{\|}$, at some altitudes, there are specific values of $E_{\|}$ that cannot exist.

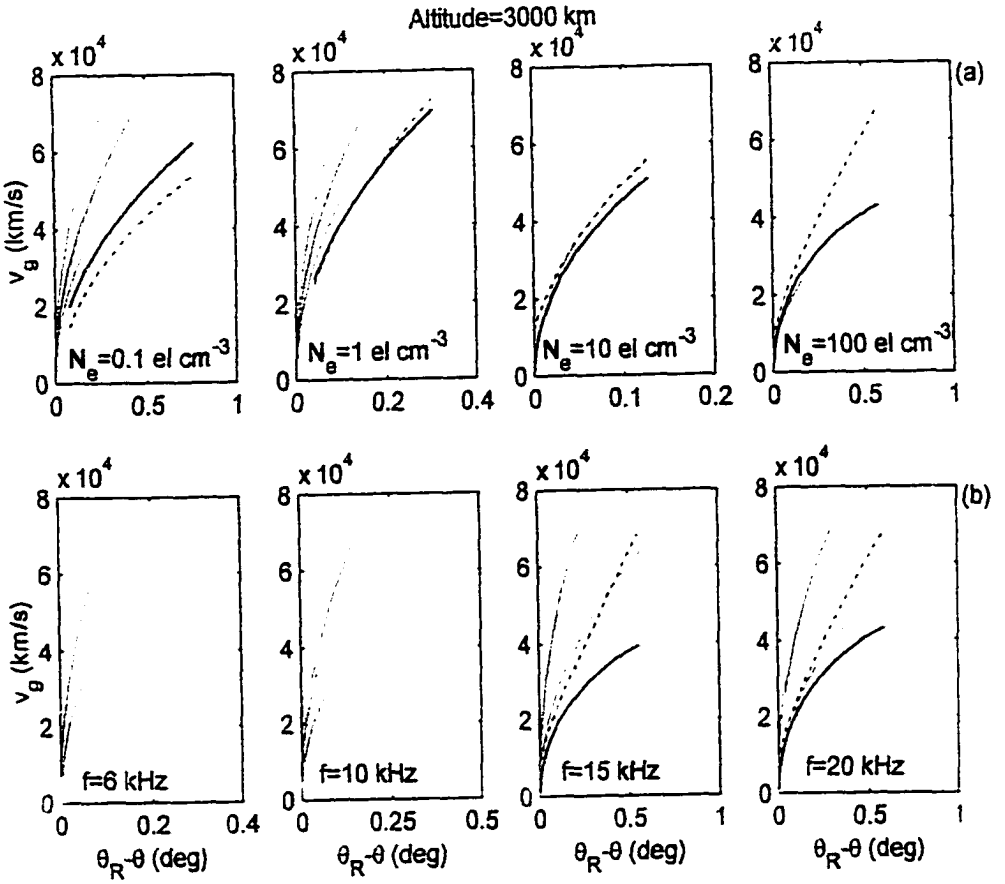

Figure 4.2.4.1 For a given altitude of 3000 km, comparison of group velocity (v_g) as a function of $\theta_R - \theta$ for different density models. (a) v_g for 6, 10, 15, and 20 kHz waves are compared with each other for different density models. The 6, 10, 15, and 20 kHz waves are represented by red, blue, green, and black lines respectively. The solid lines are the v_g computed from the ray path parameters while the dotted lines are the v_g computed using the approximation from *Draganov et al.* [1993] paper. (b) For a given frequency and altitude of 3000 km, plots to show variance in v_g as the background electron density or local f_{pe} changes. Red, blue, green, and black lines represent $N_{e,ref} = 0.1, 1, 10, 100$ el cm^{-3} density models respectively. The maximum θ selected for each frequency is such that $E_{\|} = 15$ keV. For $N_{e,ref} = 100$ el cm^{-3} and f=20 kHz, at 3000 km $E_{\|,max} = 10$ keV.

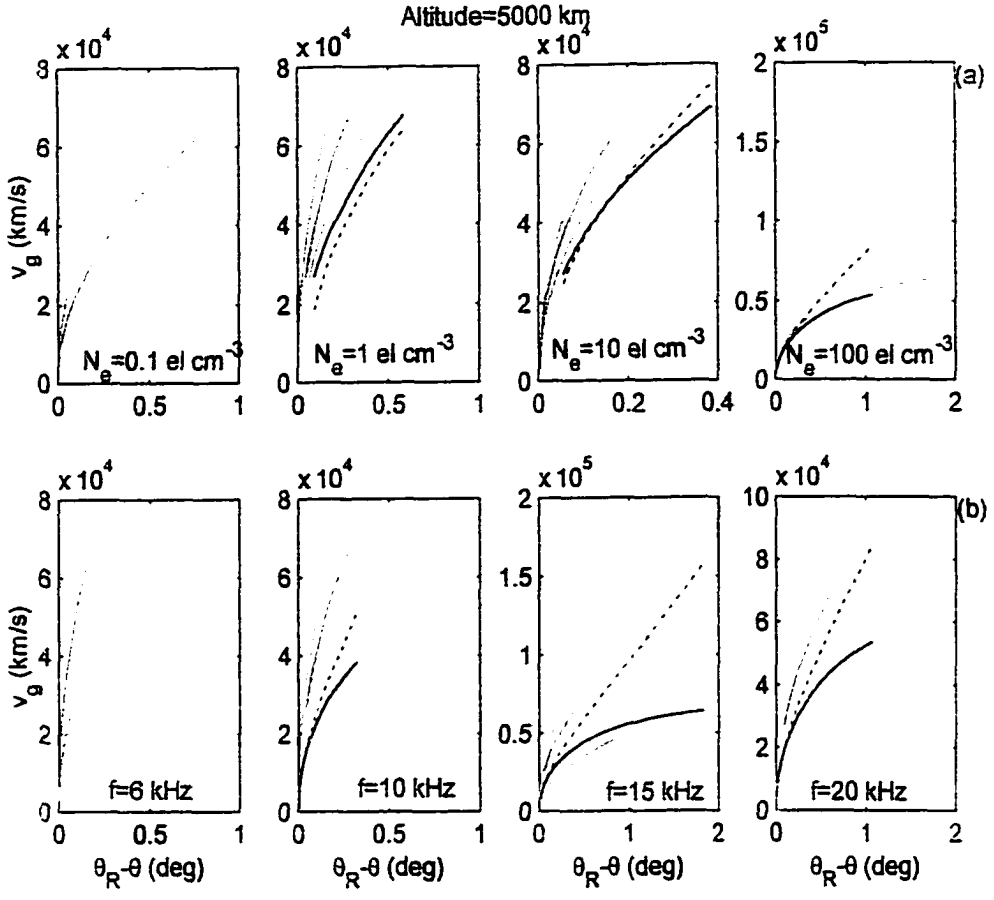

Figure 4.2.4.2. For a given altitude of 5000 km, comparison of group velocity (v_g) as a function of $\theta_R - \theta$ for different density models. (a) v_g for 6, 10, 15, and 20 kHz waves are compared with each other for different density models. The 6, 10, 15, and 20 kHz waves are represented by red, blue, green, and black lines respectively. The solid lines are the v_g computed from the ray path parameters while the dotted lines are the v_g computed using the approximation from *Draganov et al.* [1993] paper. (b) For a given frequency and altitude of 5000 km, plots to show variance in v_g as the background electron density or local f_{pe} changes. Red, blue, green, and black lines represent $N_{e,ref} = 0.1, 1, 10, 100$ el cm^{-3} density models respectively. The maximum θ selected for each frequency is such that $E_{\|} = 15$ keV. For $N_{e,ref} = 100$ el cm^{-3} $E_{\|,max} = 10$ keV for f=10 and 20 kHz waves.

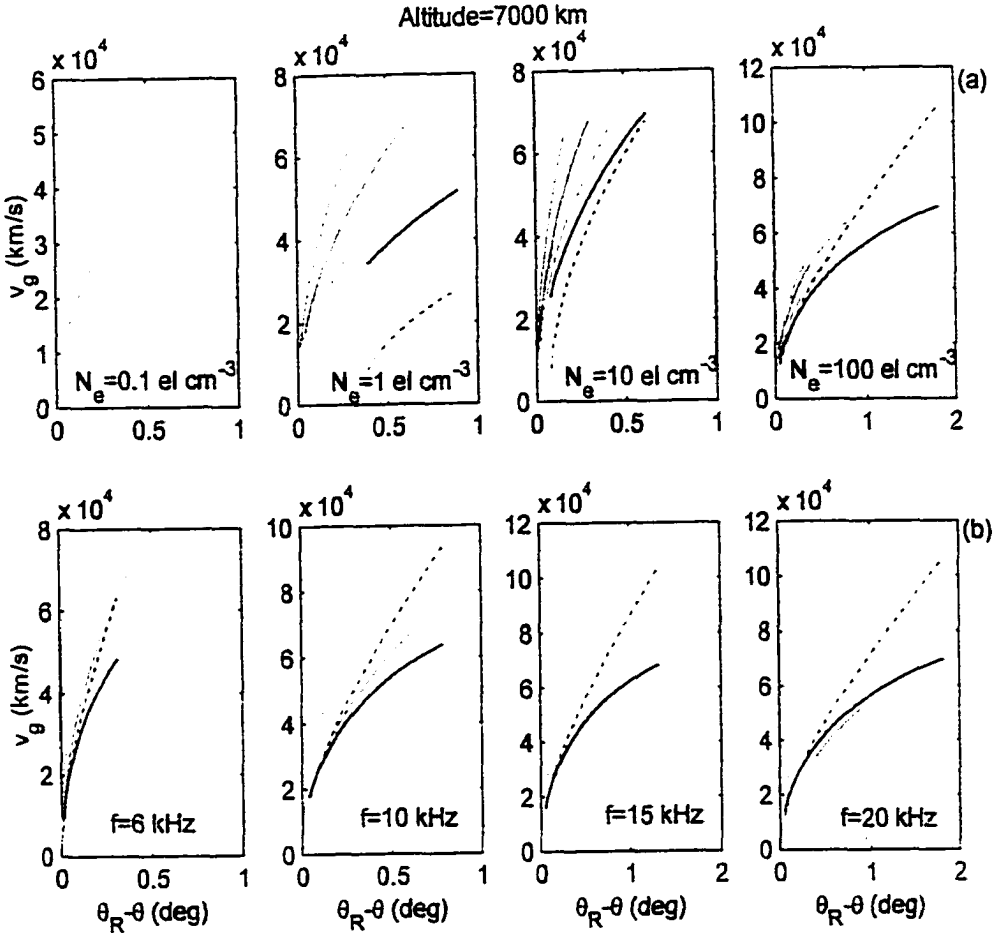

Figure 4.2.4.3. For a given altitude of 7000 km, comparison of group velocity (v_g) as a function of $\theta_R - \theta$ for different density models. (a) v_g for 6, 10, 15, and 20 kHz waves are compared with each other for different density models. The 6, 10, 15, and 20 kHz waves are represented by red, blue, green, and black lines respectively. The solid lines are the v_g computed from the ray path parameters while the dotted lines are the v_g computed using the approximation from *Draganov et al.* [1993] paper. (b) For a given frequency and altitude of 7000 km, plots to show variance in v_g as the background electron density or local f_{pe} changes. Red, blue, green, and black lines represent $N_{e,ref} = 0.1, 1, 10, 100$ el cm^{-3} density models respectively. The maximum θ selected for each frequency is such that $E_{\|} = 15$ keV.

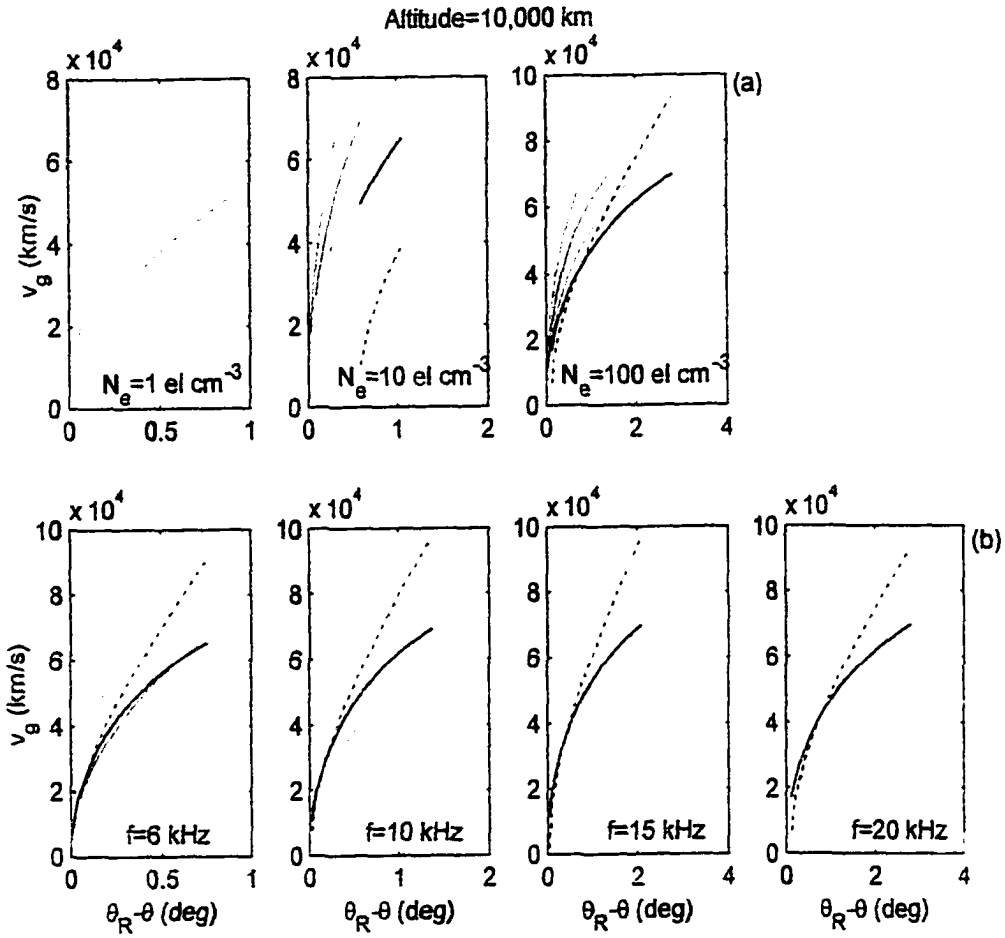

Figure 4.2.4.4. For a given altitude of 10,000 km, comparison of group velocity (v_g) as a function of $\theta_R - \theta$ for different density models. (a) v_g for 6, 10, 15, and 20 kHz waves are compared with each other for different density models. The 6, 10, 15, and 20 kHz waves are represented by red, blue, green, and black lines respectively. The solid lines are the v_g computed from the ray path parameters while the dotted lines are the v_g computed using the approximation from *Draganov et al.* [1993] paper. (b) For a given frequency and altitude of 10,000 km, plots to show variance in v_g as the background electron density or local f_{pe} changes. Red, blue, green, and black lines represent $N_{e,ref} = 0.1, 1, 10, 100$ el cm^{-3} density models respectively. The maximum θ selected for each frequency is such that $E_{\parallel} = 15$ keV.

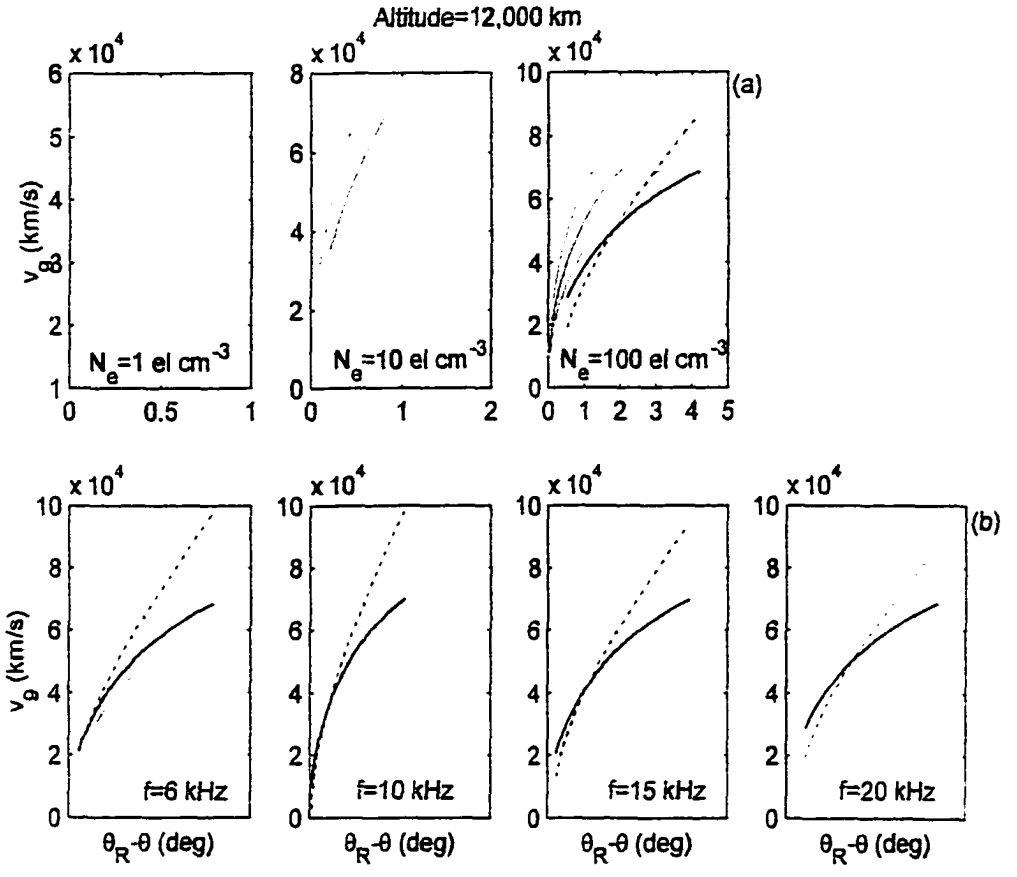

Figure 4.2.4.5. For a given altitude of 12,000 km, comparison of group velocity (v_g) as a function of $\theta_R - \theta$ for different density models. (a) v_g for 6, 10, 15, and 20 kHz waves are compared with each other for different density models. The 6, 10, 15, and 20 kHz waves are represented by red, blue, green, and black lines respectively. The solid lines are the v_g computed from the ray path parameters while the dotted lines are the v_g computed using the approximation from *Draganov et al.* [1993] paper. (b) For a given frequency and altitude of 12,000 km, plots to show variance in v_g as the background electron density or local f_{pe} changes. Red, blue, green, and black lines represent $N_{e,ref} = 0.1, 1, 10, 100$ el cm^{-3} density models respectively. The maximum θ selected for each frequency is such that $E_{\parallel} = 15$ keV. When f is comparable to either f_{pe} or f_H the v_g approximation from *Draganov et al.* [1993] paper fails and is not shown in the plots. Please refer to the text for details.

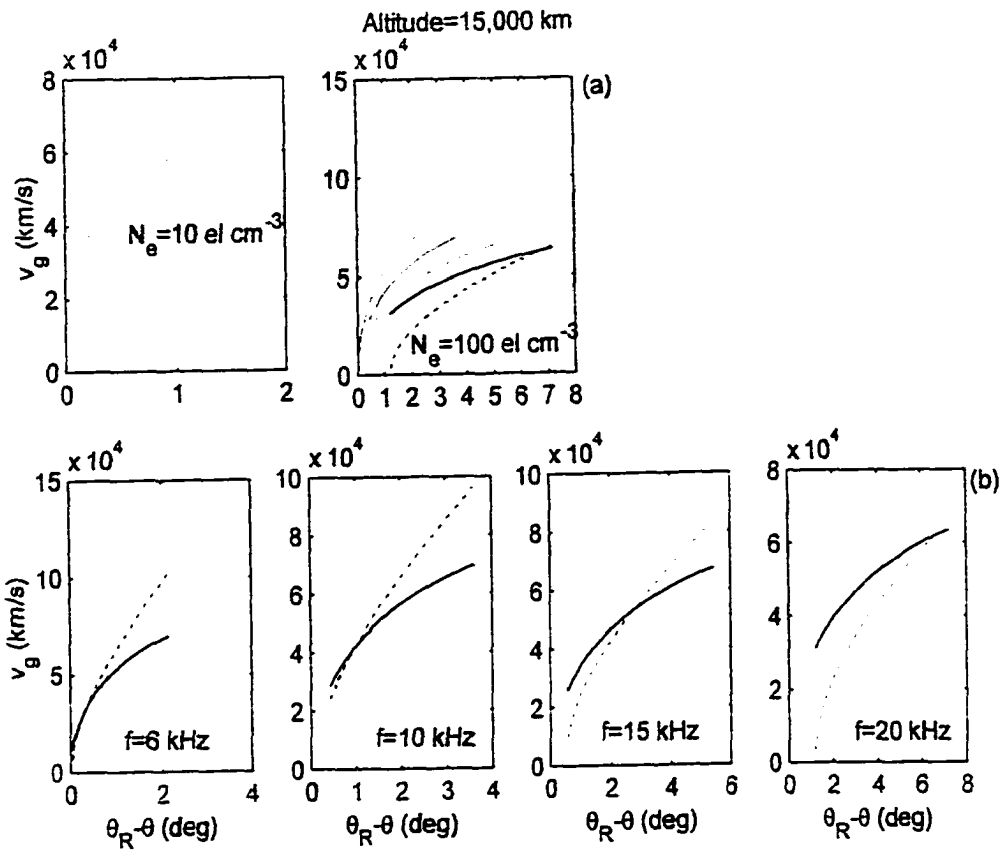

Figure 4.2.4.6. For a given altitude of 15,000 km, comparison of group velocity (v_g) as a function of $\theta_R - \theta$ for different density models. (a) v_g for 6, 10, 15, and 20 kHz waves are compared with each other for different density models. The 6, 10, 15, and 20 kHz waves are represented by red, blue, green, and black lines respectively. The solid lines are the v_g computed from the ray path parameters while the dotted lines are the v_g computed using the approximation from *Draganov et al.* [1993] paper. (b) For a given frequency and altitude of 15,000 km, plots to show variance in v_g as the background electron density or local f_{pe} changes. Red, blue, green, and black lines represent $N_{e,ref} = 0.1, 1, 10, 100$ el cm^{-3} density models respectively. The maximum θ selected for each frequency is such that $E_{\|} = 15$ keV. When f is comparable to either f_{pe} or f_H the v_g approximation from *Draganov et al.* [1993] paper fails and is not shown in the plots. Please refer to the text for details.

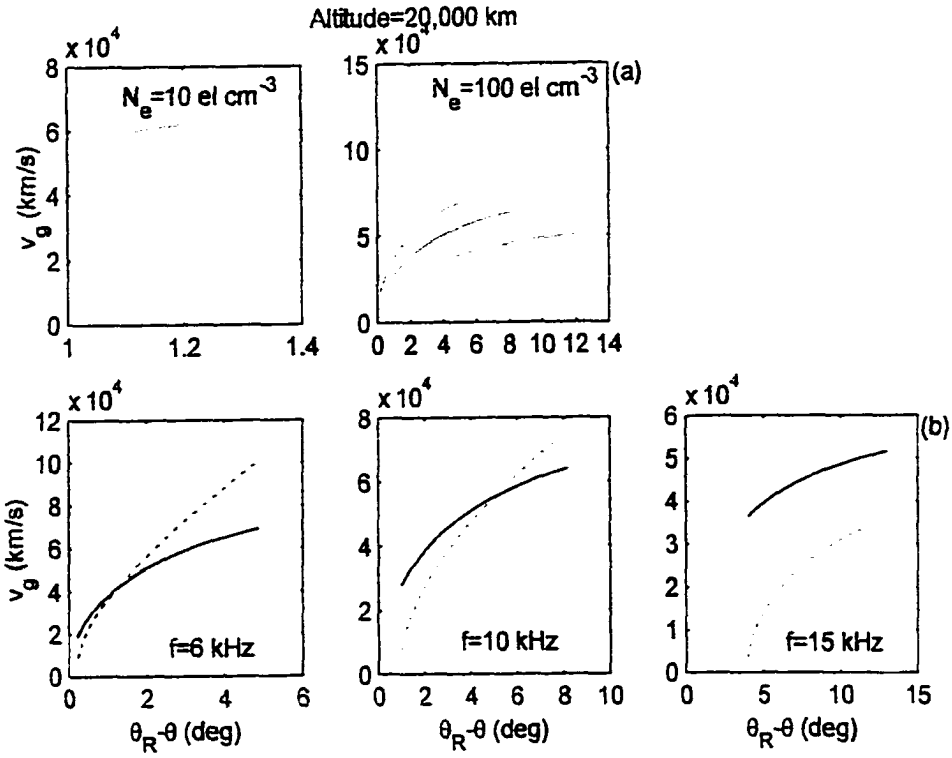

Figure 4.2.4.7. For a given altitude of 20,000 km, comparison of group velocity (v_g) as a function of $\theta_R - \theta$ for different density models. (a) v_g for 6, 10, 15, and 20 kHz waves are compared with each other for different density models. The 6, 10, 15, and 20 kHz waves are represented by red, blue, green, and black lines respectively. The solid lines are the v_g computed from the ray path parameters while the dotted lines are the v_g computed using the approximation from *Draganov et al.* [1993] paper. (b) For a given frequency and altitude of 20,000 km, plots to show variance in v_g as the background electron density or local f_{pe} changes. Red, blue, green, and black lines represent $N_{e,ref} = 0.1, 1, 10, 100$ el cm^{-3} density models respectively. The maximum θ selected for each frequency is such that $E_{\|} = 15$ keV. For $N_{e,ref} = 100$ el cm^{-3} $E_{\|,max} = 10$ keV for f=20 kHz waves. When f is comparable to either f_{pe} or f_H the v_g approximation from *Draganov et al.* [1993] paper fails and is not shown in the plots. Please refer to the text for details.

For example, at 5000 km altitude, if the local $f_H = 302$ kHz and the local $f_{pe} = 608$ kHz ($N_{e,ref} = 100$ el cm^{-3}), then any 10 kHz wave generated at this altitude has $E_{\|} < 15$ keV. The $\theta_R - \theta$ dependence of v_g and hence t_g shown in Figures 4.2.4.1 through 4.2.4.7 is a function of f_{pe}, f_H and frequency f. For a given altitude, frequency and $E_{\|}$, θ can be further away from θ_R for high densities except when $f \approx f_{pe}$ or $f \approx f_H$. For a given density model, frequency and $E_{\|}$, as the injection altitude increases the initial θ can be injected further away from θ_R, except for $f \approx f_{pe}$ or $f \approx f_H$. Finally, for a given altitude, density model and $E_{\|}$, $\theta_R - \theta$ is smaller for smaller frequencies provided $f \not\approx f_{pe}$ and $f \not\approx f_H$. The $\theta_R - \theta$ dependence can be qualitatively explained as follows.

From the dispersion relation [*Stix*, 1992],

$$\tan^2\theta = \frac{-P(n^2 - R)(n^2 - L)}{(Sn^2 - RL)(n^2 - P)} \qquad (4.2.4.14)$$

where for particles of type s, $P = 1 - \sum_s \frac{\omega_{ps}^2}{\omega^2}$, $R = 1 - \sum_s \frac{\omega_{ps}^2}{\omega(\omega+\omega_{cs})}$, $L = 1 - \sum_s \frac{\omega_{ps}^2}{\omega(\omega-\omega_{cs})}$, and $S = 0.5(R + L)$:

For ($f_{pe} \gg f_H$) and $\theta \approx \theta_R$

$$\tan^2\theta \approx \frac{\omega_H^2 - \omega^2}{\omega^2} \qquad (4.2.4.15)$$

or

$$\cos\theta \approx f/f_H \qquad (4.2.4.16)$$

For low frequencies the ratio f/f_H is small and thus $\cos\theta$ is small. Hence for a given altitude and electron energy $E_{\|}$, the μ required to satisfy equation 2.3.2 is large and this requires θ to be closer to θ_R for smaller frequencies.

For ($f_{pe} \ll f_H$) and $\theta \approx \theta_R$

$$\tan^2\theta \approx \frac{\omega_{pe}^2 - \omega^2}{\omega^2} \qquad (4.2.4.17)$$

or

$$\cos\theta \approx f/f_{pe} \tag{4.2.4.18}$$

For low frequencies the ratio f/f_{pe} is small and thus $\cos\theta$ is small. Hence for a given density model and electron energy $E_{\|}$, the μ required to satisfy equation 2.3.2 is large and this requires θ to be closer to θ_R for smaller frequencies.

For ($f \approx f_{pe} \approx f_H$) and $\theta \approx \theta_R$

$$\tan^2\theta = -1 + \frac{\omega_{pe}^2\omega_H^2}{\omega^2(\omega_{pe}^2 + \omega_H^2 - \omega^2)} \tag{4.2.4.19}$$

or

$$\cos\theta = \frac{f}{f_{pe}f_H}(f_{pe}^2 + f_H^2 - f^2)^{1/2} \tag{4.2.4.20}$$

For ($f \approx f_{pe} \approx f_H$), θ is a function of f, f_{pe}, and f_H. f is less than f_H and f_{pe} for whistler waves. Hence when f approaches f_H or f_{pe} (the smaller of the 2 frequencies), $\cos\theta$ approaches 1 irrespective of the other plasma frequency. For example, at high altitudes (eg. 20,000 km) f_H for a low density model ($N_{e,ref}$ = 10 el cm^{-3}) is approximately 23 kHz and f_{pe} is 11.7 kHz. A 10 kHz wave for these plasma parameters has an initial θ closer to θ_R compared to a 6 kHz wave.

Based on the analysis of the dispersion equation and the ray-tracing simulations it is clear that if the observed frequency is close to the local f_{pe} or f_H, t_g is affected and the spectra may show hiss events where the low frequency wave travels faster than the high frequency wave giving rise to parabolic shapes in the IAH spectra (events marked A and B in Figure 4.2.1.2a).

4.3 Determination of Auroral Field Lines, Auroral Hiss Source Region, Cold Plasma Electron Density, and Energetic Electron Parallel Resonance Energy From Auroral Hiss Observations

In this section, the model proposed in this thesis is used to determine the AH source region, $E_{\parallel}$ and cold plasma electron density along auroral field lines from the IAH spectra shown in Figure 4.2.1.2. The concepts and results developed throughout this thesis are also used in this section.

The sample IAH spectrogram in Figure 4.2.1.2 was recorded for 30 seconds from 0050 UT on July 09, 1996 at South Pole station. The South Pole station is located at $\Lambda = 79°$ or L=27.47. From the discussion in section 4.2.2, it is possible that the hiss events recorded in the sample IAH spectra could have traveled along $\Lambda = 79°$ or along any field line between $\Lambda = 77°$ (L=19.8) and $\Lambda = 81°$ (L=40.8). At this time, to uniquely determine the auroral field line additional data is essential. For example, if data can be obtained from a VLF direction finding system that can measure the AH exit point, the range of possible field lines along which the hiss could have propagated can be narrowed. Since additional data was not available for the spectrogram used in this example the cold plasma electron concentrations determined at the end of this section hold for a range of field lines defined by $77° \leq \Lambda \leq 81°$.

The lowest hiss frequency observed in the 30 seconds is $\sim$ 7 kHz. However, the hiss events show approximately 3 lower cutoff frequencies. The 3 lower cutoff frequencies that can be used to represent the sample data set are 7, 8, and 9 kHz. Since f_{LHR} at the highest altitude up to which meter-scale irregularities exist determines the lower cutoff frequency for AH (section 2.5), meter-scale irregularities must be present over a range ($\sim$ 3000 – 5000 km) of altitudes. This means that the AH data observed in the spectrogram could have scattered at any altitude between 3000 and 5000 km from the meter-scale irregularities. The highest hiss frequency observed on the spectrogram is $\sim$ 20 kHz. Since the spectrogram does not show any other signals in the background beyond 20 kHz, the 20 kHz limit is an artificial limit set by the receiver. Again, there is more than one upper cutoff frequency. Figure 4.2.1.2 shows hiss events with upper cutoff frequencies ranging from 12 to 20 kHz. Since f_{pe} and f_H determine the highest

altitude at which whistler waves may exist. depending on the initial density model. the different frequencies could have generated anywhere between $\sim$ 6000 and 20.000 km (Figure 4.2.3.5). It is also possible that the different field lines along which AH could have propagated have different electron concentrations.

From ray-tracing simulations. when dispersion is of the order of 1 second or more the cold plasma electron density along the field line should be high. From section 4.2.4 it is clear that when dispersion is of the order of 1 second or more AH data can be inverted to determine the AH source altitudes. $E_{\parallel}$. and consequently the cold plasma electron density along the field line. Hence. to construct an initial tentative density model hiss events that show a dispersion of 1 second or more are first considered. Table 9 lists the hiss events that show a dispersion of 1 second and more.

From section 4.2.4 and ray-tracing simulations the hiss events in Table 9 should have propagated along auroral field lines with enhanced electron concentrations. This implies that the initial cold plasma density model along the field line should have been such that $N_{e,ref} \sim 100$ el cm^{-3} at 2 R_E altitude. By saying that "the initial cold plasma density model along the field line should be such that $N_{e,ref} \sim 100$ el cm^{-3} at 2 R_E". density is not defined just at 2 R_E altitude. but along the entire field line. The density along the entire field line can be determined from density at 2 R_E altitude by using a R^{-5} collisionless density model outside the plasmasphere (section 4.2.3) and a diffusive equilibrium model within the plasmasphere (section 3.2). Since 17 of the 36 events show dispersion of 1 second and more. the electron concentration along 1 or more field lines between $77^\circ \leq \Lambda \leq 81^\circ$ is defined by $N_{e,ref} = 100$ el cm^{-3} at 2 R_E altitude.

Table 9: Hiss Events With Dispersion of one Second and More

Hiss Event	Frequencies (kHz)	Dispersion (secs)
8	14 - 7	1.5
9	13 - 9	1
12	12 - 7.5	1.1
13	14.8 - 7.5	1.4
15	16.8 - 7	1.3
16	16 - 7.5	1.2
19	14.9 - 7.5	1.5
21	18 - 6.9	1.3
22	14.5 - 8	1
23	14 - 8	1.4
24	14 - 8	1.8
27	14.9 - 6.9	1.4
28	12.5 - 8.8	1
29	20 - 6.9	1.4
30	16 - 8	1.1
31	15.2 - 8	1.4
33	14 - 8	1

In this paragraph the source altitude for the hiss events in Table 9 is discussed. A dispersion of 1 second is possible only if the low frequency wave is generated at high (> 16.000 km) altitudes by energetic electrons with $E_{\|} < 1$ keV. Additionally, since AH source altitudes are between 5000 and 20.000 km, the AH source region for some of the low frequency waves must be 16.000-20.000 km. The high frequency waves or frequencies between 12 and 20 kHz in Table 9 must have been generated by energetic electrons with $E_{\|} < 1$ keV at altitudes less than 8000 km to show a dispersion of ~ 1 second.

Initial analysis of the sample IAH spectra shows that some AH with frequencies between 12 and 20 kHz were generated at high altitudes between 16.000 and 20.000 km while some low frequency AH with frequencies between 7 and 9 kHz

were generated at altitudes less than 8000 km. Another result obtained is that some auroral field lines between $77° \leq \Lambda \leq 81°$ have enhanced electron density that can be modeled from the reference density $N_{e.ref} \sim 100$ el cm^{-3} at 2 R_E altitude.

Further analysis of the IAH spectra shows that hiss events with dispersion as low as 70 ms are also present in the spectra. For example, hiss event number 3 shows a dispersion of 70 ms for frequencies 9 and 17 kHz. From Figures 4.2.3.6 through 4.2.3.13, it can be inferred that these 2 frequencies should have generated at approximately the same altitude. Dispersion for hiss events 1, 2, 3, 4, and 17 are given in Table 10.

Table 10: Dispersion for hiss events 1, 2, 3, 4, and 17

Hiss Event	Frequencies (kHz)	Dispersion (ms)
1	14 - 9	200
2	15 - 9	190
3	17 - 7	214
4	14 - 9	357
17	19 - 9	357

The observed dispersion cannot be obtained if the density model is defined by $N_{e.ref} = 0.1$ el cm^{-3} at 2 R_E altitude. So hiss for these events has propagated along field lines whose electron concentration can be defined either by $N_{e.ref} \sim$ 1, 10, 100 el cm^{-3} at 2 R_E altitude. Hiss events 1, 2, and 3 can be further analyzed if photometer data is available. For instance, if $E_{\|}$ is $\sim$ 10 keV then $N_{e.ref}$ is approximately 100 el cm^{-3} at 2 R_E altitude because the other density models cannot give the observed dispersion for these three hiss events. However, in this case additional information is needed to determine the source region of hiss. If $E_{\|} < 1$ keV, determining the cold plasma electron density along the field line is not possible with the dispersion data from the 3 hiss events (1,2 and 3) alone. Hiss events 1, 2, and 3 could have a source region of $\sim$ 8200 km altitude for low frequencies (7-9 kHz) and $\sim 5000 - 6000$ km altitude for high frequencies (14-17 kHz). The cold plasma electron density along the field lines in this case would be defined by $N_{e.ref} \sim 1$ el cm^{-3} at 2 R_E altitude. If the cold plasma electron

density along the field lines is defined by $N_{e,ref} \sim 10$ or 100 el cm^{-3} at 2 R_E altitude the source region of the AH cannot be determined with hiss events 1, 2, and 3 alone.

Hiss events 4 and 17 can be generated only by energetic electrons with $E_{\|} \leq 1$ keV to show dispersion of $\sim$ 360 ms. The cold plasma electron density along the field line that the hiss could have traveled can be defined by $N_{e,ref} \sim 10 - 100$ el cm^{-3} at 2 R_E altitude. If the AH was generated by energetic electrons with $E_{\|} \leq 0.5$ keV then the high frequency AH source altitude is $\sim 5,000 - 12,000$ km and the low frequency AH source altitude is $\sim 10,000 - 20,000$ km depending on f_{pe} and f_H of the density model.

A brief outline of the results obtained in this section are discussed in this paragraph prior to analyzing the last set of hiss events that show a dispersion of $\sim$ 500 ms and more. 17 hiss events require that they be generated by energetic electrons with $E_{\|} \sim 0.5$ keV along field lines whose electron density is defined by $N_{e,ref} \sim 100$ el cm^{-3} at 2 R_E altitude. For these 17 events, frequencies between 7 and 9 kHz should be generated between 16,000 and 20,000 km altitude while frequencies between 12 and 20 kHz should be generated at < 8000 km altitude. 2 hiss events (4 and 17) require that they be generated by energetic electrons with $E_{\|} \leq 1$ keV along field lines whose electron density is defined by $N_{e,ref} \sim 10$ or 100 el cm^{-3} at 2 R_E altitude. For these 2 hiss events 10 kHz waves should be generated between 10,000 and 20,000 km altitude while 14-20 kHz waves should be generated between 5000 and 10,000 km altitude. 3 hiss events (1, 2, and 3) require that the electron density along the field line on which they propagate be defined by $N_{e,ref} \sim 100$ el cm^{-3} at 2 R_E altitude if they are generated by 10 keV electrons. The source altitude for the AH in this case cannot be determined with the exiting data alone. If these 2 hiss events are generated by energetic electrons with $E_{\|} \leq 1$ keV the source altitude of AH cannot be determined and the cold plasma electron density along the field line can be defined as $N_{e,ref} \sim 1 - 100$ el cm^{-3} at 2 R_E altitude. In the next paragraph the last set of hiss events are analyzed.

Hiss events 5, 6, 7, 10, 11, 14, 18, 20, 25, 26, 32, 34, 35, and 36 show dispersion of $\sim$ 500 ms and more. This implies that the lower frequency must have a t_g greater than 500 ms. t_g is greater than 500 ms only if $N_{e,ref}$ =10 or

100 el cm^{-3} at 2 R_E and AH is generated by energetic electrons with $E_{\|} \leq 1$ keV (Figures 4.2.3.6 - 4.2.3.9). If hiss is generated by $\sim$ 1 keV electrons then the electron density along the field line can be defined by $N_{e,ref} \sim 100$ el cm^{-3} at 2 R_E altitude and the AH source altitudes would be $\sim 16.000 - 20.000$ km for 7-9 kHz waves and 5000-8000 km for 10-18 kHz waves. If the above hiss was generated by energetic electrons with $E_{\|} \sim 0.5$ keV then the electron density along the field line can be defined by $N_{e,ref} \sim 10 - 100$ el cm^{-3} at 2 R_E altitude. AH source region in this case would be $\sim 5000 - 9000$ km for 10-18 kHz waves and 12.000-20.000 km for 7-9 kHz waves.

To summarize based on the above analysis of AH spectra using the new propagation model developed in this thesis, it can be concluded that since 17 of the 36 hiss events require that 7-9 kHz waves be generated at altitudes between 16.000 and 20.000 km and 12-20 kHz waves be generated at < 8000 km altitude. AH hiss with frequencies 7-9 kHz and 12-20 kHz are generated between 16.000-20.000 km and 5000-8000 km altitude respectively. The events are generated by energetic electrons with $E_{\|} \sim 0.5$ keV and the hiss propagates along field lines between $77^{\circ} \leq \Lambda \leq 81^{\circ}$ with enhanced electron densities that can be defined as $N_{e,ref} \sim 100$ el cm^{-3} at 2 R_E altitude. These field lines have a R^{-5} density dependence outside the plasmasphere (chapter 3 and section 4.2). Some field lines between $77^{\circ} \leq \Lambda \leq 81^{\circ}$ can have electron concentration such that $N_{e,ref} \sim 10 - 100$ el cm^{-3} at 2 R_E altitude, since 14 events support this possibility. As for all analysis in this chapter these field lines will also have a R^{-5} density dependence outside the plasmasphere. AH in this case could have been generated by energetic electrons with $E_{\|} \leq 1$ keV. By considering these 14 events AH source region is such that 7-10 kHz waves could now have generated between $12.000 - 20.000$ km depending on local f_{pe} and f_H for this field line and 12-20 kHz waves could have generated between 5000-9000 km altitude.

The IAH spectra analysis also shows that the auroral region can support large density structures within 4° ($77^{\circ} - 81^{\circ}$) latitude range. These results are consistent with *Persoon et al.*, [1983] (Please refer to section 3.2 and Tables 5 and 6 for details). The results presented in this section was from analysis of an IAH spectra. If photometer data is available then the energy of the electrons from photometer data can be used to estimate the initial wave-normal angles at which

the different frequency waves were injected. Similarly if the ionospheric exit point is known from the direction finding system. the field line along which the hiss could have propagated can be determined. Information about the field line and initial wave-normal angle will improve the results obtained in this chapter.

5. Conclusions and Recommendations

In this chapter, a summary of the results discussed in the previous chapters is presented and recommendations are made for possible future work. In section 5.1 of this chapter, a summary of the new results presented in this thesis is provided. In section 5.2, the cold plasma electron density measurement technique proposed in chapters 2 and implemented in chapter 4 is compared with the use of whistlers that have been used in the past to determine the equatorial electron concentrations in the magnetosphere. Section 5.3 discusses new avenues for future research.

5.1 Summary of the Results Presented in This Thesis

In this thesis a new model to explain AH propagation from its source region to the ground is developed. Standard whistler mode propagation theory in the smooth magnetosphere suggests that AH generated with large wave-normal angle θ along auroral field lines cannot penetrate the ground. In this thesis, a new mechanism is suggested whereby large θ AH incident on meter-scale irregularities is converted to small θ AH that can reach the ground.

This thesis provides a method to (a) remotely sense cold plasma electron density along auroral field lines, (b) determine the AH source regions and (c) calculate the parallel resonance energy of the energetic electrons that generate AH. An example in section 4.3 illustrates how to remotely sense from the ground-AH-spectra the field line(s) along which AH propagates to the ground, the AH source region, and the cold plasma electron density along the auroral field line(s). Chapter 3 of this thesis also shows how to determine the density along the magnetosphere given one reference point and methods to adapt the ray-tracing program to study auroral regions.

Auroral hiss source regions have been determined, in the past, either from satellite data or from ground observations of hiss. Satellite data places the source altitude of auroral hiss at $\sim 5000 - 10,000$ km. Ground measurements on the

other hand indicate that the source altitude of AH is ≥ 20.000 km. This thesis reinterprets the satellite data to show that the source altitude of AH can be anywhere between 5000 and 20.000 km altitude depending on frequency.

The proposed model also explains the prior observed features of auroral hiss not understood before:

(1) The ionospheric exit points of auroral hiss with respect to visible aurora:
Chapter 2 shows that impulsive auroral hiss (IAH) chiefly propagates in a ducted mode while continuous auroral hiss (CAH) propagates in a nonducted mode. When a ducted wave (IAH) exits the duct and is scattered by meter-scale irregularities. Figure 2.5.2 shows that about 0.1% to 10% of the waves have small wave-normal angles and penetrate the ground. The remaining hiss that does not fall in the transmission cone is either reflected or continuously scattered such that it can finally exit a few hundred kilometers away from the location of the aurora. Thus the model proposed in this thesis shows how a large percentage of IAH can be seen beneath or within $\sim$ 100 km of an overhead aurora. Similarly. CAH propagating in the nonducted mode departs from the source field line and reaches the meter-scale irregularities wherein it is scattered into electrostatic (big θ) and electromagnetic (small θ) waves. The scattered hiss that penetrates to the ground is observed $\sim$ 600 km equatorward of the observed aurora. Continuous scattering of some percentage of CAH could also result in a small percent of CAH entering the transmission cone and being seen within $\sim$ 100 km of an overhead aurora.

(2) The dispersion of impulsive IAH:
Sections 2.2 and 4.2 show the frequency and altitude dependence of waves on energy ($E_{\parallel}$) for different density models. The proposed mechanism shows how IAH observed on the ground should be generated at higher altitudes for lower frequencies and lower altitudes for higher frequencies giving the observed discrete spectra on the ground.

(3) The characteristic spectra of IAH and CAH:
Chapters 2 and 4 show that the spectral dispersion and discreteness in IAH spectra is due to different frequencies being generated at different altitudes and propagating to the ground in a ducted mode while the smooth spectra for CAH is a result from random mixing of waves. arriving from a range of source altitudes

in a nonducted mode and scattering from meter-scale irregularities.

(4) Observed dispersion that ranges from a few tens of milliseconds to a second: Analysis of group time as a function of θ and frequency for different altitudes and density models (chapter 4) shows that when different frequencies are generated at the same altitude the dispersion obtained is in the range of a few tens of milliseconds to a few hundreds of milliseconds whereas when different frequencies are generated at different altitudes the dispersion obtained is in the range of a few hundreds of milliseconds to a second.

(5) Difference in auroral intensity between ground and satellite observations: The ground intensity of auroral hiss is 2 to 5 orders of magnitude smaller than that observed on the satellite. Analysis of scattering of waves from meter-scale irregularities shows that only 0.1% to 10% of the incident hiss with large wave-normal angles are converted to hiss with small wave-normal angles that can penetrate to the ground. IAH and CAH also suffer losses because of D region absorption phenomenon. The absorption values at $\Lambda = 70°$ and altitude = 60-1500 km for 2 and 20 kHz are $\sim$ 1.2 and $\sim$ 3 dB respectively for a nighttime ionosphere and $\sim$ 8 and $\sim$ 20 dB respectively for a daytime ionosphere [*Helliwell*, 1965]. CAH also suffers transmission losses at the Earth-ionosphere boundary depending on its exit point. *Tsuruda et al.*, [1982] measured a -7 dB per 100 km rate of attenuation with distance and Walker [1974] estimated a -12 dB per 1000 km loss. IAH does not incur transmission losses in the Earth-ionosphere waveguide. The above losses explain the difference in the observed power spectral density between satellite and ground readings of AH.

(6) Explains the lower frequency cutoff of IAH and CAH:
f_{LHR} at the highest altitude up to which meter-scale irregularities exist determines the lower frequency cutoff for both IAH and CAH. Frequencies that have a f_{LHR} above this altitude will be reflected into the magnetosphere before reaching the meter-scale irregularities. Meter-scale irregularities extend up to a few thousand kilometers [*Fejer and Kelley*, 1980; *Sonwalkar*, 1995] and this implies a low cutoff frequency of AH at a few kiloHertz, consistent with observations.

5.2 Comparison of the Proposed Cold Plasma Electron Density Measurement Technique With Whistlers That are Used to Determine the Cold Plasma Equatorial Electron Concentrations in the Magnetosphere.

In this section, a study is made to compare the technique proposed in this thesis to remotely sense the auroral magnetosphere with the whistler wave technique to determine equatorial electron concentrations in the magnetosphere. Whistlers have been very successful in the past to study equatorial electron densities and these studies have led to the discovery of the magnetosphere and plasmapause. However, there is no method to study the auroral magnetosphere and in this thesis a new mechanism is proposed to study the auroral region of the magnetosphere. A basic difference between the use of the technique proposed in this thesis to the use of whistlers to determine cold plasma electron densities is that whistlers are used to determine equatorial cold plasma electron densities for a known L shell while the technique proposed in this thesis is used to determine the cold plasma electron density along unknown auroral field lines. In the use of whistlers to determine the cold plasma electron density, the L shell is first determined from the nose frequency (f_n) and time delay (t_n) at f_n. Once the L shell is determined, the cold plasma electron density is determined by an iterative search of diffusive equilibrium density models and collisionless R^{-n} density models. The iterative search involves determining the right density and gyrofrequency that will mathematically reproduce the observed t_n for the observed f_n. Disadvantage with the use of whistlers is that their source region is approximately between L=2 ($\Lambda = 45°$) and L=4 ($\Lambda = 60°$). As a result nose whistlers are not seen at very high latitudes ($\Lambda = 65°$) or at very low latitudes (very close to the equator). Additionally, in the mathematical computation of t_n, it is assumed that $f/f_H \ll 1$ and $f_{pe} \gg f_H$. These conditions do not hold true at high altitudes.

The technique proposed in this thesis helps to determine electron densities along auroral field lines. A brief synopsis of how AH spectrograms recorded on the ground can be used to invert the data to determine electron concentrations along auroral field lines is provided in section 4.1. In the proposed model, the invariant latitude is approximated from the dispersion data and the location of

the recording station . With this technique one field line cannot be accurately determined as the field line along which the hiss could have propagated. It is also possible that the electron concentrations are very different between these field lines as suggested in theory [*Persoon et al.*, 1983] and shown in this thesis (section 4.3). More accurate results can be obtained with the proposed model if additional data from a photometer or direction finding system is available. The advantage with the model is that, to date all density measurements at high latitudes and altitudes have only been made on spacecraft. The technique discussed in this thesis provides a possible method to make ground measurements over time periods of seconds to hours.

5.3 Recommendations for Future Work

A new approach is proposed, in this thesis, to invert ground readings of AH to determine the cold plasma electron density along auroral field lines. Unlike the technique proposed with nose whistlers, the field line is unknown in this case. The model proposed in this thesis determines the cold plasma electron concentrations along a range of possible field lines and this range can be narrowed if additional data is available. Possible future work could involve developing a direction finding system, to measure AH exit point, such as one developed by *Tsuruda and Hayashi*, [1975].

In chapter 2 of this thesis the upper and lower frequency cutoff of IAH and CAH as a function of Landau damping is discussed. The proposed model suggests that the upper frequency cutoff for CAH is probably determined by Landau damping. Both IAH and CAH propagate downward with large θ and for high frequencies Landau damping is significant especially at low energies. An in-depth analysis on the role of Landau damping on auroral hiss could lead to significant results.

Meter-scale irregularities play an important role in the proposed mechanism of hiss propagation from high source altitudes to the ground. Hiss penetrates to the ground by scattering from meter-scale irregularities. As discussed in section 2.5, approximately 0.1% to 10% of the incident hiss reaches the ground. This

could be a possible reason for the lack of correlation between hiss intensity and visible aurora luminosity. Radar observations show a strong correlation between the occurrence of VLF hiss in the 1-10 kHz range and 18 MHz radar echoes from the F-region field-aligned irregularities [*Hower and Gluth*, 1965]. All but one of the 33 hiss events observed by *Hower and Gluth*, [1965] were associated with the 18 MHz radar echoes. However, more work needs to be done to study the relation between the amplitude and range of meter-scale irregularities and the observed auroral hiss intensity.

AH scattering by meter-scale irregularities suggests that some AH can be converted to LH waves [*Bell et al.*, 1991]. High-amplitude LH waves are excited when

$$f_{LHR} \leq f \ll f_H \tag{5.3.1}$$

$$\lambda N^{-1}\, dN/ds \geq 1 \tag{5.3.2}$$

where f and λ are the frequency and wavelength of the whistler mode wave. N is the thermal plasma density, and s is the distance measured in the direction perpendicular to both $\overline{B}_o$ and planar irregularities [*Bell et al.*, 1991]. For $s \sim \lambda$ and density enhancements of $\sim$ 100% the above condition is satisfied for low-frequency AH ($\sim 3 - 15$ kHz) and hence a fraction of the whistler mode waves in the proposed model is converted to high-amplitude LH waves. Similar results are obtained when $s < \lambda$ and density enhancements are small. LH waves are important because they couple both to electrons and ions.

A possible topic for future research would be to obtain the LH wave intensity and its region of occurrence using the proposed propagation mechanism discussed in this thesis. A brief outline of the process can be as follows: From the measured exit point of AH and radar data one can obtain the location of the meter-scale irregularity responsible for stimulation of LH waves. Radar data can also provide an estimate of the wavelength and density enhancement of the meter-scale irregularities. The value of f_{LHR} in association with a density model similar to the one shown in Figures 2.2, 4.2.1-5 can then be used to find the upper altitude limit of the meter-scale irregularities. Using the measured density (ionosonde

data). a density model can be constructed and used in scattering calculations (Figure 2.5.2). From the measured AH intensity and the results of scattering calculations. LH intensity can be estimated.

References

Angerami. J.J.. Thomas. J.O.. Studies of planetary atmosphere 1. the distribution of electrons and ions in the Earth's exosphere. *J. Geophys. Res.. 69.* 4537. 1964.

Barrington. R.E.. T.R. Hartz. and R.W. Harvey. Diurnal distribution of ELF. VLF and LF noise at high latitudes as observed by Alouette-2. *J. Geophys. Res.. 76.* 5278. 1971.

Beghin. C.. J.L. Rauch. and J.M. Bosqued. Electrostatic plasma waves and HF auroral hiss generated at low altitude. *J. Geophys. Res.. 94.* 1359. 1989.

Bell. T. F.. and H. D. Ngo. Electrostatic waves stimulated by coherent VLF signals propagating in and near the inner radiation belt. *J. Geophys. Res.. 93.* 2599. 1988.

Bell. T. F.. and H. D. Ngo. Electrostatic lower hybrid waves excited by electromagnetic whistler mode waves scattering from planar magnetic-field-aligned plasma density irregularities. *J. Geophys. Res.. 95.* 149. 1990.

Bell. T.F.. U.S. Inan. V.S. Sonwalkar. and R.A. Helliwell. DE-1 observations of lower hybrid waves excited by VLF whistler mode waves. *Geophys. Res. Lett.. 18.* 393. 1991.

Benson. R. F.. and W. Calvert. ISIS 1 observations at the source of auroral kilometric radiation. *Geophys. Res. Lett.. 6.* 479. 1979.

Benson. Robert F.. Joseph M. Grebowsky. Extremely low ionospheric peak altitudes in the polar hole region. *Radio Sci.. 36.* 277. 2001.

Bernhardt. P. A.. and C. G. Park. Protonospheric-ionospheric modeling of VLF ducts. *J. Geophys. Res.. 82.* 5222. 1977.

Burtis. W.J.. *Users' Guide to the Stanford VLF Ray Tracing Program.* RadioSci. Lab.. Stanford Electr. Lab.. Stanford Univ.. Stanford. Calif.. 1974.

Calvert. W.. The auroral plasma cavity. *Geophys. Res. Lett.. 8.* 919. 1981.

Chang. T.. and B. Coppi. Lower hybrid acceleration and ion evaluation in the supra-auroral region. *Geophys. Res. Lett.. 8.* 1253. 1981.

Carpenter. D.L.. Earth's plasmasphere awaits rediscovery. *EOS. 76.* 89-92. 1995.

Carpenter. D. L.. and C. G. Park. On what ionospheric workers should know about the plasmapause-plasmasphere. *Rev. Geophys. Space Phys.. 11.* 133. 1973.

Chen. X. Observations and Analysis of Whistler Mode Echoes Received by RPI on IMAGE at High Latitudes. Masters thesis. University Of Alaska Fairbanks. Fairbanks. Alaska.. 2000.

Davies. K.. *Ionospheric Radio Waves.* Blaisdell Publishing Company. A Division of Ginn and Company. Waltham. Massachusetts. 1969.

Draganov. A. B.. U. S. Inan. V. S. Sonwalkar. and T. F. Bell. Whistlers and plasmaspheric hiss: Wave directions and three-dimensional propagation. *J. Geophys. Res.. 98.* 11.401. 1993.

Ergun. R.E.. E. Klementis. C.W. Carlson. J.P. McFadden. and J.H. Clemmons. Wavelength measurement of auroral hiss. *J. Geophys. Res.. 96.* 21.299 1991.

Farrell. W.M.. D.A. Gurnett. P.M. Banks. and R.I. Bush. An analysis of whistler mode radiation from the Spacelab 2 electron beam. *J. Geophys. Res.. 93.* 153. 1988.

Farrell. W.M.. D.A. Gurnett. and C.K. Goertz. Coherent Cerenkov radiation from the Spacelab 2 electron beam. *J. Geophys. Res.. 94.* 443. 1989.

Fejer. B.G.. and M.C. Kelley. Ionospheric irregularities. *Rev. Geophys.. 18.* 401. 1980.

Groves. K.M.. M.C. Lee. and S.P. Kuo. Spectral broadening of VLF radio signals traversing the ionosphere. *J. Geophys. Res.. 93.* 14.683. 1988.

Gurnett. D. A.. Electromagnetic plasma wave emissions from the auroral field lines. *J. Geomagn. Geoelectr.. 30.* 257. 1978.

Gurnett. D. A.. and L.A. Frank. ELF noise bands associated with auroral electron precipitation. *J. Geophys. Res.. 77.* 3411. 1972.

Gurnett. D.A.. and J.L. Green. On the polarization and origin of auroral kilometric radiation. *J. Geophys. Res.. 83.* 689. 1978.

Gurnett. D. A.. S. D. Shawhan. and R. R. Shaw. Auroral hiss. *Z* mode radiation. and auroral kilometric radiation in the polar magnetosphere: DE 1 observations. *J. Geophys. Res.. 88.* 329. 1983.

Hargreaves. J.K.. tempit The solar-terrestrial environment. Cambridge Univ. Press. Cambridge. Great Britain. 1995.

Harikumar. J.. and V.S. Sonwalkar. Trapping and propagation of large wave normal angle whistler mode waves through field aligned density depletions or enhancements (Ducts) in the auroral magnetosphere: applications to impulsive auroral hiss. presented at XXVI URSI General Assembly. 13-21 Aug. 1999. Toronto Canada.

Haselgrove. J.. Ray theory and a new method for ray tracing. in *Report. of Physical Society Conference on Physics of the Ionosphere*. p. 355. Cambridge Univ. Press. New York. 1954.

Helliwell. R. A.. *Whistlers and Related Ionospheric Phenomena*. Stanford Univ. Press. Stanford. Calif.. 1965.

Helliwell. R. A.. and M.G. Morgan. Summary of research on whistlers and related phenomena. *J. Res. Natl. Bur. Stand. U.S.. Sect. D. 64*. 642. 1960.

Hoffman. R. A.. and T. Laaspere. Comparison of very-low-frequency auroral hiss with precipitating low-energy electrons by the use of simultaneous data from two OGO 4 experiments. *J. Geophys. Res.. 77*. 640. 1972.

Hower. G. L.. and W. I. Gluth. Association between VLF hiss and HF radar echoes from field-aligned ionization. *J. Geophys. Res.. 70*. 649. 1965.

Inan. U. S.. and T. F. Bell. The plasmapause as a VLF wave guide. *J. Geophys. Res.. 82*. 2819. 1977.

James. H. G.. Refraction of whistler-mode waves by large-scale gradients in the middle latitude ionosphere. *Ann. Geophys.. 28*. 301. 1972.

James. H. G.. Whistler-mode hiss at low and medium frequencies in the dayside-cusp ionosphere. *J. Geophys. Res.. 78*. 4578. 1973.

Jorgensen. T. S.. Interpretation of auroral hiss measured on OGO 2 and at Byrd Station in terms of incoherent Cerenkov radiation. *J. Geophys. Res.. 73*. 1055. 1968.

Jorgensen. T. S.. VLF and LF emissions at auroral latitudes. in Low Frequency Waves and Irregularities in the Ionosphere. edited by N.D'Angelo. pp. 111-119. D. Reidel. Norwell. Mass.. 1969.

Jorgensen. T. S.. Progress in ELF/VLF emission studies at high latitudes. in The Radiating Atmosphere. edited by B.M. McCormac. pp. 327-335. D. Reidel. Norwell. Mass.. 1979.

Kimura. I.. Effects of ions on whistler-mode raytracing. *Radio Sci.. 1.* 269. 1966.

Kletzing. C.A.. F.S. Mozer and R.B. Torbert. Electron temperature and density at high latitude. *J. Geophys. Res.. 103.* 14.837. 1998.

Laaspere. T.. and W. C. Johnson. Additional results from an OGO 6 experiment concerning ionospheric electric and electromagnetic fields in the range 20 Hz to 540 kHz. *J. Geophys. Res.. 78.* 2926. 1973.

LaBelle. J.. A.T. Weatherwax. J. Perring. E. Walsh. M.L. Trimpi. and U.S. Inan. Low-frequency impulsive auroral hiss observations at high geomagnetic latitudes. *J. Geophys. Res.. 103.* 20.459. 1998.

Lysak. R. L.. M. K. Hudson. and M. Temerin. Ion heating by strong electrostatic ion cyclotron turbulence. *J. Geophys. Res.. 85.* 678. 1980.

Maeda. K.. A calculation of auroral hiss with improved models for geoplasma and magnetic field. *Planet. Space Sci.. 23.* 843. 1975.

Maggs. J. E.. Coherent generation of VLF hiss. *J. Geophys. Res.. 81.* 1707. 1976.

Maggs. J. E.. Electrostatic noise generated by the auroral electron beam. *J. Geophys. Res.. 83.* 3173. 1978.

Maggs. J. E.. and W. Lotko. Altitude dependent model of the auroral beam and beam-generated electrostatic noise. *J. Geophys. Res.. 86.* 3439. 1981.

Makita. K.. VLF-LF hiss emissions associated with aurora. Mem. Natl. Inst. Polar Res. Jpn.. *Ser. A. 16.* 1. 1979.

Martin. L.H.. R.A. Helliwell. and K.R. Marks. Association between aurorae and very low-frequency hiss observed at Byrd station. Antarctica. *Nature. 187.* 751. 1960.

Matsuo. T.. T. Nishiyama. and D. Matubara. Propagation of a quasi electrostatic whistler mode auroral hiss to the ground. *Proc. NIPR Symp. Upper Atmos. Phys.. 12.* 12. 1998.

McIlwain. C.E.. Coordinates for mapping the distribution of magnetically trapped particles. *J. Geophys. Res.. 66.* 3681. 1961.

Morgan. D. D.. D. A. Gurnett. J. D. Menietti. J. D. Winningham. and J. L. Burch. Landau damping of auroral hiss. *J. Geophys. Res.. 99.* 2471. 1994.

Mosier. S. R.. and D. A. Gurnett. VLF measurements of the Poynting flux along the geomagnetic field with the Injun 5 satellite.. *J. Geophys. Res.. 74.* 5675. 1969.

Mosier. S. R.. and D. A. Gurnett. Observed correlation between auroral and VLF emissions. *J. Geophys. Res.. 77.* 1137. 1972.

Mozer. F. S.. C. A. Cattel. M. K. Hudson. R. A. Lysak. M. Temerin. and R. B. Torbert. Satellite measurements and theories of low altitude auroral particle acceleration. *Space Sci. Rev.. 27.* 155. 1980.

Ngo. H. D.. Electrostatic waves stimulated by VLF whistler mode waves scattering from magnetic field aligned plasma density irregularities. Ph.D. thesis. Stanford Univ.. Stanford. Calif.. 1989.

Ondoh. T.. Polar hiss observed by ISIS satellites. in *Magnetospheric Substorms.* edited by J.R. Kan et al.. *Geophys. Monogr. Ser.*. vol. 64. p. 387. AGU. Washington. D.C.. 1991.

Ondoh. T.. Y. Nakamura. and T. Murakami. Characteristics of VLF saucers and auroral hiss from ISIS satellite received at Syowa station. Antarctica. *Mem. Natl. Inst. Polar Res.. Jpn.. Spec. Issue. 18.* 54. 1981.

Park. C.G. and D.L. Carpenter. Very Low Frequency Radio Waves in the magnetosphere. *Upper Atmospheric Research in Antarctica. Antarctic Research Series. Vol 29.* Paper 4. 1978.

Persoon. A.M.. Electron density distributions in the high-latitude magnetosphere. *Adv. Space Res.. 8.* (8) 79-88. 1988.

Persoon. A.M.. D.A. Gurnett. and S.D. Shawhan. Polar cap electron densities from DE 1 plasma wave observations. *J. Geophys. Res.. 88.* 10.123. 1983.

Persoon. A.M.. D.A. Gurnett. W.K. Peterson. J.H. Waite Jr.. J.L. Burch. and J.L. Green. Electron density depletions in the nightside auroral zone. *J. Geophys. Res.. 93.* 1871. 1988.

Sahr. J.D.. and B.G. Fejer. Auroral electrojet plasma irregularity theory and experiment: A critical review of present understanding and future directions. *J. Geophys. Res.. 101.* 26.893. 1996.

Sazhin. S.. S. K. Bullough. and M. Hayakawa. Auroral hiss: A review. *Planet. Space Sci.. 41.* 153. 1993.

Singh. D. P.. and B. Singh. Propagation characteristics of ground observed VLF waves after emerging from the ducts in the ionosphere. *Ann. Geophys.. 34.* 113. 1978.

Siren. J.C.. Dispersive auroral hiss. *Nature Phys. Sci.. 238.* 118. 1972.

Siren. J. C.. Fast hisslers in substorms. *J. Geophys. Res.. 80.* 93. 1975.

Sonwalkar. V.S.. Magnetospheric LF-. VLF-. and ELF-waves. in *Handbook of Atmospheric Electrodynamics.* pp. 407-462. CRC Press. Boca Raton. Fla.. 1995.

Sonwalkar. V.S.. and Harikumar. J.. Generation and propagation of auroral hiss. *Eos Trans.. 78. 46.* F618. 1997 (abstract).

Sonwalkar. V.S.. and Harikumar. J.. An explanation of ground observations of auroral hiss: role of density depletions and meter-scale irregularities. *Eos Trans.. 79. 45.* F764. 1998 (abstract).

Sonwalkar. V.S.. and Harikumar. J.. Scattering of large wave normal angle whistler mode waves by field-aligned density irregularities in the auroral ionosphere: applications to continuous auroral hiss. presented at XXVI URSI General Assembly. 13-21 Aug. 1999. Toronto Canada.

Sonwalkar. V.S.. and Harikumar. J.. On what we can learn about auroral region from the ground observations of auroral hiss. *Eos Trans.. 80. 46.* S868. 1999 (abstract).

Sonwalkar. V.S.. and Harikumar. J.. An Explanation of Ground Observations of Auroral Hiss: Role of Density Depletions and Meter-Scale Irregularities. *J. Geophys. Res.. 105.* 18867. 2000.

Sonwalkar. V. S.. T. F. Bell. R. A. Helliwell. and U. S. Inan. Direct multiple path propagation: A fundamental property of nonducted VLF waves in the magnetosphere. *J. Geophys. Res.. 89.* 2823. 1984.

Sonwalkar. V.S.. J. Harikumar. D. L. Carpenter. and T. F. Bell. Analysis of whistler mode wave injection experiments with RPI on IMAGE spacecraft. presented at XXVI URSI General Assembly. 13-21 Aug. 1999. Toronto Canada.

Sonwalkar. V.S.. X. Chen. J. Harikumar. D. L. Carpenter. and T. F. Bell. Whistler-mode wave-injection experiments in the plasmasphere with a radio sounder. *J. Atmos. Solar Terr. Phys.. 63.* 1199. 2001.

Sonwalkar. V.S.. U.S. Inan. T.F. Bell. R.A. Helliwell. O.A. Molchanov. and J.L. Green. DE 1 VLF observations during Activny wave injection experiments. *J. Geophys. Res.. 99.* 6173. 1994.

Sonwalkar. V.S.. X. Chen. J. Harikumar. D.L. Carpenter. T.F. Bell. M. Salvati. and J. Bortnik. Whistler mode wave injection experiments with RPI on IMAGE spacecraft. *Eos Trans.. 80. 46.* FS39. 1999 (abstract).

Sonwalkar. V.S.. X. Chen. J. Harikumar. D.L. Carpenter. M. Salvati. T.F. Bell. W.W. Taylor. S.F. Fung. J.L. Green. B.W. Reinisch. J. Goldstein. P. Reiff. Initial observations and analysis of whistler mode echoes received by RPI on IMAGE. *Eos Trans.. 81. 48.* F1038. 2000 (abstract).

Srivastava. R.N.. Propagation of VLF emissions in the magnetosphere and the ionosphere. *Planet. Space Sci.. 22.* 1545. 1974.

Srivastava. R.N.. VLF hiss. visual aurora and geomagnetic activity. *Planet. Space Sci.. 25.* 375. 1976.

Swift. D.W.. and J.R. Kan. A theory of auroral hiss and implications on the origin of auroral electrons. *J. Geophys. Res.. 80.* 985. 1975.

Stix. T.H.. *Waves in Plasmas.* American Institute of Physics. New York. 1992.

Tanaka. Y.. M. Hayakawa. and M. Nishino. Study of auroral VLF hiss observed at Syowa Station. Antarctica. *Mem. Natl Inst. Polar Res. Jpn.. Ser. A. 13.* 58 p.. 1976.

Titova. E.E.. V.I. Di. V.E. Yurov. O.M. Raspopov. V. Y. Trakhtengertz. F. Jiricek. and P. Triska. Interaction between VLF waves and turbulent ionosphere. *Geophys. Res. Lett.. 11.* 323. 1984.

Tsuruda. K. and K. Hayashi. Direction finding technique for elliptically polarized

VLF electromagnetic waves and its application to the low latitude whistlers. *J. Atmos. Terr. Phys.*, *37*, 1193, 1975.

Tsuruda, K., S. Machida, T. Teresawa, A. Nishida, and K. Maezawa, High spatial attenuation of the Siple transmitter signal and natural VLF chorus observed at ground-based chain stations near Roberval, Quebec, *J. Geophys. Res.*, *87*, 742, 1982.

Walker, A.D.M., Excitation of the Earth-ionosphere waveguide by downgoing whistlers. II. Propagation in the magnetic meridian, *Proc. R. Soc. London, Ser. A*, 340, 375, 1974.

Winningham, J. D. and W. J. Heikkila, Polar cap auroral electron fluxes observed with ISIS 1, *J. Geophys Res.*, *79*, 9495, 1974.

Yabroff, I., Computation of whistler ray paths, *J. Res., Natl. Bur. Stand. U.S., Sect. D*, *65D*, 485, 1961.

Yamamoto, T., On the amplification of VLF hiss, *Planet. Space Sci.*, *27*, 273, 1979.